Precision Measurement in Quantum Optics

by

David J. Starling

Submitted in Partial Fulfillment

of the

Requirements for the Degree

Doctor of Philosophy

Supervised by

Professor John C. Howell

Department of Physics and Astronomy
Arts, Sciences and Engineering
School of Arts and Sciences

University of Rochester
Rochester, New York

2012

For my wife Sarah and my parents Linda and Richard

Curriculum Vitae

David Starling was born in Jacksonville Beach, Florida on September 20, 1983. He attended the State University of New York at Fredonia where he received his Bachelor of Science in Physics and Mathematics in the spring of 2006. He began graduate work at the University of Rochester in the fall of 2006 and received his Master of Arts in Physics in the Fall of 2008. He pursued his doctoral research in experimental atomic physics and quantum optics under the supervision of Professor John C. Howell beginning in the summer of 2007.

Publications

1. **Null Weak Values and Quantum State Discrimination**, Oded Zilberberg, Alessandro Romito, Gregory A. Howland, David J. Starling, John C. Howell, and Yuval Gefen, *In Submission*.

2. **Highly dispersive off-resonant atomic prism using rubidium vapor**, David J. Starling, Steven M. Bloch, Praveen K. Vudyasetu, Joseph S. Choi and John C. Howell, *In Submission*.

3. **Extracting an entanglement signature from only classical mutual information**, David J. Starling, Curtis J. Broadbent and John C. Howell, Phys. Rev. A **84**, 032305 (2011).

4. **Precision frequency measurements with interferometric weak values**, David J. Starling, P. Ben Dixon, Andrew N. Jordan and John C. Howell, Phys. Rev. A **82**, 063822 (2010).

5. **Heralded single-photon partial coherence**, P. Ben Dixon, Gregory Howland, Mehul Malik, David J. Starling, R. W. Boyd, and John C. Howell, Phys. Rev. A **82**, 023801(R) (2010).

6. **Continuous phase amplification with a Sagnac interferometer**, David J. Starling, P. Ben Dixon, Nathan S. Williams, Andrew N. Jordan, and John C. Howell, Phys. Rev. A **82**, 011802(R) (2010).

7. **Interferometric weak value deflections: Quantum and classical treatments**, John C. Howell, David J. Starling, P. Ben Dixon, Praveen K. Vudyasetu, and Andrew N. Jordan, Phys. Rev. A **81**, 033813 (2010).

8. **Optimizing the signal-to-noise ratio of a beam-deflection measurement with interferometric weak values**, David J. Starling, P. Ben Dixon, Andrew N. Jordan, and John C. Howell, Phys. Rev. A **80**, 041803(R) (2009).

9. **Ultrasensitive Beam Deflection Measurement via Interferometric Weak Value Amplification**, P. Ben Dixon, David J. Starling, Andrew N. Jordan, and John C. Howell, Phys. Rev. Lett. **102**, 173601 (2009).

10. **All Optical Waveguiding in a Coherent Atomic Rubidium Vapor**, Praveen K. Vudyasetu, David J. Starling, and John C. Howell, Phys. Rev. Lett. **102**, 123602 (2009).

11. **Quantum chaos, delocalization, and entanglement in disordered Heisenberg models**, Winton G. Brown, Lea F. Santos, David J. Starling, and Lorenza Viola, Phys. Rev. E **77**, 021106 (2008).

Conference Proceedings

1. Poster: **Extracting an entanglement signature from only classical mutual information**, David J. Starling, Curtis J. Broadbent and John C. Howell, *Cross Border Workshop*, University of Rochester (June 2011).

2. **Extracting an entanglement signature from only classical mutual information**, David J. Starling, Curtis J. Broadbent and John C. Howell, *Conference on Lasers and Electro-Optics (CLEO)*, Baltimore, MD (May 2011).

3. **Near Quantum Limited Optical Phase Measurements on a Dark Fringe**, David J. Starling, P. Ben Dixon, Nathan S. Williams, Andrew N. Jordan and John C. Howell, *Frontiers in Optics*, Rochester, NY (October 2010).

4. Poster: **Weak Value Deflection Measurement**, David J. Starling, P. Ben Dixon and John C. Howell, *Sym. on Optical Int. and Quantum Systems*, University of Rochester (October 2009).

5. **Connecting the 3-d O(4) Heisenberg Spin Model to the 4-d SU(2) Lattice Gauge Theory**, David J. Starling and Michael Grady, *Rochester Symposium for Undergraduate Physics Students*, University of Rochester (April 2006).

6. **Test of Ladder-Track Design for Inductrack Magnetic Levitation**, <u>David J. Starling</u> *et al.*, *Rochester Symposium for Undergraduate Physics Students*, University of Rochester (April 2004).

Acknowledgments

It is my honor to thank those people who have made this journey enjoyable, and without whom I would surely have struggled.

First and foremost, my graduate adviser John C. Howell has been a constant source of enthusiasm, support and friendship. His endless supply of kindness and faith has been an inspiration, and it has been an honor and privilege to work under his direction. I also wish to thank my undergraduate adviser, Michael Grady, whose quiet and profound manner astonishes, and without whom I might never have known the joys of research.

I would like to thank my colleagues P. Ben Dixon, with whom I have worked for over four years, and Nathan Williams, with whom I spent many hours discussing the various natures of our discipline. They have both been great sources of knowledge, amusement, and companionship. I also thank my tutors, Praveen Vudyasetu, Ryan Camacho and Curtis Broadbent for their patience in the lab. And finally, I would like to thank my co-authors and friends, Greg Armstrong, Greg Howland, Justin Dressel, Steve Bloch, Bethany Little, Gerardo Viza, James Schneeloch, Joeseph Choi and Julian Martinez.

Lastly, I would like to thank my family: my parents, for supporting and encouraging me throughout my childhood; my grandparents, for their incredible patience and generosity; and of course my loving wife, for her unending support. Sarah, without you in my life, the world would seem a very different place.

Abstract

The work contained in this thesis is derived from various projects completed during my studies at the University of Rochester. The first chapter introduces the reader to foundational concepts in quantum mechanics, quantum optics, weak values, and the interaction of light with matter. Chapter two covers the results of experiments conducted to measure the deflection of a beam of classical light using the weak value formalism. A discussion of the optimal signal to noise ratio of such a measurement is included. Chapter three shows how the so-called "inverse weak value" can be used to measure the phase of an optical beam with high precision. The following chapter includes results on precision frequency measurements using a standard glass prism and weak values, followed by related experimental results arising from the interaction of light with gaseous rubidium. Chapter five focuses on a proposal to use weak measurements to undo a random disturbance in the amplitude or phase of an entangled pair of photons. It is shown that the entanglement of an ensemble of photon pairs can be largely restored after this random disturbance.

Table of Contents

List of Figures

List of Acronyms

AAV   Aharonov, Albert, and Vaidman

BS   Beam Splitter

CCD   Charge Coupled Device

EIA   Electromagnetically Induced Absorption

EIT   Electromagnetically Induced Transparency

FWM   Four-wave mixing

HeNe   Helium-Neon Laser

HWP   Half-Wave Plate

LG   Laguerre Gaussian

POVM   Positive Operator Valued Measure

PBS   Polarizing Beam Splitter

QCD   Quad Cell Detector

Rb   Rubidium

SBC   Soleil-Babinet Compensator

SNR   Signal to Noise Ratio

SPDC   Spontaneous parametric down conversion

WV   Weak Values

WVA   Weak Value Amplification

Foreword

I, David Starling, made significant contributions in the experimental design, data collection, data analysis and reporting of the following. The following pages were authored by me except where noted below.

In chapter one, Fig. 1.2 was produced by P. Ben Dixon. Parts of sections 1.2.3 and 1.2.4 were co-authored by me, John C. Howell, P. Ben Dixon, Praveen K. Vudyasetu, and Andrew N. Jordan.

Chapter two is a collection of three publications in Physical Review Letters and Physical Review A, co-authored by me, P. Ben Dixon, Andrew N. Jordan, John C. Howell and Praveen K. Vudyasetu. The text has been edited from the published forms. Figures 2.1, 2.3 and 2.4 were produced in conjunction with P. Ben Dixon.

Chapter three is taken from a publication in Physical Review A, co-authored by me, P. Ben Dixon, Nathan S. Williams, Andrew N. Jordan and John C. Howell. The text has been edited from its published form. Figure 3.2 was produced by Andrew N. Jordan.

Chapter four is taken from: a publication in Physical Review A, co-authored by me, P. Ben Dixon, Andrew N. Jordan and John C. Howell; a publication in Physical Review Letters, co-authored by me, Praveen K. Vudyasetu and John C. Howell; and, a paper in submission, co-authored by me, Praveen K. Vudyasetu, Steven M. Bloch, Joseph S. Choi, Bethany Little and John C. Howell. Figures 4.4 through 4.15 were produced in conjunction with Praveen K. Vudyasetu.

Chapter five is a work in progress and was co-authored by me and Nathan Williams.

1   Introduction

1.1   Quantum Optics

Our understanding of light has undergone drastic changes throughout the years. Newton proposed that light was composed of particles in 1704 [1], whereas the very successful theories of Maxwell described light as waves by 1861 [2]. Yet now we believe both ideas are correct. Quantum optics is the result of this entangled history; it is the study of the quantum mechanical nature of the photon and is a marriage of physical optics with quantum field theory.

While Maxwell's equations could predict the propagation of light and its interactions with macroscopic materials with great accuracy, there were a number of troubling experimental results that could not be explained. One notable discrepancy is known as the "ultraviolet catastrophe," pointed out by Einstein and others, where classical theory in the early twentieth century predicted that a black body will radiate an infinite amount of energy in the low wavelength region of the spectrum. The solution was to assume that electromagnetic radiation could only exist in discrete packets or "quanta." By this point, Max Planck had already introduced his "action quantum," i.e. the photon, as a mathematical construct in late 1900, yet did not truly appreciate his contribution. It was not until 1905 that

Einstein gave weight to the action quantum when he published a description of the photoelectric effect [3], thus birthing the quantum mechanical description of electromagnetic radiation. In 1927, over twenty years later, Dirac tackled the difficult problem of describing the emission and absorption of photons while maintaining their wavelike nature [4], thus setting the stage for understanding electromagnetic radiation at a more fundamental level.

What follows is the result of more than one hundred years of work in quantum theory and the study of the photon, partially summarized in only a few short pages, and focusing on measurements, weak measurements, weak values, and the interaction of light with matter.

1.1.1 Quantum Mechanics and Quantum Measurement

Quantum mechanics is an attempt to understand the motion and interactions of particles at small length and/or high energy scales. It has been perhaps the most successful physical theory in human history, and it all begins with the quantum state $|\psi(t)\rangle$ and the Hamiltonian $\hat{H}$ which dictates its time evolution. This evolution is described by the Schrödinger equation and is written simply as

$$\hat{H}|\psi\rangle = i\hbar\frac{\partial}{\partial t}|\psi\rangle. \tag{1.1}$$

for a non-relativistic particle, where $\hbar$ is Planck's constant. In the pages that follow, we will consider the solutions to this equation in simple circumstances with various approximations. One interesting solution is for time-independent Hamiltonians and is given by

$$|\psi(t)\rangle = e^{-i\hat{H}t/\hbar}|\psi(0)\rangle. \tag{1.2}$$

We will use this solution in our discussion of weak values when appropriate.

Let's say we have a particle in the pure state $\rho = |\psi\rangle\langle\psi|$, and that we can decompose this state in the computational basis,

$$|\psi\rangle = \alpha|0\rangle + \beta|1\rangle, \tag{1.3}$$

where α and β are complex numbers and we assume that $|\psi\rangle$ is normalized, and therefore $|\alpha|^2 + |\beta|^2 = 1$. It is clear that our particle is a two state particle. The eigenstates $|0\rangle$ and $|1\rangle$ can represent any number of physical states, e.g., horizontal and vertical polarizations of light, spin up and spin down for spin-1/2 particles or the excitation of a two-level atom.

Let us next consider a measurement operator $\hat{\mathcal{O}}$ that corresponds to some laboratory device (say a CCD camera to measure position). We can decompose this measurement operator into its outcomes,

$$\hat{\mathcal{O}} = \sum_i o_i \hat{\mathcal{O}}_i, \tag{1.4}$$

where $\{\hat{\mathcal{O}}_i\}$ are the projectors onto the eigenstates of $\hat{\mathcal{O}}$ and $\{o_i\}$ are the corresponding eigenvalues. Using this operator, how might we calculate the average value of the corresponding observable for our state $|\psi\rangle$? There are two equivalent methods,

$$\langle\hat{\mathcal{O}}\rangle = \langle\psi|\hat{\mathcal{O}}|\psi\rangle \tag{1.5}$$

and

$$\langle\hat{\mathcal{O}}\rangle = \mathrm{Tr}(\hat{\mathcal{O}}\hat{\rho}). \tag{1.6}$$

For the state above, we might choose to write $\hat{\mathcal{O}}_i$ as the projectors onto the eigenstates $|0\rangle$ and $|1\rangle$, i.e.

$$\hat{\mathcal{O}}_0 = |0\rangle\langle0| = \hat{\Pi}_0, \tag{1.7}$$

$$\hat{\mathcal{O}}_1 = |1\rangle\langle1| = \hat{\Pi}_1. \tag{1.8}$$

We can think of these two projectors as the outcomes of a two-pixel camera, where $|0\rangle$ is the left pixel, and $|1\rangle$ is the right pixel. Performing a measurement

of $\hat{\mathcal{O}}_0$ ("does the photon strike the left pixel?") on our state $|\psi\rangle$ would therefore result in a new state, $|\psi'\rangle = \hat{\mathcal{O}}_0|\psi\rangle = \alpha|0\rangle$ with probability $|\alpha|^2$. This is called a projective measurement, because the photon has been projected into the one of its eigenstates ($|0\rangle$). By performing an ensemble of measurements, we can determine the magnitude of α and β from the probabilities. By rotating to new bases, we can also obtain the phases.

We can consider non-projective measurements by decomposing $\hat{\mathcal{O}}$ into a different set of states. For example, let's look at

$$\hat{\mathcal{O}} = o_+\hat{M}_+ + o_-\hat{M}_-, \tag{1.9}$$

where our new measurement operators are defined by

$$\hat{M}_+ = \sqrt{\frac{1+p}{2}}\hat{\Pi}_0 + \sqrt{\frac{1-p}{2}}\hat{\Pi}_1, \tag{1.10}$$

$$\hat{M}_- = \sqrt{\frac{1-p}{2}}\hat{\Pi}_0 + \sqrt{\frac{1+p}{2}}\hat{\Pi}_1 \tag{1.11}$$

for $0 \leq p \leq 1$. We see that for $p = 1$, we have the previous projective measurement case, whereas for $p = 0$, $\hat{M}_+ = \hat{M}_- \propto \hat{1}$. That is, an application of $\hat{M}_\pm$ for $p = 0$ does not change the state *and* we have no way to estimate the elements of ρ.

When $0 < p \ll 1$, however, we say that $\hat{M}_\pm$ represent *weak measurements*, i.e., measurements that only weakly probe the system. In the context of photon polarization, one might direct single photons toward a weakly polarization dependent beam splitter (BS) to simulate such a measurement.

Despite the weakness of this measurement, we can still compute the elements of ρ from measurements on an ensemble of identically prepared photons, assuming we know the value of p. For example,

$$|\alpha|^2 = \langle\hat{E}_+\rangle\frac{1+p^{-1}}{2} + \langle\hat{E}_-\rangle\frac{1-p^{-1}}{2}, \tag{1.12}$$

where $\hat{E}_\pm = \hat{M}_\pm^\dagger\hat{M}_\pm = \hat{M}_\pm\hat{M}_\pm$ are the elements of the positive operator valued measure (POVM), sometimes called the probability operators. After an ensemble

of measurements, we can accurately estimate the values of the $\langle \hat{E}_+ \rangle$ and $\langle \hat{E}_- \rangle$, which in turn give us the value for $|\alpha|$.

We now have the basic tools for describing a measurement in quantum mechanics. For a more detailed analysis, see reference 5. In the following section, we will discuss the quantum nature of the photon so that we can use this formalism to discuss weak values in the context of quantum optics.

1.1.2   The Photon

It is easy to envision a photon as a marble, flying around and interacting balistically with its environment. However, the true story is much more subtle. For one, photons have no mass, and they travel the same speed regardless of reference frame. Furthermore, there is also a great deal of difficulty in expressing the photon wave function, in part due to the fact that a photon has no definite position [6, 7]. We will, for the most part, ignore these subtleties, and instead focus on the standard treatment of quantizing the electromagnetic field.

We begin, as many treatments do (see e.g., reference 8), with a classical electromagnetic field confined to a one dimensional cavity of length L. For completeness, we write down Maxwell's equations in vacuum,

$$\nabla \times \mathbf{H} = \frac{\partial \mathbf{D}}{\partial t}, \tag{1.13}$$

$$\nabla \times \mathbf{E} = -\frac{\partial \mathbf{B}}{\partial t}, \tag{1.14}$$

$$\nabla \cdot \mathbf{B} = 0, \tag{1.15}$$

$$\nabla \cdot \mathbf{D} = 0, \tag{1.16}$$

with $\mathbf{B} = \mu_0 \mathbf{H}$, $\mathbf{D} = \epsilon_0 \mathbf{E}$, and ϵ_0 and μ_0 are the permitivity and permeability of free space, respectively. From this, and given the boundary conditions of the

cavity, we can determine the value of E_x and H_y to be

$$E_x(z,t) = \sum_i A_i q_i(t) \sin(k_i z), \qquad (1.17)$$

$$H_y(z,y) = \sum_i A_i \left(\frac{\dot{q}_i \epsilon_0}{k_i} \right) \cos(k_i z), \qquad (1.18)$$

where q_i is the amplitude of the ith normal mode, $k_i = i\pi/L$ is the wave number for the ith mode, and

$$A_i = \left(\frac{2\nu_i^2 m_i}{V \epsilon_0} \right)^{1/2}, \qquad (1.19)$$

where $\nu_i = i\pi c/L$ is the angular frequency of the ith mode, $V = LA$ is the volume of the cavity, and m_i is a constant with the dimension of mass.

To connect this classical description of the electromagnetic field to quantum mechanics, let us consider the following:

$$\mathcal{H} = \frac{1}{2} \int_V dV' (\epsilon_0 E_x^2 + \mu_0 H_y^2) \qquad (1.20)$$

$$= \frac{1}{2} \sum_i (m_i \nu_i^2 q_i^2 + m_i \dot{q}_i^2) \qquad (1.21)$$

$$= \frac{1}{2} \sum_i \left(m_i \nu_i^2 q_i^2 + \frac{p_i^2}{m_i} \right), \qquad (1.22)$$

where we started with the classical Hamiltonian, substituted in our solutions for E_x and H_y, and made the assignment $p_i = m_i \dot{q}_i$ in analogy with momentum. We immediately recognize the form of this Hamiltonian as a harmonic oscillator.

The final step is to assume that the canonical variables q and p become operators and therefore obey the quantum mechanical commutation relations for position and momentum, i.e. $[q_i, p_{i'}] = i\hbar \delta_{ii'}$ and $[q_i, q_{i'}] = [p_i, p_{i'}] = 0$. If we rotate the operators in the following way,

$$\hat{a}_i = \frac{e^{-i\nu_i t}}{\sqrt{2m_i \hbar \nu_i}} (m_i \nu_i \hat{q}_i + i\hat{p}_i), \qquad (1.23)$$

we find that the equations are simplified and have a straightforward meaning. The operator $\hat{a}_i$ is the annihilation operator for the ith mode, in reference to the well

known solutions to the quantum harmonic oscillator. With this substitution, the quantum Hamiltonian becomes

$$\hat{\mathcal{H}} = \sum_i \hbar\nu_i \left(\hat{a}_i^\dagger \hat{a}_i + \frac{1}{2} \right), \tag{1.24}$$

with electric and magnetic field operators given by

$$\hat{E}_x(z,t) \;=\; \sum_i \mathcal{E}_i (\hat{a}_i e^{-i\nu_i t} + \hat{a}_i^\dagger e^{i\nu_i t}) \sin(k_i z), \tag{1.25}$$

$$\hat{H}_y(z,y) \;=\; -i\epsilon_0 c \sum_i \mathcal{E}_i (\hat{a}_i e^{-i\nu_i t} - \hat{a}_i^\dagger e^{i\nu_i t}) \cos(k_i z), \tag{1.26}$$

where $\mathcal{E}_i = (\hbar\nu_i/\epsilon_0 V)^{1/2}$ has dimensions of electric field and c is the speed of light. We see that both field operators have counter-rotating frequency terms, and are therefore typically split into their positive and negative frequency parts, where e.g., $\hat{E}^{(+)}$ contains only annihilation operators. Also, note that the specifics of the longitudinal (z-direction) sine terms will vary with the geometry of the system under study.

Since photons often do not interact strongly with their environment—which is one reason for their usefulness in quantum communication—this free space calculation is particularly suited to our application. We will use the creation and annihilation operators to describe the field in the following chapters, but for a more detailed description of quantization see references [4, 8, 9].

1.2 The Weak Value

1.2.1 Original Formulation

It is commonly thought that any average of a quantum operator must be bounded between the smallest and largest of its eigenvalues. This can be seen by writing the expectation value for an operator $\hat{O}$ with discrete eigenvalues $\{o_i\}$ as

$$\langle \hat{O} \rangle = \sum_i o_i p_i, \tag{1.27}$$

where $0 \leq p_i \leq 1$ are the probabilities for each outcome i. This notion was shown to be incorrect by Aharonov, Albert, and Vaidman (AAV), who introduce the concept of a *weak value* in their seminal 1988 paper in Physical Review Letters [10]. For example, AAV described how it would be possible to measure a (post-selected) spin-1/2 particle to have $\langle \sigma_z \rangle = 100$. In order to realize this effect, four steps are traditionally carried out: quantum state preparation (pre-selection), a weak perturbation, post-selection on a final quantum state and a projective readout of a continuous variable. The weak perturbation can result in a large shift of the appropriate continuous variable, which constitutes a measurement (described below).

We can think of the weak value as the average of measurement results over only a sub-set of the data that corresponds to a prescribed outcome of a projective measurement (post-selection). While initially controversial [11, 12], the prediction of strange weak values that lie outside the range of the observable's eigenvalues has been experimentally confirmed in the field of quantum optics [13–21], and recent proposals exist in condensed matter systems as well [22–24].

Weak values are an interesting phenomenon, because they assist us in understanding many counterintuitive quantum results. For example, weak values can be used as a fundamental test of quantum mechanics by ruling out a class of macro-realistic hidden variable theories and are equivalent to the violation of generalized Leggett-Garg inequalities [22]. Weak values have been useful to help resolve paradoxes that arise in quantum mechanics such as Hardy's paradox [25, 26], apparent superluminal travel [27], the Cheshire Cat [28] and more general counterfactual quantum problems such as the three-box problem [11]. With weak values, it is also possible to make meaningful, sequential measurements of noncommuting observables [29].

Aside from the fundamental physics interest in weak values, it has been realized that they are also useful. The utility of weak values has been dramatically

demonstrated by Hosten and Kwiat [30] who were able to detect a polarization-dependent beam deflection of 1 Å. Connections between weak values and other areas of physics include tunable delay lines using fast and slow light in bulk media [31] and fiber optics [32, 33], as well as weak value inspired cross phase modulation amplification [34].

In order to give a complete account, we shall start at the beginning. The initial derivation [10], and a subsequent correction [12], are what follows. AAV considered a single particle and a detector in separable quantum states. The state of the detector is Gaussian with conjugate canonical operators $\hat{x}$ and $\hat{p}$, which are often called *meter* variables. We can write this initial state in either basis,

$$|\phi_i\rangle = \int dx\, \phi(x)|x\rangle = \int dp\, \widetilde{\phi}(p)|p\rangle, \tag{1.28}$$

where $\phi(x)$ and $\widetilde{\phi}(p)$ are the x and p wavefunctions for the detector. For a Gaussian meter state, we write $\phi(x) = \exp[-x^2/4(\Delta x)^2]$ and $\widetilde{\phi}(p) = \exp[-p^2/4(\Delta p)^2]$, where $\Delta x = 1/2\Delta p$ and we have ignored the normalization constants.

The particle under question is often called the *system*, with the measurement of interest $\hat{A}$ known as the system operator. The state of the system is written as

$$|\psi_i\rangle = \sum_j c_j |a_j\rangle, \tag{1.29}$$

where c_i is the probability amplitude for the ith eigenstate $|a_i\rangle$ with corresponding eigenvalue a_i. Therefore, the initial state for both the system and meter can be written as the separable state

$$|\Psi_i\rangle = |\phi_i\rangle \otimes |\psi_i\rangle = \sum_j \int dx\, e^{-x^2/4(\Delta x)^2} c_j |x\rangle \otimes |a_j\rangle, \tag{1.30}$$

where $\otimes$ signifies a tensor product connecting two states from separate Hilbert spaces. The system and meter are then coupled together via an interaction Hamiltonian in order to measure $\hat{A}$ using the detector. The interaction Hamiltonian is of the form

$$\hat{H} = -g(t)\hat{A}\hat{x}, \tag{1.31}$$

where $g(t)$ is the normalized time-dependent strength of the coupling and $\hat{A}$ and $\hat{x}$ operate in different spaces. We will assume throughout that $g(t) = \delta(t - t_0)$ is the Dirac delta function and t_0 is the moment in time of the interaction. This means that our particle couples to the detector at t_0 in a short amount of time. We also assume that, during the interaction, $\hat{H}$ represents the total Hamiltonian.

We then apply the interaction to our initial state to get

$$\hat{U}|\Psi_i\rangle \;=\; e^{-\frac{i}{\hbar}\int \hat{H}dt}|\Psi_i\rangle \tag{1.32}$$

$$=\; e^{\frac{i}{\hbar}\hat{A}\hat{x}}\sum_j \int dx\, e^{-x^2/4(\Delta x)^2}c_j|x\rangle \otimes |a_j\rangle \tag{1.33}$$

$$=\; \sum_j \int dx\, e^{\frac{i}{\hbar}a_j x}e^{-x^2/4(\Delta x)^2}c_j|x\rangle \otimes |a_j\rangle \tag{1.34}$$

$$=\; \sum_j \int dp\, e^{-(p-a_j)^2/4(\Delta p)^2}c_j|p\rangle \otimes |a_j\rangle, \tag{1.35}$$

where we used an insertion of $\hat{1} = \int dp\,|p\rangle\langle p|$ and note that $\langle p|x\rangle \propto \exp(ipx/\hbar)$. If we inspect each term in the sum separately, we see that each system eigenstate corresponds to a Gaussian in p centered on the eigenvalue a_i. If Δp is sufficiently small, such that $|a_j - a_{j'}| > \Delta p$ for $j \neq j'$, then we find that each term in the summation is well-separated in p from the next, and we have a strong measurement. Knowing the distribution of $\hat{U}|\Psi_i\rangle$ in p tells us the corresponding coefficients c_j. That is, we have made a measurement of A indirectly via a measurement of the meter.

However, if the separation of the eigenvalues a_i are not larger than the spread of the meter, then a single measurement of $\hat{p}$ is not sufficient to determine which eigenstate that measurement represents. This constitutes a weak measurement. However, by repeating the measurement many times on identically prepared particles and detectors, we can obtain the distribution with any desired uncertainty and therefore eventually find the amplitudes $\{c_j\}$.

An interesting result is obtained if we take this one step further. Let us choose

to filter the results at the end by post-selecting on a particular quantum state of the system, say

$$|\psi_f\rangle = \sum_j b_j |b_j\rangle. \tag{1.36}$$

This process is very similar to the initial preselection of $|\psi_i\rangle$ and, experimentally, is quite simple. We then find, with the help of a Taylor expansion, that

$$
\begin{aligned}
\langle\psi_f|\hat{U}|\Psi_i\rangle &= \langle\psi_f|e^{-i\hat{A}\hat{x}/\hbar}|\psi_i\rangle \otimes |\phi_i\rangle \\
&\approx \langle\psi_f|(1 + i\hat{A}\hat{x}/\hbar + ...)|\psi_i\rangle \otimes |\phi_i\rangle \\
&= (\langle\psi_f|\psi_i\rangle + i\hat{x}\langle\psi_f|\hat{A}|\psi_i\rangle/\hbar + ...) \otimes |\phi_i\rangle \\
&= \langle\psi_f|\psi_i\rangle(1 + i\hat{x}\langle\psi_f|\hat{A}|\psi_i\rangle/\langle\psi_f|\psi_i\rangle\hbar + ...) \otimes |\phi_i\rangle \\
&\approx \langle\psi_f|\psi_i\rangle e^{-iA_w\hat{x}/\hbar}|\phi_i\rangle \\
&= \langle\psi_f|\psi_i\rangle \int dx\, e^{-iA_w x/\hbar}\phi(x)|x\rangle \\
&= \langle\psi_f|\psi_i\rangle \int dp\, \widetilde{\phi}(p - A_w)|p\rangle,
\end{aligned}
\tag{1.37}
$$

where

$$A_w :=_f \langle\hat{A}\rangle_i = \frac{\langle\psi_f|\hat{A}|\psi_i\rangle}{\langle\psi_f|\psi_i\rangle} \tag{1.38}$$

is the weak value. The end result is a single Gaussian shifted not by an eigenvalue of $\hat{A}$, but by the weak value A_w, with an overall attenuation given by the prefactor $\langle\psi_f|\psi_i\rangle$. The approximations here are valid only for certain limits [12] given by $\Delta x \ll A_w^{-1}$ and

$$\Delta x \ll \min \left|\frac{\langle\psi_f|\hat{A}|\psi_i\rangle}{\langle\psi_f|\hat{A}^n|\psi_i\rangle}\right|^{(n-1)^{-1}}. \tag{1.39}$$

Within these limits, we find that A_w can be quite large, giving a result where $_f\langle\hat{A}\rangle_i$ (a pre- and post-selected ensemble average) can lie far outside the eigenvalue spectrum of $\hat{A}$. If we were to measure the spin of an electron (system) by looking at how far it would deflect (meter) after passing through an inhomogeneous magnetic field, our detected electrons would deflect on average much farther than they should given their spin. If we think of this measurement result as an

amplification, one might ask: can we use this technique to measure small quantities with increased precision? We will address this question after a more modern description of this effect.

1.2.2 Contextual Value Formulation

Weak values arise from of a particular choice of our measurement apparatus, and in particular, the value assignments we make for our measurement results [35]. It may come as a surprise that a measurement of some observable $\hat{A}$ greatly depends on the way in which we make the measurement. However, it is this point which will shed some light on the somewhat unusual measurement technique producing a weak value.

Consider a particle in a quantum state ρ, and an observable $\hat{A}$ that we wish to study. The standard way of computing the average of this observable is

$$\langle \hat{A} \rangle = \sum_i a_i P_i = \sum_i a_i \text{Tr}(\hat{\Pi}_i \rho), \tag{1.40}$$

where $\{a_i\}$ are the eigenvalues of $\hat{A}$ and P_i and $\hat{\Pi}_i$ are the probability of and the projector onto the ith eigenstate, respectively. In order to perform this task in the laboratory, we must have some way of separating out each eigenstate by performing projective measurements. From the statistics of such a measurement, the average of $\hat{A}$ can be computed.

The question arises: what if our measurement apparatus is not projective in nature? What information can we learn about our state ρ, or our observable $\hat{A}$? These questions can be answered in the context of POVMs. Consider an apparatus which is not necessarily projective $\{\Pi_i\}$, but instead may be weak in nature $\{\hat{M}_i\}$. The corresponding POVM is simply $\{\hat{E}_i = \hat{M}_i^\dagger \hat{M}_i\}$. As before, the result of each measurement has a probability given by $P_i = \text{Tr}(\hat{E}_i \rho)$. However, if

we want to represent our observable $\hat{A}$ in terms of this measurement context, we can no longer use the eigenvalues:

$$\hat{A} = \sum_i a_i \hat{\Pi}_i = \sum_j \alpha_j \hat{E}_j, \tag{1.41}$$

where $\{\alpha_j\}$ are the contextual values.

In order to reproduce the results of AAV, we simply generate the weak value scenario by choosing the appropriate $\{\hat{M}_k\}$ (or equivalently, $\{\hat{E}_k\}$). That is,

$$\hat{M}_k = \hat{M}_f \hat{M}_w \hat{M}_i, \tag{1.42}$$

where $\hat{M}_i$ is the initial pre-selection (e.g., $\hat{M}_i = |\Psi_i\rangle\langle\Psi_i|$), $\hat{M}_f$ is the post-selection, and $\hat{M}_w$ is the intermediate weak perturbation. With this measurement context, the average of $\hat{A}$ is then given by

$$_f\langle\hat{A}\rangle_i = \frac{\sum_k \alpha_k \text{Tr}(\hat{E}_k \rho)}{\sum_k \text{Tr}(\hat{E}_k \rho)}, \tag{1.43}$$

where the denominator is the renormalization factor from the conditioned average. A straightforward calculation shows that Eq. (1.43) reproduces the AAV result of $_f\langle\hat{\sigma}_z\rangle_i = \tan(\theta/2)$ [10] in the limit of a weak intermediate perturbation. We therefore see that a weak value is nothing more than a conditioned average in a particular measurement context. That is, the weak value depends not only on the input state ρ and the quantity of interest $\hat{A}$, but also on the measurement apparatus. In the next section we will consider the usefulness of the weak value in an optics experiment.

1.2.3   Weak Values: Optics Experiments

Let us consider weak values in the context of optical experiments. It was quickly realized that one can test the work of AAV using laser radiation, and in 1991, the lab of Randy Hulet demonstrated a weak value [14]. Their proposal coupled the
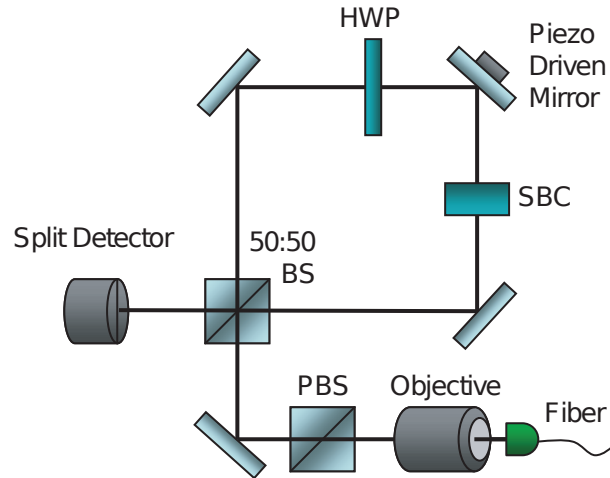
Figure 1.1: Proposed experimental setup for an interferometric weak value deflection measurement

transverse position or momentum of the beam (the meter) with the polarization degree of freedom of the photons (the system) using a birefringent crystal. They were able to show an amplification of 20 of the beam displacement upon postselection. In 2008, Hosten and Kwiat were able to demonstrate an *imaginary* weak value with a similar design, obtaining an amplification of nearly 10000. Using this technique, they were able to measure the spin hall effect of light at the interface of a glass prism [30]. In what follows, we will describe the theory for a measurement of the deflection of a beam using interferometric weak values [15].

It is important to note that all two dimensional quantum systems are isomorphic to spin-1/2 particles. In the Hosten-Kwiat experiment, the two dimensional system was the circular polarization states of the light $\{|+\rangle, |-\rangle\}$. For the interferometric design, we consider the which-path states of a photon in a Sagnac interferometer as the two-state system (see Fig. 1.1). That is, the two paths in the interferometer (clockwise and counterclockwise) can be denoted by the states $\{|\circlearrowright\rangle, |\circlearrowleft\rangle\}$.

Consider Fig. 1.1. Radiation from a fiber-coupled laser is launched into free

space. The beam is polarized by a polarizing beam splitter (PBS) and then enters a Sagnac interferometer which consists of three mirrors, a 50:50 BS, a half-wave plate (HWP) and a Soleil-Babinet compensator (SBC). The SBC and HWP in the interferometer adjust the relative phase between the two paths and allow the output intensity of the interferometer to be tuned. The output port is monitored with a split detector, i.e., a detector which subtracts the intensity striking its left and right sides. The piezo driven mirror gives a small beam deflection.

We will consider one photon at a time, ignoring the coherent nature of the laser radiation. This is valid, as will be shown later, due to the linear nature of the experimental apparatus. The photon's which-path (system) variable is coupled to its transverse momentum (meter) variable. We write the system eigenstates as $\{|\circlearrowleft\rangle, |\circlearrowright\rangle\} \equiv \{|a_i\rangle\}$ and the meter eigenstates as $\{|k_x\rangle\}$, where x is the transverse direction in the plane of the page and so k_x is the transverse momentum of the photons. The pre-selected total state of the photon is the tensor product of the system and meter states, written as

$$|\Psi\rangle = \int dk_x \widetilde{\phi}(k_x) \hat{a}_{k_x}^\dagger |0\rangle \otimes |\psi_i\rangle, \tag{1.44}$$

where $\hat{a}_{k_x}^\dagger$ is the usual creation operator for the transverse mode k_x, $|\psi_i\rangle = \sum_i c_i |a_i\rangle$ is the input system state of the photon, $\{c_i\}$ are the probability amplitudes for the system states, and $\widetilde{\phi}(k_x)$ is the transverse momentum wavefunction. We will assume that $\widetilde{\phi}(k_x)$ [and therefore $\phi(x)$] is a Gaussian in order to obtain an analytic solution.

We now describe the weak measurement procedure. First, the photon undergoes a small unitary evolution, which couples one of the propagation directions in the interferometer to one momentum shift, given by k, and the other direction to another momentum shift, given by $-k$ (relative to the optical axis at the exit face of the BS for a symmetric interferometer). In essence, the momentum shift k, upon detection, gives a small amount of which-path information about the

photon. The unitary evolution is given by $\hat{U} = e^{-ik\hat{A}\hat{x}} \approx 1 - ik\hat{A}\hat{x}$, where $\hat{A}$ is the which-path observable with eigenvalues given by $\hat{A}|a_i\rangle = a_i|a_i\rangle$. The Taylor expansion is valid only for small momentum kicks k relative to the width of the distribution in k_x. The post-selection occurs at the 50:50 BS by monitoring the so-called "dark port."

For simplicity, the calculation here will assume a collimated beam with no divergence. For very small momentum kicks and short propagation distances, the deflection in the detection plane is very small compared to the transverse diameter of the beam, and thus the system eigenstates are only weakly discriminated. When the photon passes through the BS for the second time, there is a post-selection on the state $|\psi_f\rangle$ which is nearly orthogonal to the input state. This yields a post-selected meter state

$$\langle\psi_f|U|\Psi\rangle \approx \int dk_x \widetilde{\phi}(k_x)\hat{a}_{k_x}^\dagger|0\rangle\langle\psi_f|\psi_i\rangle$$
$$- i\int dk_x \widetilde{\phi}(k_x)kx\hat{a}_{k_x}^\dagger|0\rangle\langle\psi_f|\hat{A}|\psi_i\rangle. \tag{1.45}$$

As can be seen, if the pre- and the post-selected system states are nearly orthogonal, the probability for the photon to pass through the post-selecting device (i.e. the BS) is small. However, for the photons that do pass through, we must renormalize the single photon meter state. We define the renormalized state as

$$|\Psi'\rangle = \int dk_x \widetilde{\phi}(k_x)\hat{a}_{k_x}^\dagger|0\rangle$$
$$- i\int dk_x \widetilde{\phi}(k_x)kx\hat{a}_{k_x}^\dagger|0\rangle\frac{\langle\psi_f|\hat{A}|\psi_i\rangle}{\langle\psi_f|\psi_i\rangle}, \tag{1.46}$$

where $A_w = \frac{\langle\psi_f|\hat{A}|\psi_i\rangle}{\langle\psi_f|\psi_i\rangle}$ is the standard weak value term. We can calculate its value by recognizing that the eigenvalues of $\hat{A}$ are ± 1 for the two directions in the interferometer, which encodes the fact that the deflections are in opposite directions in the detection plane. The pre-selected state $|\psi_i\rangle$ is determined by the

properties of the BS and the relative phase δ between the two paths, controlled by the SBC. Explicitly, the pre- and post-selected system states are given by

$$|\psi_i\rangle = \frac{1}{\sqrt{2}}(e^{-i\frac{\delta}{2}}|\circlearrowright\rangle + e^{i\frac{\delta}{2}}|\circlearrowleft\rangle) \tag{1.47}$$

$$|\psi_f\rangle = \frac{1}{\sqrt{2}}(|\circlearrowright\rangle - |\circlearrowleft\rangle). \tag{1.48}$$

We then see that $\langle\psi_f|\psi_i\rangle = i\sin(\frac{\delta}{2})$ and $\langle\psi_f|\hat{A}|\psi_i\rangle = \cos(\delta/2)$. Thus,

$$A_w = \frac{\langle\psi_f|\hat{A}|\psi_i\rangle}{\langle\psi_f|\psi_i\rangle} = -i\cot(\phi/2) \tag{1.49}$$

is purely imaginary.

As long as the second term on the right hand side is much smaller than the first of Eq. (1.46), we can reexponentiate the Taylor expansion to obtain

$$|\Psi'\rangle = \int dk_x \widetilde{\phi}(k_x)e^{-ikA_w x}\hat{a}^\dagger_{k_x}|0\rangle. \tag{1.50}$$

To obtain the probability amplitude distribution in the transverse plane, we define a positive frequency field operator

$$\hat{E}^{(+)}(x) = E_0 \int dk_x e^{-ik_x x}\hat{a}_{k_x}, \tag{1.51}$$

where E_0 is the electric field amplitude. To look at a single photon detection, we post-select on the single photon state $\hat{E}^{(-)}(x)|0\rangle$. Using the commutation relation $[\hat{a}_{k'_x}, \hat{a}^\dagger_{k_x}] = \delta(k'_x - k_x)\hat{1}$, the state becomes

$$\langle 0|\hat{E}^{(+)}(x)|\Psi'\rangle = E_0 \int dk_x e^{-ik_x x}\widetilde{\phi}(k_x)e^{-ikA_w x}. \tag{1.52}$$

From this point, we will drop the normalization of the state and consider a Gaussian wavefunction, such as the single mode output of a laser. Using the fact that $A_w \approx i2/\delta$ for small δ, we find

$$\begin{aligned}
\langle 0|\hat{E}^{(+)}(x)|\Psi'\rangle &\propto e^{\frac{-2kx}{\delta}} \int dk_x e^{-ik_x x}e^{-k_x^2\sigma^2} \\
&= \exp\left[-\frac{x^2}{4\sigma^2} - \frac{2kx}{\delta}\right],
\end{aligned} \tag{1.53}$$

where σ is the Gaussian beam radius. After completing the square,

$$\langle 0|\hat{E}^+(x)|\Psi'\rangle \propto \exp\left[-\frac{1}{4\sigma^2}\left(x + \frac{4k\sigma^2}{\delta}\right)^2\right]. \qquad (1.54)$$

One can see that, at the detector, there will be a transverse position shift of the photons given by $d_w = 4k\sigma^2/\delta$, where we denote d_w as the weak value transverse deflection.

If we remove the BS and allow the beam to propagate to the detector without interference, the deflection of the beam in the detection plane is given by $d \approx lk/k_0$, where l is the length the beam propagates from the mirror to the detector and $k_0 = 2\pi/\lambda$ is the wave number of the photon. The amplification is therefore given by $d_w/d = 4\sigma^2 k_0/\delta l \gg 1$ for a wide range of experimentally feasible parameters.

1.2.4   Weak Values: Are They Classical?

As we have seen, the original formulation of the weak value was purely quantum mechanical in nature [10]. However, many experiments in the optical domain [14, 15, 30] have used coherent quasi-classical fields and no apparent quantum mechanical system was employed. The "classical" behavior of these weak value deflection measurements has been known for some time. In fact, shortly after the Hosten and Kwiat paper, Aiello and Woerdman [36] published the classical description of their results to allow greater accessibility to the metrology community. In what follows, we will derive the previous result from a classical electrodynamics point of view under the corresponding limits.

Consider the transverse two-port input field of the interferometer as

$$\boldsymbol{E}_{in} = \begin{pmatrix} E_0\, e^{-x^2/4\sigma^2} \\ 0 \end{pmatrix}, \qquad (1.55)$$

where the second position in the column vector denotes the input port with no electric field (left to right in Fig. 1.1). The field then passes through a 50:50 BS with a matrix representation

$$\boldsymbol{B} = \frac{1}{\sqrt{2}} \begin{pmatrix} 1 & i \\ i & 1 \end{pmatrix}. \tag{1.56}$$

We now define a matrix which gives both an opposite momentum shift k and a relative phase between the two paths

$$\boldsymbol{M} = \begin{pmatrix} e^{i(-kx+\phi/2)} & 0 \\ 0 & e^{-i(-kx+\phi/2)} \end{pmatrix}. \tag{1.57}$$

We want to determine the field at the location of the detector, known as the "dark" output port of the interferometer (i.e., the port with the lowest intensity of light coming out of it). The evolution of the light is represented by the matrix combination

$$\boldsymbol{E}_{out} = (\boldsymbol{BMB})\boldsymbol{E}_{in}. \tag{1.58}$$

The output field at the dark port is renormalized by $\sin(\phi/2)$ by noting that the position detector records only the incident field. For small k, the measured output signal (renormalized) at the dark port will be of the form

$$E_{out}^d = \frac{\sin(-kx + \phi/2)}{\sin(\phi/2)} \exp[-x^2/4\sigma^2]. \tag{1.59}$$

For small angles, we obtain

$$E_{out}^d \approx \left(1 - \frac{2kx}{\phi}\right) \exp[-x^2/4\sigma^2], \tag{1.60}$$

which we exponentiate and, after completing the square in the exponent, find

$$E_{out}^d \propto \exp\left[-\frac{1}{4\sigma^2}\left(x + \frac{4k\sigma^2}{\phi}\right)^2\right]. \tag{1.61}$$

Note the similarity in this procedure to our previous derivation: Taylor expanding, exponentiating, and completing the square. We see that we obtain the same

deflection as the quantum mechanical weak value treatment. It would therefore seem as though we do not require quantum mechanics to produce a weak value, and that perhaps the only requirement is a system that exhibits interference. Some may argue, however, that electromagnetic interference is indeed a quantum effect, and point to the similarities between the relevant equations of Maxwell and Schrödinger.

For precision measurements of beam deflections, it is advantageous to construct a compact interferometer for stability reasons. Therefore, the effects of beam divergence are typically minimal. For a detailed classical treatment of these effects, see reference 37.

1.2.5 Real Versus Imaginary Weak Values

In our derivations thus far, we have made no assumptions about whether A_w was real, imaginary or complex. Depending on the situation, A_w can take on any of these possibilities. In the case of Ritchie *et al.* [38], A_w was purely real. In contrast, Hosten *et al.* [30] and Dixon *et al.* [15] demonstrated purely imaginary weak values (as seen above). Recently, Dressel and Jordan discussed the significance of the imaginary part of the weak value [39]. They state,

> Unlike the real part of the generalized weak value of an observable, which can in a restricted sense be operationally interpreted as an idealized conditioned average of that observable in the limit of zero measurement disturbance, the imaginary part of the generalized weak value does not provide information pertaining to the observable being measured. What it does provide is direct information about how the initial state would be unitarily disturbed by the observable operator.

For our purposes, let us consider the case derived in Eq. (1.37), where after post-selection, the wavefunction gets a shift $\widetilde{\phi}(p) \rightarrow \widetilde{\phi}(p - A_w)$. If we make the

reasonable assumption that our wavefunction is Gaussian, such that

$$\phi(x) = \exp[-x^2/4(\Delta x)^2], \tag{1.62}$$

$$\widetilde{\phi}(p) = \exp[-p^2/4(\Delta p)^2], \tag{1.63}$$

are Fourier transform pairs, where $\Delta q = 1/2\Delta p$, then we can consider the general case when $A_w = A'_w + iA''_w$ is complex. Looking at the shifted momentum wavefunction, we find that

$$\widetilde{\phi}(p - A_w) = e^{-(p-A_w)^2/4(\Delta p)^2} \tag{1.64}$$

$$= \underbrace{e^{-\frac{(p-A'_w)^2}{4(\Delta p)^2}}}_{1} \times \underbrace{e^{-\frac{(A''_w)^2}{4(\Delta p)^2}}}_{2} \times \underbrace{e^{-i\frac{A''_w(p-A'_w)}{2(\Delta p)^2}}}_{3} \tag{1.65}$$

Term 1 is the familiar shift of the momentum wavefunction for a real weak value. Term 2 shows that there is an overall attenuation when the weak value has an imaginary part, an issue that we shall come to later. Term 3 provides an oscillation of the momentum wavefunction.

To understand this oscillation in more detail, let us consider a purely imaginary weak value (such as in references [15, 30]), where we know that we obtain a large amplification in the position domain. To see this, let $A_w = iA''_w$ be imaginary. Then, ignoring normalization and attenuation, the post-selected state in the position basis becomes

$$\phi_w(x) = \mathcal{F}_p^{-1}[\widetilde{\phi}(p - iA''_w)] \tag{1.66}$$

$$= \mathcal{F}_p^{-1}\left[\exp\left[-\frac{p^2}{4(\Delta p)^2}\right]\exp\left[-i\frac{A''_w p}{2(\Delta p)^2}\right]\right] \tag{1.67}$$

$$= \phi(x - A''_w/2(\Delta p)^2), \tag{1.68}$$

where we have used the shift property of Fourier transforms in the final line. Therefore, by changing A_w from real to imaginary, we move the shift from the momentum wavefunction to the position wavefunction. Interestingly, the size of Δp can have a large impact on the size of the shift. In the case of photon propagation, a change of basis such as this can be obtained simply by propagation
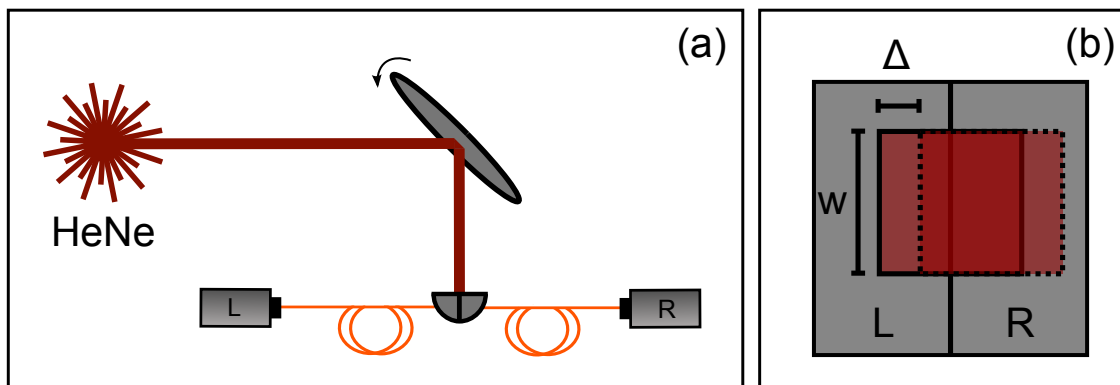
Figure 1.2: A square shaped laser beam from a Helium-Neon (HeNe) laser source incident on a split detector.

or with the use of a lens. Therefore, access to measurements in either basis is readily available.

1.2.6   Signal-to-Noise Ratio

We have thus far made a point of ignoring the effect of the small post-selection probability associated with our resultant state. This small probability translates to a small number of detection events for an ensemble of identically prepared, transformed and post-selected quantum objects. Importantly, the statistics of our ensemble can have a large impact on our measurement precision; we know that measurement precision often increases with the number of detection events. Therefore, what can be said of the SNR for the scheme as presented above, where large amounts of photons are never detected? The complete answer to this question will come in chapter two. For now, let us evaluate this peculiarity from a simpler perspective.

Consider a beam of light, emitted from a laser source, incident on a split-detector as shown in Fig. 1.2a. We begin by asking the following question: what is the average position of the beam on the detector, and what is the uncertainty

in this position? To answer this question in full, we must consider the nature of the incident light.

While the electromagnetic field in classical electrodynamics can have a well defined amplitude and phase, such is not the case in quantum mechanics. One might point out that a number state of light $|n\rangle$ has a perfectly known amplitude. However, the phase of such a state is completely uncertain. These two quantities (amplitude and phase) obey a form of Heisenberg's uncertainty relation. So, if it impossible to perfectly represent a classical field in quantum mechanics, what is a good approximation? We need only look to the eigenstates of the annihilation operator (or, equivalently, $\hat{E}^{(+)}$) to find an answer.

Let us consider the state $|\alpha\rangle$ as an eigenstate of the annihilation operator with eigenvalue α. That is,

$$\hat{a}|\alpha\rangle = \alpha|\alpha\rangle. \tag{1.69}$$

We are assuming a single mode field, taking only one term from Eq. (1.25). We also assume that the coherent state can be expanded in the number basis, so $|\alpha\rangle = \sum_n c_n |n\rangle$. By remembering that $\hat{a}|n\rangle = \sqrt{n}|n-1\rangle$, inserting the expansion of $|\alpha\rangle$ into Eq. (1.69), matching coefficients on each side and then normalizing, we obtain

$$|\alpha\rangle = e^{-|\alpha|^2/2} \sum_{n=0}^{\infty} \frac{\alpha^n}{\sqrt{n!}} |n\rangle. \tag{1.70}$$

By expressing $|\alpha\rangle$ in the coordinate representation ($\langle q|\alpha\rangle$ and $\langle p|\alpha\rangle$), one finds that the coherent state satisfies the minimum uncertainty relation $\Delta q \Delta p = \hbar/2$. This may be surprising, since the constituents of the coherent state ($\{|n\rangle\}$) have $\Delta q \Delta p = (n + 1/2)\hbar \geq \hbar/2$. Furthermore, the coordinate representation of $|\alpha\rangle$ is the wave packet that coheres (or sticks together) when subjected to a harmonic potential. For this reason, we consider the coherent state the most accurate representation of the classical electromagnetic field, and use this representation when discussing radiation from a laser operating well above threshold [8].
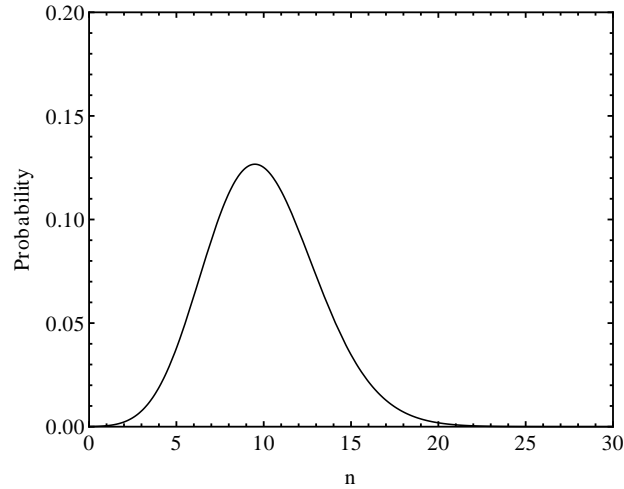
Figure 1.3: Poisson distribution exhibiting the counting statistics of laser radiation with $\langle n \rangle = 10$.

One might recognize the form of the coefficients of $|\alpha\rangle$, and if we look at the probability of finding n photons in our coherent state, we obtain

$$
\begin{aligned}
p(n;\alpha) &= \langle n|\alpha\rangle\langle\alpha|n\rangle \\
&= \frac{|\alpha|^{2n}e^{-|\alpha|^2}}{n!} \\
&= \frac{\langle n\rangle^n e^{-\langle n\rangle}}{n!}
\end{aligned}
\tag{1.71}
$$

with mean $\langle n \rangle = |\alpha|^2$. This is the well known Poisson distribution which describes the statistics of random events, ranging from applications in biology and civil engineering to radiation events from unstable elements. For our purposes, we note that the average number of photons in a coherent state $|\alpha\rangle$ is $|\alpha|^2$, with the probability distribution shown in Fig. 1.3. Due to the width of this distribution, it is clear that the total number of photons for a given coherent state will fluctuate; for the Poisson distrubution in Eq. (1.71), the standard deviation is $\sqrt{\langle n \rangle}$.

Let us return to the question at hand: what is the average position of the beam on the detector (in Fig. 1.2a), and what is the uncertainty in this position? Consider a simple system with a square beam of width w and height w, as shown

in Fig. 1.2b. The beam is initially centered on the detector; then, a small shift is given to the beam position by an amount Δ as shown. The split detector records the power (or number of photons) incident on each side. From this, we can determine the position of the beam (assuming we know its shape).

The observable for our position measurement is defined to be $\hat{s} = \hat{n}_R - \hat{n}_L$, where $\hat{n}_{R,L}$ corresponds to the number of photons incident on the right (R) or left (L) side of the detector. For a coherent state, we can compute the expectation value of our signal $\langle \hat{s} \rangle = \langle \hat{n}_R \rangle - \langle \hat{n}_L \rangle$, and relate this to the geometry from Fig. 1.2b,

$$\hat{s} = \hat{n}\frac{w/2 + \Delta}{w} - \hat{n}\frac{w/2 - \Delta}{w} = 2\frac{\Delta}{w}\hat{n}, \tag{1.72}$$

where $\hat{n} = \hat{n}_L + \hat{n}_R$. That is, Δ is determined by $\hat{s}$ such that $\langle \hat{s} \rangle = 2\Delta\langle \hat{n} \rangle/w$. However, to determine the SNR for this measurement, we compute

$$\mathcal{R} = \frac{\langle \hat{s} \rangle}{\sqrt{(\Delta\hat{s})^2}}. \tag{1.73}$$

By noting that $[\hat{n}_L, \hat{n}_R] = 0$ and that $\langle \hat{n}_L \hat{n}_R \rangle = \langle \hat{n}_L \rangle \langle \hat{n}_R \rangle$, we find that

$$\mathcal{R} = \frac{2\Delta\langle \hat{n} \rangle}{w\sqrt{\langle \hat{n} \rangle}} = \frac{2\Delta\sqrt{\langle \hat{n} \rangle}}{w}. \tag{1.74}$$

We have thus shown that the SNR scales as $\sqrt{\langle \hat{n} \rangle}$ and is linear in the beam displacement Δ. Thus, due to the quantum mechanical nature of our "classical" light source, there are fluctuations in the laser intensity (often called shot noise) which result in reduced measurement precision. By using a more intense laser source, or by collecting more photons, the SNR will increase.

In the case of weak values, we know that the displacement imparted to the beam Δ is amplified, and yet the number of photons incident on the detector $\langle \hat{n} \rangle$ is reduced. Therefore, these two effects compete. A detailed discussion $\mathcal{R}$, post-selection and amplification will be presented in chapter two.

1.3 Interaction of Light and Matter

1.3.1 Interaction Hamiltonian

In chapter four, we will present an experiment on how one can use laser radiation tuned near the resonances of rubidium (Rb) to perform accurate measurements of optical frequency as well as guide probe light. Therefore, in the present section, we discuss the general theory of the interaction of light and matter.

We have already seen how a quantum description of the electromagnetic field is necessary to understand the intensity fluctuations of laser radiation. However, we need not turn to the quantized electric field in every instance. In fact, a great many results can be accurately predicted from the classical description of the electric field.

Let us consider a quantum mechanical atom with one valence electron that can populate any number of quantum states $\{|1\rangle, |2\rangle, |3\rangle, ...\}$. The first column of the periodic table, composed of hydrogen and the alkali metals, are prime examples. In the experiments presented in chapter four, we use Rb gas.

The evolution of an electron in an atom is of course described by its Hamiltonian $\hat{H}$. If we apply a classical electric field and we choose to describe the atom quantum-mechanically, we can then write

$$\hat{H} = \hat{H}_0 + \hat{H}_i, \tag{1.75}$$

where $\hat{H}_0$ is the unperturbed Hamiltonian of the electron given by

$$\hat{H}_0 = \sum_n \hbar\omega_n |n\rangle\langle n|, \tag{1.76}$$

with $\hbar\omega_n$ the energy of the nth level, and

$$\hat{H}_i \approx -e\hat{\mathbf{r}} \cdot \mathbf{E}(\mathbf{r}_0, t) \tag{1.77}$$

is the interaction Hamiltonian in the dipole approximation that describes the interaction between the electron (with charge e) and the time varying electric field. Notice that the electric field is a classical vector.

There are a variety of ways of solving the Schrödinger equation. Perhaps the most compact and useful form is in the density matrix representation, where

$$\dot{\hat{\rho}} = -\frac{i}{\hbar}[\hat{H}, \hat{\rho}]. \tag{1.78}$$

Given some initial state $\hat{\rho}_0$, we can solve for $\hat{\rho}(t)$. We can even include phenomenological decay terms via a relaxation matrix Γ, resulting in

$$\dot{\hat{\rho}} = -\frac{i}{\hbar}[\hat{H}, \hat{\rho}] - \frac{1}{2}\{\Gamma, \rho\}. \tag{1.79}$$

The solutions to these equations under specific conditions result in well known phenomena such as Rabi oscillation, population inversion, Stark shifts and more. Let us consider the simple case of a two level atom interacting with a single mode laser field, ignoring the contribution of excited state decay.

The two states of the atom can be written as $\{|a\rangle, |b\rangle\}$, with $|a\rangle$ as the ground state and $|b\rangle$ as the excited state. The Hamiltonian is then given by Eq. (1.75), with $\hat{H}_0$ consisting of two terms and

$$\hat{H}_i = -\frac{1}{2}\hbar\Omega(t)|b\rangle\langle a| + H.c., \tag{1.80}$$

where H.c. indicates the Hermitian conjugate of the previous term and $\Omega(t) = \frac{\mu E}{\hbar}e^{-i(\omega t - kz)}$ is the complex, time dependent Rabi frequency with ω and k the frequency and wave number of the light source, respectively, and μ is the dipole moment. We often only care about the amplitude of $\Omega(t)$, and write $\Omega = |\Omega(t)|$, removing the fast oscillation in t and z.

The pure state density matrix is $\rho = |\Psi\rangle\langle\Psi|$, determined by $|\Psi\rangle = a(t)e^{-i\omega_a t}|a\rangle + b(t)e^{-i\omega_b t}|b\rangle$. The determination of these coefficients is simply a matter of solving a first order ordinary differential equation. For convenience, we define the modified Rabi frequency $\Omega' = \sqrt{\Omega^2 + \Delta^2}$, where Δ is the detuning of the laser from

the atomic transition, $\Delta = \omega - (\omega_b - \omega_a)$. If the atom is initially in the ground state $[a(0) = 1, b(0) = 0]$, we find

$$|\Psi(t)\rangle = \left[\cos(\Omega't/2) - i\frac{\Delta}{\Omega'}\sin(\Omega't/2)\right] e^{-i(\omega_a - \Delta/2)t}|a\rangle + i\frac{\Omega}{\Omega'}\sin(\Omega't/2)e^{-i(\omega_b + \Delta/2)t}|b\rangle. \tag{1.81}$$

If we look at the population of the excited state, we see that

$$|\langle b|\Psi(t)\rangle|^2 = \left|\frac{\Omega}{\Omega'}\right|^2 \sin^2(\Omega't/2). \tag{1.82}$$

That is, the probability that the electron will be found in the excited state oscillates in time at half of the modified Rabi frequency Ω'. The amplitude of these Rabi oscillations depends on the detuning Δ. For $\Delta = 0$ ($\Omega' = \Omega$), the population completely inverts to the excited state at $t = \pi(1 + 2n)/\Omega$, for all integers n.

In the next section, we will discuss the application of a second single mode electric field, resulting in electromagnetically induced transparency (EIT).

1.3.2 Electromagnetically Induced Transparency

It is by now well known that the application of two coherent laser beams near atomic resonance gives rise to some interesting effects under the right conditions [EIT, electromagnetically induced absorption (EIA), guiding, four-wave mixing, etc.]. To understand these effects, let us consider a three level atom as shown in Fig. 1.4. The detuning of the probe field from resonance is given by Δ and the two-photon detuning of the probe and coupling fields is given by δ. The excited state decay rate is given by Γ (equal into both ground states) and the ground state decay rate is given by γ. We write the applied electric fields $E_{p,c}$ in terms of their Rabi frequencies,

$$\Omega_p(t) = \frac{\mu E_p}{\hbar}e^{-i(\omega_p t - kz)}, \tag{1.83}$$

$$\Omega_c(t) = \frac{\mu E_c}{\hbar}e^{-i(\omega_c t - kz)}. \tag{1.84}$$

$$\tag{1.85}$$
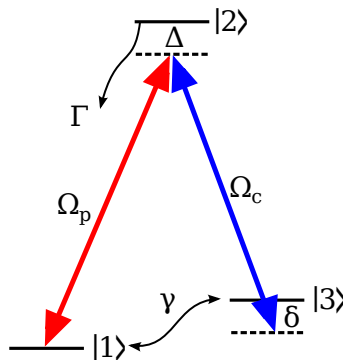
Figure 1.4: A standard three level atom in a Λ configuration with applied probe and coupling fields.

We concern ourselves with only one dimension (z).

The state of the atom is described by the density operator ρ, and the interaction Hamiltonian can be written as

$$\hat{H}_i \approx -\frac{1}{2}\hbar\Omega_p(t)|2\rangle\langle 1| - \frac{1}{2}\hbar\Omega_c(t)|2\rangle\langle 3| + H.c. \tag{1.86}$$

At this point, we have the option of solving the system for $\hat{\rho}(t)$, allowing us to calculate any quantities of interest. This problem, in general, is quite complex and typically involves a large number of assumptions.

For our purposes, we will assume that the coupling field is much stronger than the probe field and that the electron is initially in state $|1\rangle$, such that $\rho_{11} = 1$ and $\rho_{22} = \rho_{33} = 0$ at $t = 0$. We are typically interested in how the probe field interacts with the atom, and therefore the element of ρ which is most important is ρ_{21}, i.e., the element that connects the ground state $|1\rangle$ to the excited state $|2\rangle$. For this element, the steady-state perturbative solution to Eq. (1.79) is given by

$$\rho_{21} \approx \frac{\Omega_p}{2}\frac{\delta + i\gamma}{(\delta + i\gamma)(\Delta + i\Gamma/2) + |\Omega_c|^2/4}. \tag{1.87}$$

For a detailed derivation, see references [8, 40]. In the next section, we will see how the ρ_{21} term is related to the propagation of the probe field.

1.3.3 Dispersion and Slow Light

We have seen how the application of an oscillating electric field near the resonance of an atom can cause the electron to oscillate between the ground and excited states of that atom. However, we have not discussed how the atom affects the electric field. In particular, how is the probe field from the previous section altered as it passes through an EIT medium with a number density N?

A dipole moment is induced between two levels upon an application of the field near resonance, given by $P = e\langle\Psi|\hat{r}|\Psi\rangle$ in steady state. Since $\hat{r}$ is odd, we note that $\langle a|\hat{r}|a\rangle = \langle b|\hat{r}|b\rangle = 0$ and $\langle a|\hat{r}|b\rangle = \langle b|\hat{r}|a\rangle$. We then make the connection that the polarization of the atom is also related to the applied electric field, as given by $P = 2\mu\rho_{ab} = \epsilon_0\chi E$, where χ is the (rank zero) electric susceptibility tensor of the atom.

We can therefore solve for χ near the electronic transition $2 \rightarrow 1$, and find

$$\chi(\Delta) \approx \frac{N|\mu|^2}{\hbar\epsilon_0} \frac{\delta + i\gamma}{(\delta + i\gamma)(\Delta + i\Gamma/2) + |\Omega_c|^2/4}. \tag{1.88}$$

If we make the connection that $n = \sqrt{1 + \chi}$ is the index of refraction for the atom, we see in Fig. 1.5 how the real and imaginary parts of n are related as a function of the detuning Δ.

To interpret these curves, we must understand the significance of the real and imaginary parts of the index of refraction. In general, the index modifies the phase of the plane wave such that $\phi = \omega t + kz \rightarrow \omega t + nkz$. For a complex index $n = n' + in''$, we have $nkz = n'kz + in''kz$, so that the real part of n alters the phase ϕ of the field, and the imaginary part n'' is related to an exponential attenuation or gain, as seen by

$$E(z, t) = E_0 e^{i(\omega t + n'kz + in''kz)} = E_0 e^{-n''kz} e^{i(\omega t + n'kz)}. \tag{1.89}$$

Additionally, remembering that $k = 2\pi/\lambda$, we see that $\lambda \rightarrow \lambda/n'$. That is, for a medium with $n > 1$ (like glass), the wavelength of the radiation is compressed in-
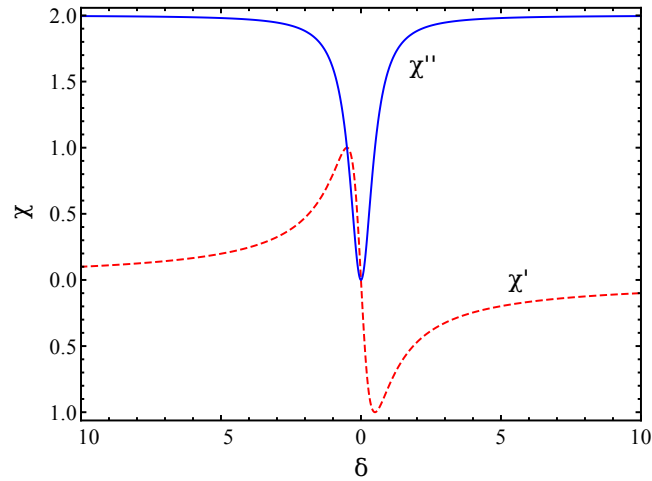
Figure 1.5: Dispersion and absorption curves for a three level atom in an EIT configuration with arbitrary parameters.

side the medium. Due to energy conservation, this implies that the phase velocity must decrease, such that $v_p = c/n'$.

If instead one considers a wave packet, such as a Gaussian pulse traveling through a medium with index n, the *group velocity* of this packet is given by

$$v_g(\omega) = \frac{d\omega}{dk} = c/n_g = \frac{c}{n'(\omega) + \omega\frac{dn'}{d\omega}}, \tag{1.90}$$

where n_g is called the group index. We see immediately that, in order to slow down a pulse of light, we require a large dispersion $dn'/d\omega$. A quick look at Fig. 1.5 shows that an EIT medium is a good candidate for both transparency (vanishing χ'') and dispersion (steep χ'). A great review of slow and fast light can be found in reference 41. Later, in chapter four, we will see how EIT can be used to guide light, and then how dispersion can lead to precision measurement optical frequency changes.

1.4 Outline of Thesis

The following pages are a subset of more than five years of Ph.D. research in the John Howell quantum optics lab at the University of Rochester. We will delve into only those experimental results that form the most cohesive representation of my research contributions, focusing on precision measurement using weak values. For clarity, I will quickly outline the remaining chapters.

Chapter two describes the way in which weak values can be used in an interferometer to amplify very small transverse deflections of an optical beam. The theory for this interferometric weak value amplification method is presented along with the experimental results; an angular deflection resolution of a mirror down to 560 femtoradians (fm) is obtained. This is followed by a detailed analysis of the signal-to-noise ratio (SNR). It is shown that this method has the advantage of reduced technical noise and allows for the use of detectors with a low saturation intensity.

In chapter three, we describe a weak value inspired phase amplification technique in a Sagnac interferometer. In contrast to homodyne, this measurement technique involves only one position sensitive detector. In fact, we monitor only the dark port and show that the signal varies linearly with phase, resulting in similar sensitivity to standard techniques.

In chapter four, we describe three related experiments, eventually resulting in an accurate measurement of optical frequency. We begin by demonstrating a weak value measurement of a change in optical frequency of 129 ± 7 kHz/$\sqrt{\text{Hz}}$ using a standard glass prism. We then show how the dispersion obtained in hot Rb vapor can be used to guide light and, ultimately, disperse multiple optical frequencies in a prism configuration. We resolve spectral lines 50 MHz apart and realize a spectral sensitivity of 20 Hz/$\sqrt{\text{Hz}}$ via precision deflection measurements.

In chapter five, a proposal for a weak measurement experiment with theo-

retical predictions is presented. The results demonstrate a non-local recovery of entanglement using weak measurements on a statistically amplitude damped pair of qubits. We discuss concurrence as well as fidelity in the context of a biphoton and present a possible optical implementation.

2 Deflection Measurements

2.1 Introduction

The ultimate limit of the sensitivity of a beam deflection measurement is of great interest in physics. The signal-to-noise ratio (SNR) of such measurements is limited by the power fluctuations of coherent light sources, as discussed in chapter one, providing a theoretical bound known as the shot noise limit. Similarly, there is a quantum limit on the precision with which one can measure the force on an object [42], derived from the Heisenberg uncertainty principle; this standard quantum limit (SQL) also plays a role in beam deflection measurements.

To reach this limit, there are a variety of techniques. It was found that interferometric measurements of longitudinal displacements and split-detection of transverse deflections have essentially the same ultimate sensitivity [43]. In the previous chapter, we discussed how using interference techniques can result in the amplification of a measurement result. In the present chapter, we will describe in detail the development of this weak value amplification technique in the optical regime, which combines interferometry with split detection, and report on experimental results.

This weak value measurement uses the which-path information of a Sagnac

interferometer to obtain dramatically enhanced resolution of the deflection of an optical beam. The resulting scheme reaches nearly the same ultimate sensitivity as previous methods, but with a number of advantages for precision measurement science. First, it can be used with a variety of beam deflection sources and is not limited to a polarization dependent deflection or displacement such as in references [14, 30]. Second, due to the post-selection, the reduced number of photons incident on the detector allows for the use a wide variety of detection schemes. Finally, the post-selection attenuation is completely independent of the source of deflection because it originates from the destructive interference between the two interferometer paths. In the experiment reported here, the weak measurement consists of monitoring the transverse position of the photon after exiting the interferometer, which gives partial information about which path the photon traversed.

2.2 Theory

In section 1.2.3, we showed how one might derive a weak value from a setup consisting of a photon in a Sagnac interferometer. Here, we will derive the result in a slightly different way and arrive at the same result, while providing more detail relevant to an experimental implementation.

Consider the schematic of the weak value amplification scheme shown in Fig. 2.1. A light beam enters a Sagnac interferometer composed of a 50:50 BS and mirrors to cause the beam to take one of two paths and eventually exit via the same 50:50 BS. For an ideal, perfectly aligned Sagnac interferometer, all of the light exits the input port of the interferometer which is therefore referred to as the bright port; the other port is known as the dark port. The constructive interference at the entrance port occurs due to two $\pi/2$ phase shifts which occur upon reflection at the BS. This symmetry is broken with the presence of a HWP and a SBC
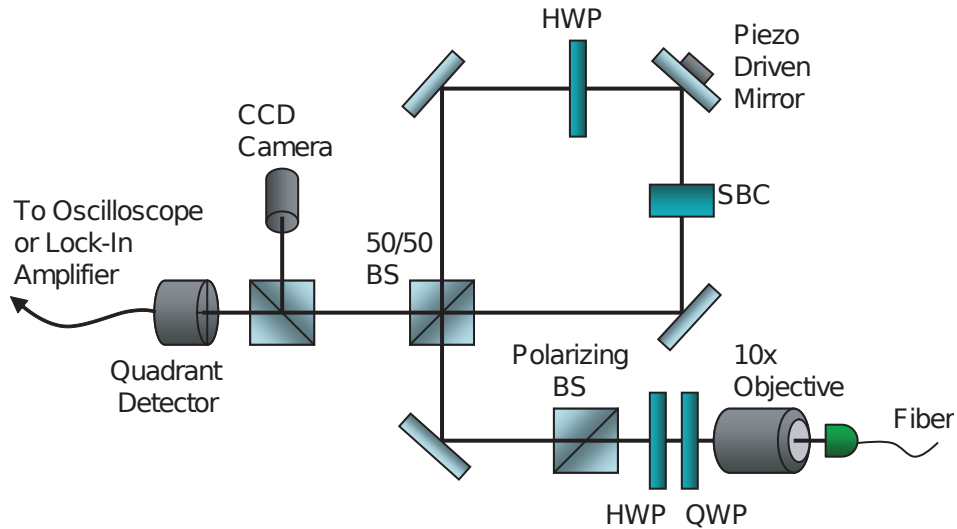
Figure 2.1: Experimental setup for the weak value deflection measurement. See text for details.

which introduce a relative phase ϕ between the paths, allowing one to continuously change the dark port to a bright port. While the theory presented here is for single photons, the experiment was realized with a coherent light source. As shown in the previous chapter, the results are the same.

The beam travels through the interferometer, and the spatial shift of the beam exiting the dark-port is monitored. We refer to the beam's which-path information as the *system*, described as before with the states $\{|\circlearrowright\rangle, |\circlearrowleft\rangle\}$. The transverse position degree of freedom of the beam, labeled by the states $|x\rangle$, is referred to as the *meter*. A slight tilt is given to the mirror at the symmetric point in the interferometer. This tilt corresponds to a shift of the transverse momentum of the beam. Importantly, the tilt also breaks the symmetry of the Sagnac interferometer, with one propagation direction being deflected to the left of the optical axis at the exit of the BS, and the other being deflected to the right. In other words, the which-path observable is coupled to the continuous transverse deflection.

This effect entangles the *system* with the *meter* via an impulsive interaction

Hamiltonian, leading to an evolution operator $\exp(-i\hat{x}\hat{A}k)$, where $\hat{x}$ is the transverse position operator for the meter, k is the transverse momentum shift given to the beam by the mirror, and the *system* operator $\hat{A} = |\circlearrowleft\rangle\langle\circlearrowleft| - |\circlearrowright\rangle\langle\circlearrowright|$ describes the fact that this momentum-shift is opposite for each propagation direction.

The splitting of the beam at the 50:50 BS, plus the SBC (causing the relative phase ϕ) results in an initial *system* state of $|\psi_i\rangle = (ie^{i\phi/2}|\circlearrowleft\rangle + e^{-i\phi/2}|\circlearrowright\rangle)/\sqrt{2}$. The entangling of the position degree of freedom with the which-path degree of freedom results in the state

$$|\Psi\rangle = \int dx\psi(x)|x\rangle \exp(-ix\hat{A}k)|\psi_i\rangle, \qquad (2.1)$$

where $\psi(x)$ is the wavefunction of the *meter* in the position basis. This evolution is part of a standard analysis on quantum measurement, where the above transformation would result in a momentum-space shift of the *meter*, $\Phi(p) \to \Phi(p\pm k)$, if the initial state is an eigenstate of $\hat{A}$, as described in chapter one.

The weak value analysis then consists of expanding $\exp(-ix\hat{A}k)$ to first order (assuming $k\sigma < 1$, where $\sigma = \sqrt{\langle x^2\rangle}$ is the initial size of the beam) and post-selecting with a final state $|\psi_f\rangle = (|\circlearrowright\rangle + i|\circlearrowleft\rangle)/\sqrt{2}$ (describing the dark-port of the interferometer). This leaves the state as

$$\langle\psi_f|\Psi\rangle = \int dx\psi(x)|x\rangle\langle\psi_f| \exp(-ix\hat{A}k)|\psi_i\rangle \qquad (2.2)$$

$$= \int dx\psi(x)|x\rangle[\langle\psi_f|\psi_i\rangle - ikx\langle\psi_f|\hat{A}|\psi_i\rangle]. \qquad (2.3)$$

We now assume that $k\sigma|\langle\psi_f|\hat{A}|\psi_i\rangle| < |\langle\psi_f|\psi_i\rangle| < 1$, and can therefore factor out the dominant state overlap term to find

$$\langle\psi_f|\Psi\rangle = \langle\psi_f|\psi_i\rangle \int dx\psi(x)|x\rangle \exp(-ixA_wk), \qquad (2.4)$$

where we have re-exponentiated to find an amplification of the momentum shift by the *weak value*

$$A_w = \frac{\langle\psi_f|\hat{A}|\psi_i\rangle}{\langle\psi_f|\psi_i\rangle} \qquad (2.5)$$
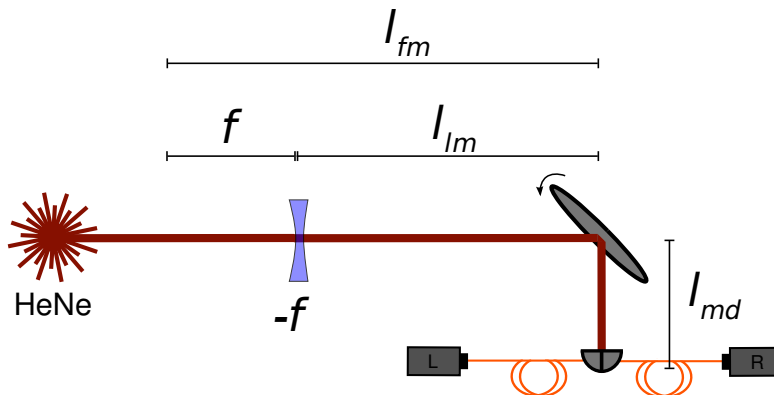
Figure 2.2: Weakly diverging beam in a deflection measurement.

with a post-selection probability of $P_{ps} = |\langle\psi_f|\psi_i\rangle|^2 = \sin^2(\phi/2)$. The new momentum shift kA_w will be smaller than the width of the momentum-space wavefunction, $1/\sigma$, but the weak value can greatly exceed the $[-1, 1]$ eigen-value range of $\hat{A}$. In the case at hand, the weak value is purely imaginary, $A_w = -i\cot(\phi/2) \approx -2i/\phi$ for small ϕ. This has the effect of causing a shift in the position expectation,

$$\langle x \rangle = d_w = 2k\sigma^2|A_w| \approx 4k\sigma^2/\phi, \tag{2.6}$$

assuming a symmetric spatial wavefunction. This gives the same result as Eq. (1.54).

To consider the case of a diverging beam we insert a negative focal length lens before the interferometer and use standard Fourier optics methods in the paraxial approximation outlined in Goodman [44]. In the quantum treatment, phase factors and Fourier transforms are applied to the quantum state $\Psi(x)$ or $\widetilde{\Psi}(k_x)$ instead of the electric field. See Fig. 2.2 for the relevant distances.

Passing through the lens, the wavefunction acquires a multiplicative phase factor $\exp[ik_0x^2/(2f)]$, where k_0 is the wavenumber of the light and f is the focal length of the lens (note that $f > 0$ and we have inserted the negative by hand, resulting in a spreading beam). Propagation effects are accounted for by

Fourier transforming the state at the lens, and applying a multiplicative phase factor $\exp[-ip^2 l_{lm}/(2k_0)]$ to the momentum-space wavefunction, where l_{lm} is the distance between the lens and the mirror. The effect of the oscillating mirror is to shift the state by a very small transverse momentum k, $\Phi(p) \to \Phi(p \pm k)$, where the direction of the shift depends on which path the photon takes in the interferometer. Propagation from the mirror to the detector results in a final multiplicative phase factor $\exp[-ip^2 l_{md}/(2k_0)]$ on the momentum-space wavefunction, where l_{md} is the distance between the mirror and the detector. After applying an inverse Fourier transform, the individual amplitudes in both arms are given by

$$\Psi_{\pm}(x) \propto \exp\left[\frac{-ik_0 x^2 \pm 2ilkx}{2(l + l_{md})}\right], \tag{2.7}$$

up to normalization, where $l = l_{lm} - \sigma^2 f/[\sigma^2 + if/(2k_0)]$ and σ is the beam radius at the lens. These amplitudes now interfere with a relative phase ϕ, and the position of the beam is monitored with a split detector at the dark port. Because the relative momentum shift k given by the movable mirror is so small, the post-selection probability is given only by the overlap of pre- and post-selected states, $P_{ps} = \sin^2(\phi/2) \approx \phi^2/4$ for $\phi \ll 1$. If we consider the beam far from the focus, such that the wavelength $\lambda \ll 2\pi\sigma^2/f$, we find that the beam deflection is given by

$$d'_w = \frac{4k\sigma^2}{\phi} \frac{l_{fm}(l_{fm} + l_{md})}{f^2} = d_w F, \tag{2.8}$$

where $F = l_{fm}(l_{fm} + l_{md})/f^2$ and l_{fm} is the distance between the focal plane of the lens and the mirror.

Finally, we can compare this result to the unamplified deflection (without the interferometer) of $\delta = k l_{md}/k_0$, where k_0 is the wavenumber of the light so that $\theta = k/k_0$ is the small angle the mirror imparts to the light beam. The amplification factor is simply $\mathcal{A} = \langle x \rangle / \delta$.

2.3   Experiment

A fiber coupled 780 nm laser beam is collimated using a $10\times$ microscope objective. Just after the objective, the beam has a Gaussian radius of $\sigma = 640\ \mu$m. The beam can be made to be converging or diverging by moving the fiber end relative to the microscope objective. After collimation, the beam passes through a PBS giving a pure horizontal polarization. Half- and quarter-wave plates are used to adjust the intensity of the beam passing through the polarizing BS. The beam then enters a Sagnac interferometer input port (the pre-selection process). Passing through the interferometer in the clockwise direction, the beam first passes through a HWP which rotates the polarization to vertical. The beam then passes through a SBC which adds a tunable phase to the beam (the SBC is set to add this phase to vertically polarized beams relative to those polarized horizontally). Passing counterclockwise, the beam first passes through the SBC which now has no relative effect, then through the HWP, changing the polarization to vertical. A piezo-electric actuator scans the tilt of one of the interferometer mirrors back and forth. A gimbal mount is used so that the center of the mirror is the fulcrum. The tilt of the mirror gives the two propagation directions opposite deflections. The small beam deflection is the weak interaction between the transverse beam deflection (*meter*) and the which path degree of freedom (*system*).

Post-selection is achieved simply by monitoring the light that exits the dark port of the interferometer. Tuning the SBC to add a small but nonzero relative phase allows a small amount of light out of the dark port. This light is split by a 50:50 BS and sent to a CCD camera (Newport model LBP-2-USB) which monitors the beam structure, and to a 10 mm by 10 mm quadrant detector (New Focus model 2921) which monitors the beam deflection as well as the total power. The active area of the quadrant detector is significantly larger than the beams used.

The interferometer is roughly square with sides of approximately 15 cm. The

distance from the microscope objective to the piezo-driven mirror is $l_{lm} = 48$ cm. The distance from the piezo driven mirror to the detectors is $l_{md} = 114$ cm (the same distance to both the CCD camera and the quadrant detector). The piezo driven mirror has a lever arm of 3.5 cm.

The piezo deflection was calibrated by removing the 50:50 BS from the interferometer and observing the centroid of the beam on the CCD camera. In this configuration the beam experiences no interference and ray optics describes the beam deflection. The piezo response was found to be 91 pm/mV, verified from 500 Hz down to D.C.

To characterize the system the interferometer was first aligned well, minimizing the light exiting the dark port. The relative phase given by the SBC was then tuned away from zero, allowing light to exit the interferometer. The piezo-driven mirror was given a 500 mV peak-to-peak amplitude, 100 Hz, sinusoidal driving voltage and the beam deflection was observed using the quadrant detector connected to an oscilloscope. This was done over a range of beam sizes σ' (Gaussian beam radius at the detector), for three values of SBC phase difference. For these measurements the beam power entering the interferometer was 3.2 mW and the power exiting was between 30 μW and 170 μW. These measurements, as well as corresponding theoretical prediction curves given by Eq. (2.8) are shown in Fig. 2.3. The measured data is, in general, well described by the theory. The unamplified deflection is $\delta = 2.95$ μm.

At the smallest SBC angle (7.2°) the small overlap between pre- and post-selected states allows only a small amount of light to exit the dark port. With this light at low intensities it begins to be of roughly equal intensity to stray light incident on the quadrant detector. This leads to less than ideal amplification, as shown in Fig. 2.3. The error bars take into account random error only, not systematic error such as this.

For fixed interferometer output intensity, the range of detectable deflections
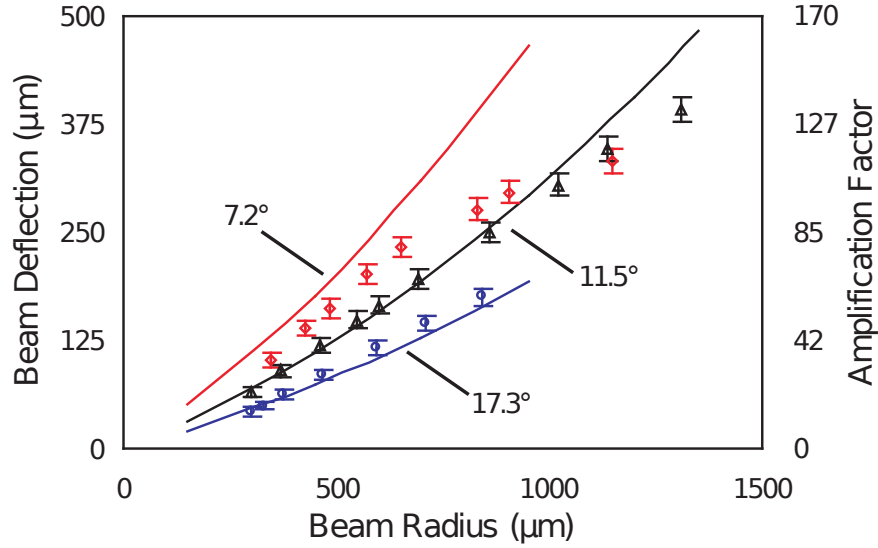
Figure 2.3: Measured beam deflection for different beam radii and different relative phases ϕ. The scale on the left is the measured beam deflection $\langle x \rangle$. The scale on the right is the amplification factor $\mathcal{A}$.

was also explored. The interferometer was again aligned such that the beams only had a small phase offset from each other. For these measurements the beam size at the detector was $\sigma = 1240 \pm 50$ μm. The weak value amplification factor was approximately 86, while the post-selection probability was about 2% (3.2 mW entered the interferometer while 63 μW exited the dark port). The amplification factor was found by driving the piezo with a 500 mV peak-to-peak signal and comparing the measured beam deflection with the aligned interferometer to the measured beam deflection with the interferometer BS removed. The piezo driving voltage was varied over five orders of magnitude while the output of the quadrant detector was sent to a lock-in amplifier and the signal was observed. The smallest driving voltage that yielded measurable a beam deflection was 220 nV, corresponding to an angular deflection of the mirror of 560 ± 40 frad (the mirror angle is half the beam deflection angle). These measurements are shown in Fig. 2.4. At smaller driving voltages, the lock-in amplifier was unable to lock
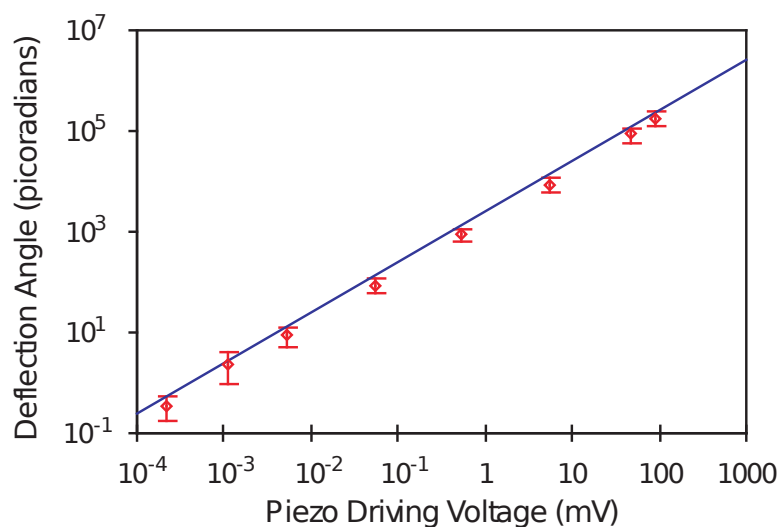
Figure 2.4: Measured deflection angle with weak value amplification. The solid line shows the expected deflection based on an interpolation of calibrated measurements of the piezo actuator's linear travel at higher voltages.

to the signal.

There are other, perhaps more interesting features of this experiment. The deflection indirectly measured the linear travel resolution of the piezo-electric actuator. The piezo actuator moved 20 ± 2 fm at the smallest measurable signal. This distance is on the order of large atomic nucleus diameters (Uranium is 15 fm) and is almost six orders of magnitude more resolution than the manufacturer's specifications of 10 nm. Also, as Hosten and Kwiat point out [30], weak value measurement techniques such as the one described here reduce technical noise (thermal, electrical, vibrational, etc.). This point will be explored later in this chapter.

2.4 Theory: Signal-to-Noise Ratio

Standard techniques to optimize the SNR of a beam deflection measurement include focusing the beam onto a split detector or focusing the beam onto the source of the deflection. The improvement of the SNR is of great interest in not only deflection and interferometric phase measurements but also in spectroscopy and metrology [45, 46], anemometry [47], positioning [48], micro-cantilever cooling [49], and atomic force microscopy [50, 51]. In particular, atomic force microscopes are capable of reaching atomic scale resolution using either a direct beam deflection measurement [50] or a fiber interferometric method [51]. We show that for any given beam radius, interferometric weak value amplification (WVA) can improve (or, at least match) the SNR of such beam deflection measurements. It has also been pointed out by Hosten and Kwiat that WVA reduces technical noise, which combined with our result provides a powerful technique [30].

The analogy between interferometry and beam deflection described in a paper by Barnett *et al.* [52] allows one to predict the SNR for a deflection of an arbitrary optical beam (e.g. coherent or squeezed). For a coherent beam with a horizontal Gaussian intensity profile at the detector of

$$I(x) = \frac{1}{\sqrt{2\pi}\sigma} e^{-x^2/2\sigma^2}, \tag{2.9}$$

they show that the SNR is given by

$$\mathcal{R} = \sqrt{\frac{2}{\pi}} \frac{\sqrt{N}d}{\sigma}, \tag{2.10}$$

where N is the total number of photons incident on the detector, d is the transverse deflection, and σ is the beam radius defined in Eq. (2.9). Equation (2.10) represents the ultimate limit of the SNR for position detection with a coherent Gaussian beam. Compare this to Eq. (1.74), where we assumed a square, flat top beam. We note that the two expressions have the same form aside from an overall constant related to the shape of the beam.

We now incorporate weak values by describing the amplification of a deflection at a split detector as a multiplicative factor $\mathcal{A}$. Thus, $d_w = \mathcal{A}d$ is the weak value amplified deflection. Also, the post-selection probability P_{ps} modifies the number of photons incident on the detector such that $N_w = P_{ps}N$. Note that the beam radius is not altered. We have seen that, for a collimated Gaussian beam passing through a Sagnac interferometer (see Fig. 2.5), the WVA factor and the post-selection probability are given by

$$\mathcal{A} = \frac{2k_0\sigma^2}{l_{md}}\cot(\phi/2), \ \ P_{ps} = \sin^2(\phi/2), \tag{2.11}$$

where l_{md} is the distance from the piezo-actuated mirror to the detector, k_0 is the wave number of the light and ϕ is the relative phase of the two paths in the interferometer.

Using Eqs. (2.11) and making the substitutions $d \to \mathcal{A}d$ and $N \to P_{ps}N$ into Eq. (2.10), we find the weak value amplified SNR is

$$\mathcal{R}_w = \alpha\,\mathcal{R}, \tag{2.12}$$

where $\alpha = 2k_0\sigma^2\cos(\phi/2)/l_{md}$. For a typical value of ϕ we note that $\cos(\phi/2) \approx 1$.

It is interesting to note that the dependence of the SNR is proportional to the beam radius at the detector in the amplified case [Eq. (2.12)] but inversely proportional when there is no amplification [Eq. (2.10)]. We see that it is possible to greatly improve the SNR in a deflection measurement with experimentally realizable parameters. Typical values for the experiment to follow are $\phi/2 = 25°$, $\sigma = 1.7$ mm, $l_{md} = 14$ cm and $k_0 = 8 \times 10^6$ m^{-1} such that the expected SNR amplification is $\alpha \approx 300$.

One might think that putting a detector in the far field would result in a very accurate deflection measurement. This is indeed correct; in fact, the far-field measurement can be obtained at the focal plane of a lens. This is recognized as a typical method to reach the ultimate precision for a beam deflection measurement

[43]. Consider a collimated Gaussian beam with a large beam radius σ which acquires a transverse momentum shift k given by a movable mirror. The beam then passes through a lens with focal length f followed by a split detector. The total distance from the source of the deflection to the detector is l_{md}, and the detector is at the focal plane of the lens. This results in a new deflection $d' = fk/k_0$ and a new beam radius $\sigma' = f/2k_0\sigma$ at the detector. Making the substitutions $d \to d'$ and $\sigma \to \sigma'$ into Eq. (2.10), we see that when the beam is focused onto a split detector the SNR is amplified:

$$\mathcal{R}_f = \alpha_f \, \mathcal{R}, \tag{2.13}$$

where $\alpha_f = 2k_0\sigma^2/l_{md}$ is the improvement in the SNR relative to the case with no lens [i.e. Eq. (2.10)]. Yet this is identical to the improvement obtained using interferometric weak values, up to a factor of $\cos(\phi/2) \approx 1$ for small ϕ. Thus we see that the improvement factors are equal using either WVA or a lens focusing the beam onto a split detector, resulting in the same ultimate limit of precision. However, WVA has three important advantages: the reduction in technical noise, the ability to use a large beam radius and having a lower intensity at the detector due to the post selection probability $P_{ps} = \sin^2(\phi/2)$.

Let us now consider the contribution of technical noise to the SNR of a beam deflection measurement. Suppose that there are N photons contributing to the measurement of a deflection of distance d. In addition to the Poisson shot noise η_i, there is technical noise $\xi(t)$ that we model as a white noise process with zero mean and correlation function $\langle \xi(t)\xi(0) \rangle = S_\xi^2 \delta(t)$. The measured signal $x = d + \eta_i + \xi(t)$ then has contributions from the signal, the shot noise, and the technical noise. The variance of the time-averaged signal $\bar{x}$ is given by $\Delta \bar{x}^2 = (1/N^2) \sum_{i,j=1}^N \langle \eta_i \eta_j \rangle + (1/t^2) \int_0^t dt' dt'' \langle \xi(t')\xi(t'') \rangle$, where the shot noise and technical noise are assumed to be uncorrelated with each other. For a coherent beam described in Eq. (2.9), the shot noise variance is $\langle \eta_i \eta_j \rangle = \sigma^2 \delta_{ij}$. Therefore, given a photon rate Γ (so
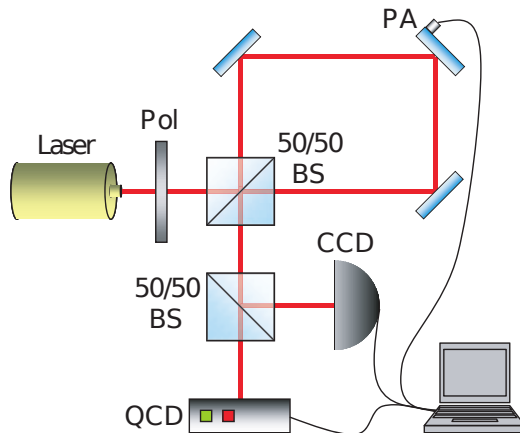
Figure 2.5: Experimental setup for testing the SNR of a deflection measurement. See text for details.

$N = \Gamma t$), the measured distance (after integrating for a time t) is given by

$$\langle x \rangle = d \pm \frac{\sigma}{\sqrt{\Gamma t}} \pm \frac{S_\xi}{\sqrt{t}}. \tag{2.14}$$

We now compare this with the weak value case. Given the same number of original photons N, we will only have $P_{ps}N$ post-selected photons, while the technical noise stays the same. Taking $d \to \mathcal{A}d$ this gives

$$\langle x \rangle = \frac{1}{\sqrt{P_{ps}}} \left(\alpha d \pm \frac{\sigma}{\sqrt{\Gamma t}} \pm \frac{S_\xi \sqrt{P_{ps}}}{\sqrt{t}} \right). \tag{2.15}$$

In other words, once we rescale, we have the same enhancement of the SNR by α as discussed in Eq. (2.12), but additionally the technical noise contribution is reduced by $\sqrt{P_{ps}}$ from using the weak value post-selection. Therein lies the power of weak value amplification for reducing the technical noise of a measurement.

2.5 Experiment: Signal-to-Noise Ratio

The experimental setup is shown in Fig. 2.5. A 780 nm fiber-coupled laser is launched and collimated using a 20× objective lens followed by a spherical lens

with $f = 500$ mm (not shown) to produce a collimated beam radius of $\sigma = 1.7$ mm. For smaller beam radii, the lens is removed and the $20\times$ objective is replaced with a $10\times$ objective. A polarizer is used to produce a pure horizontal linear polarization. The beam enters the interferometer (this is the pre-selection) and is divided, traveling clockwise and counterclockwise, before returning to the BS. A piezo-actuated mirror on a gimbal mount at a symmetric point in the interferometer is driven (horizontally) with a 10 kHz sine wave with a flat peak of duration 10 μs. The piezo actuator moves 127 pm/mV at this frequency with a lever arm of 3.5 cm. Due to a slight vertical misalignment of one of the interferometer mirrors, the output port does not experience total destructive interference (this is the post-selection on a nearly orthogonal state) and contains approximately 20% of the total input power, corresponding to $\phi/2 = 25°$. A second BS sends this light to a quadrant cell detector (QCD) and a charge coupled device (CCD) camera. The output from the CCD camera is monitored and the output from the QCD is fed into two low-noise preamplifiers with frequency filters (Stanford Research Systems model SR560) in series. The first preamplifier is ac coupled with the filter set to 6 dB/oct band-pass between 3 and 30 kHz with no amplification. The second preamplifier is dc coupled with the filter set to 12 dB/oct low-pass at 30 kHz and an amplification factor ranging from 100 to 2000. The low-pass filter limits the laser noise to the 10–90% risetime of a 30 kHz sine wave ($\tau = 10.5\mu$s) and so we take this limit as our integration time such that the number of photons incident on the detector during the measurement is $N = P\tau/E_\gamma$, where P is the power of the laser and E_γ is the energy of a single photon at $\lambda = 780$ nm.

In what follows, we compare measurements using two separate configurations: *WVA setup* is shown in Fig. 2.5 (diamonds, black curves) and produces the weak value amplification SNR found in Eq. (2.12); *SD setup* (for standard detection, circles, red curves) is the same as *WVA setup* but with the first 50:50 BS removed, resulting in the SNR given by Eq. (2.10). The curves are linear fits to the data
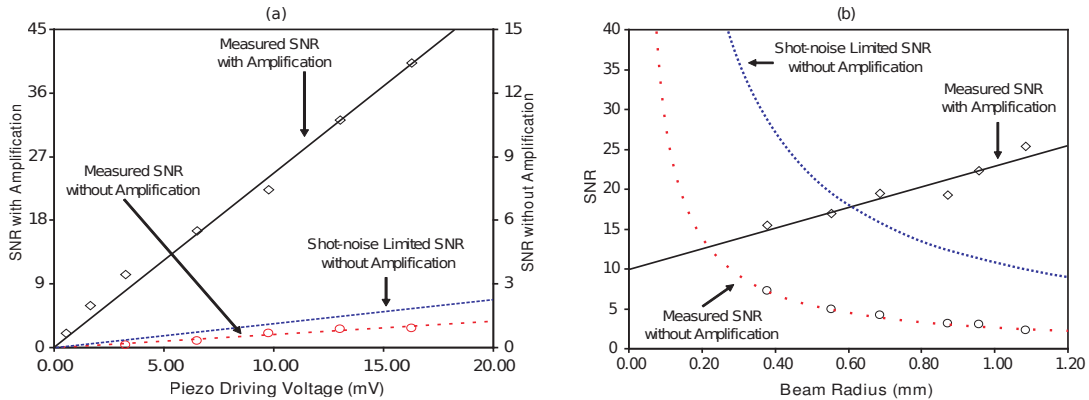
Figure 2.6: Data for the SNR of a deflection measurement. Note that for (a), the black curve is plotted using the left axis whereas the blue and red curves (dashed and dotted curves, respectively) are plotted using the right axis. See text for details.

with the y-intercept forced to zero. The error bars are smaller than the points. The theoretical curves of the SNR in Fig. 2.6 (blue curves), to which our data are compared, assume the configuration of *SD setup* with a noiseless detector which has a perfect quantum efficiency; this is what we refer to as an "ideal measurement." We see reasonable agreement of the data with theory by noting the trends in Fig. 2.5 as predicted by Eq. (2.12). The quoted error below comes from the measured data's standard deviation from the linear fits.

Data were taken for a fixed beam radius $\sigma = 1.7$ mm and detector distance $l_{md} = 14$ cm for two cases: (1) a variable piezo actuator driving voltage amplitude with a fixed input power of 1.32 mW [Fig. 2.5a]; and with (2) a variable input power with a fixed driving voltage amplitude of 12.8 mV (not graphed). For the first case, using *SD setup*, we measured a SNR a factor of 1.77 ± 0.07 worse than an ideal measurement; with WVA, i.e. *WVA setup*, an improvement of 39 ± 3 was obtained, corresponding to a SNR that is a factor of 21.8 ± 0.5 better than an

ideal measurement using *SD setup*. For the second case, we found that the SNR with WVA was linear in power, resulting in a SNR a factor of 22.5 ± 0.5 better than an ideal measurement using *SD setup*.

Next, the beam radius at the detector σ was varied from 0.38 to 1.1 mm while the beam radius at the lens was roughly constant at $a = 850$ μm. For this measurement, the input power was 1.32 mW, the distances were $l_{lm} = 0.51$ m and $l_{md} = 0.63$ m, and the driving voltage amplitude was 12.8 mV. The results are shown in Fig. 2.5b. Using *SD setup*, we find that the SNR varies inversely with beam radius as predicted by Eq. (2.10). However, using *WVA setup*, we see a linear increase in the SNR as the beam radius is increased as predicted by Eq. (2.12).

To verify the dependence of the SNR on l_{md}, as seen in Eqs. (2.10) and (2.12), we fixed the input power at 1.32 mW, the driving voltage amplitude at 12.8 mV, the beam radius at $\sigma = 1.7$ mm and varied the position of the detector relative to the piezo-actuated mirror. We found that, using *WVA setup*, the SNR was roughly constant with a value of 29 $\pm$1. This can be understood by realizing that, in Eq. (2.12), the l_{md} in the denominator cancels the l_{md} in the numerator owing to the fact that $d = l_{md}(\Delta\theta)$, where $\Delta\theta$ is the angular deflection. Using *SD setup*, we saw the expected linear relationship and we found that the system is worse than an ideal system by a factor of 3.2 ± 0.1.

To demonstrate the utility of this method we constructed a smaller interferometer with a smaller $l_{md} = 42$ mm and a smaller beam radius $\sigma = 850$ μm. For this geometry with 2.9 mW of input light and 390 μW of output light, the predicted amplification $\alpha = 260$. With these parameters, the SNR for an ideal *WVA setup* is approximately unity. We measured α to be 150. Combining this with our nonideal detector, we obtain an improvement of the SNR better than a quantum limited *SD setup* by a factor of 54. Practically, this means that in order to obtain equal measurement precision with this quantum limited system using

the same beam radius it would take over three more orders of magnitude of time or power.

An important note is that the expected WVA of the SNR for the larger interferometer is approximately $\alpha = 300$; yet only an $\alpha = 55$ (a factor of 5.5 below) was obtained from the graphed data. However, for the smaller interferometer, the measured α was only a factor 1.7 below the predicted value.

2.6 Conclusion

We have described and demonstrated a method of amplifying small beam deflections using weak values. The amplification is independent of the source of the deflection. In this experiment a small mirror deflection in a Sagnac interferometer provides the beam deflection. By tuning the interferometer and monitoring the resulting small amount of light exiting the interferometer dark port, weak value amplification factors of over 100 are achieved. The weak value experimental setup, in conjunction with a lock-in amplifier, allows the measurement of 560 frad of mirror deflection which is caused by 20 fm of piezo actuator travel.

While this technique does not beat the ultimate limit for a beam deflection measurement, it does have a number of improvements over other schemes: (1) the reduction in technical noise; (2) the ability to use high power lasers with low power detectors while maintaining the optimal SNR; and (3) the ability to obtain the ultimate limit in deflection measurement with a large beam radius. Additionally, we point out that, while weak values can be understood semi-classically, the SNR in a deflection measurement requires a quantum mechanical understanding of the laser and its fluctuations.

It is interesting to note that interferometry and split detection have been competing technologies in measuring a beam deflection [43]. Here we show that the combination of the two technologies leads to an improvement that can not be

observed using only one, i.e. that measurements of the position of a large radius laser beam with WVA allows for better precision than with a quantum limited system using split detection for the same beam radius.

Further improvements to the system may include decreasing stray light on the detector by carefully minimizing any back reflections from optics, and aligning the interferometer to have an improved dark port, possibly by using a deformable mirror, or using quantum limited detectors. As a note, this system may be used for active feedback stabilization since the sinusoidal deflection results in an in-phase sinusoidal amplified signal. Applications that can take advantage of this setup include: measuring the surface of an object by replacing the piezo actuator with a stylus such as with atomic force microscopy; measuring frequency changes using a dispersive material (see chapter four); or even measuring doppler shifts from fluid flow such as in Doppler anemometry.

3 Phase Measurements

3.1 Introduction

Phase measurements using coherent light sources find uses in myriad areas of science [53–57]. Therefore, it is not surprising that many advances in phase measurement techniques have been made since the introduction of the laser. For instance, Caves emphasized how the SNR of a phase measurement can be improved by using a squeezed vacuum state in the dark input port of an interferometer [58]. Related advances in this area include the use of other non-classical states of light such as Fock states [59] or the use of phase estimation techniques [60] which approach the Heisenberg limit in phase sensitivity [61]. Unfortunately, these states of light tend to be weak and very sensitive to losses, in effect reducing the SNR of a phase measurement. As a result, the use of coherent light sources has dominated the field of precision metrology [15, 62]. In this case, the phase sensitivity scales as $1/\sqrt{N}$ rad, where N is the average number of photons used in the measurement.

In this chapter, we show that it is possible to make a measurement of phase with the same SNR as balanced homodyne detection yet only the light in the dark port is measured. We use a coherent light source with a split-detector in a Sagnac interferometer and show that the signal of a phase measurement is amplified. We

derive our results using a classical wave description and a quantum mechanical treatment which uses a similar weak value formalism to that already presented. Much like with weak values [10, 12], there is a large reduction of the intensity at the detector due to interference at the beam splitter. Thus, we can use a low-cost detector with a low saturation intensity and still obtain significantly higher phase sensitivity when compared to using a balanced homodyne detector with the same total incident intensity. This method may improve the sensitivity of high-power balanced homodyne phase measurements.

3.2   Classical Theory

Consider a coherent light source with a Gaussian amplitude profile entering the input port of a Sagnac interferometer as shown in Fig. 3.1. The interferometer is purposely misaligned using a piezo-actuated mirror such that the two paths experience opposite deflections. The transverse momentum shift imparted by the mirror is labeled as k. A relative phase shift ϕ can be induced between the two light paths (clockwise and counterclockwise) in the interferometer.

We model the electric field propagation using standard matrix methods in the paraxial approximation. We can then write the input electric field amplitude as

$$\boldsymbol{E}_{in} = \left(\begin{array}{cc} E_0 e^{-x^2/4\sigma^2} & 0 \end{array} \right)^T, \tag{3.1}$$

where σ is defined as the Gaussian beam radius and T stands for transpose. The first position in the column vector denotes port 1 (see Fig. 3.1) of the beam splitter and the second position denotes port 2 (with no input electric field). We assume that the beam is large enough so that the entire interferometer fits within the Rayleigh range. The matrix representation for the 50:50 beamsplitter is given by

$$\boldsymbol{B} = \frac{1}{\sqrt{2}} \left(\begin{array}{cc} 1 & i \\ i & 1 \end{array} \right), \tag{3.2}$$
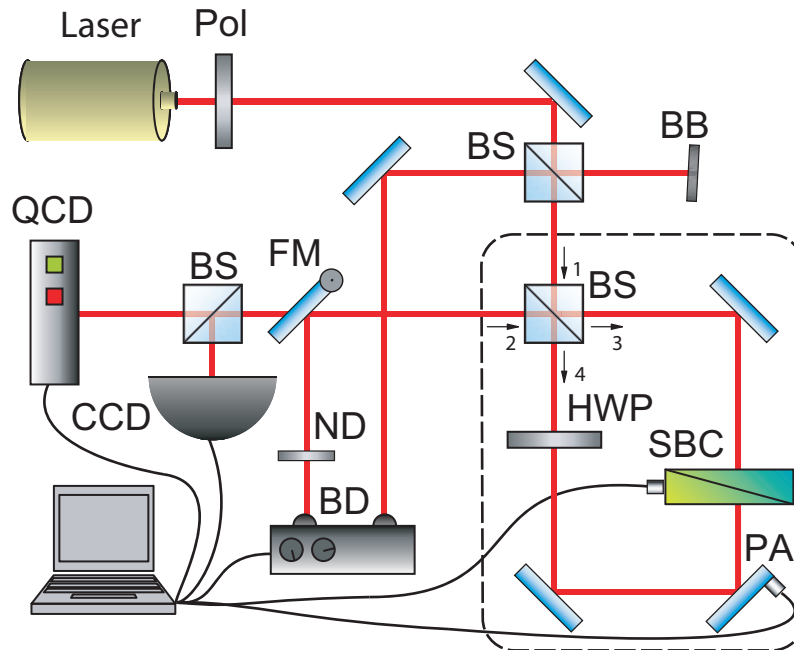
Figure 3.1: Experimental setup for measuring phase with weak values and ho-
modyne detection. See text for details. Beamsplitter (BS), beam block (BB),
polarizer (Pol), quad cell detector (QCD), half wave place (HWP), Soleil-Babinet
compensator (SBC), neutral density filter (ND), balance detector (BD), flip mirror
(FM) and the camera (CCD) are labeled accordingly.

where column and row one correspond to port 4 (counterclockwise) and column and row two correspond to port 3 (clockwise). We now define a matrix that gives both an opposite momentum shift k and a relative phase shift ϕ between the two light paths

$$\boldsymbol{M} = \begin{pmatrix} e^{i(-kx+\phi/2)} & 0 \\ 0 & e^{-i(-kx+\phi/2)} \end{pmatrix}. \tag{3.3}$$

The exiting electric field amplitude is represented by the matrix combination $(\boldsymbol{BMB})\boldsymbol{E}_{in}$,

$$\boldsymbol{E}_{out} = iE_0 e^{-x^2/4\sigma^2} \begin{pmatrix} -\sin(kx-\phi/2) \\ \cos(kx-\phi/2) \end{pmatrix}, \tag{3.4}$$

where the first position now corresponds to port 2 (the dark port) and the second position corresponds to port 1 (the bright port).

For a balanced homodyne detection scheme, we take $k=0$ and $\phi \to \pi/2 + \phi$ and subtract the integrated intensity of both ports. After normalizing by the total power, we obtain the unitless homodyne signal

$$\Delta_h = \sin(\phi). \tag{3.5}$$

Thus, we see that by balancing the interferometer, we are measuring the signal along the linear part of the sine curve for small phase shifts.

In contrast, if we consider a small transverse momentum shift ($k\sigma < 1$) and monitor only the dark port, given by the first element in the $\boldsymbol{E}_{out}$ vector, we find that

$$E_{out}^{(d)} \approx A \left(\frac{x}{\sigma} - \frac{\tan(\phi/2)}{k\sigma} \right) \exp[-x^2/4\sigma^2], \tag{3.6}$$

where $A = -iE_0 k\sigma \cos(\phi/2)$. The intensity at the dark port is then given by

$$I_d(x) = P_{ps}I_0 \left(\frac{x}{\sigma} - \frac{\tan(\phi/2)}{k\sigma} \right)^2 \exp[-x^2/2\sigma^2], \tag{3.7}$$

where P_{ps} is the attenuation (post-selection probability) of the measured output beam given by

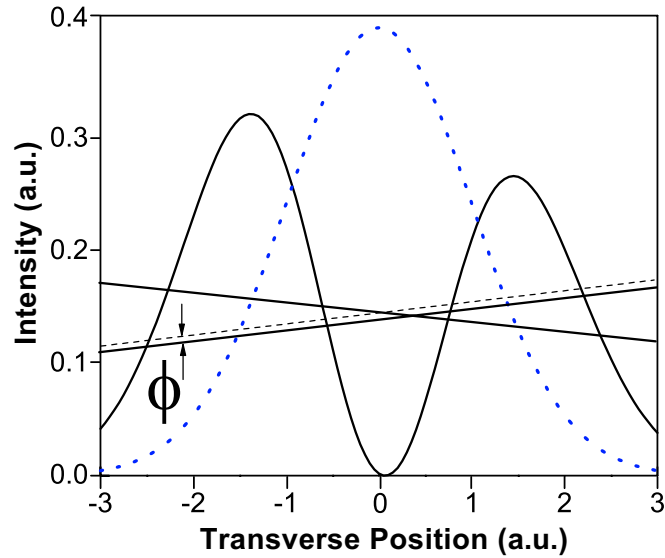$$P_{ps} = |k\sigma \cos(\phi/2)|^2, \tag{3.8}$$

Figure 3.2: Theory plot of the post-selected beam profile. See text for details.

and I_0 is the maximum input intensity. Aside from the attenuation factor P_{ps}, $I_d(x)$ is normalized to the input for vanishingly small ϕ.

Equation (3.7) is plotted in Fig. 3.2 for arbitrary values of the parameters. The dotted (blue) curve is the single-mode input profile of the beam in the interferometer. The solid (black) curve is the post-selected split-Gaussian mode produced by the misalignment of the interferometer and a slight relative phase shift between the two light paths. The solid lines represent the tilted wave fronts in the two paths of the interferometer when they combine at the BS, one that is delayed relative to the other, producing an asymmetric split-Gaussian (shown). The dashed line represents a wave front with the same tilt but zero relative phase delay, which would result in a symmetric split-Gaussian (not shown).

We see that, as the two tilted phase fronts are delayed relative to each other by ϕ, the average position of the beam shifts. Therefore, by measuring the average position of the beam, one can determine the relative phase shift between the beams traveling each path in the interferometer. This is the nature of the our measurement procedure.

3.3 Quantum Theory

We have presented the theory in terms of classical wave optics in order to provide the greatest accessibility. However, for an analysis at the single photon level, and an analysis of the signal-to-noise ratio for precision phase measurement, it is of interest to consider the quantum mechanical derivation.

As before, the experiment may be interpreted as the detection of the which-path (*system*) information of a single photon (clockwise or counter-clockwise). This is done indirectly using the transverse position degree of freedom of the photon as the *meter*, which is followed by a post-selection of the system state (due to the interference at the beam splitter), allowing only a few photons to arrive at the split-detector where the meter is measured.

If the pre- and post-selected system states are almost orthogonal (so $k\sigma \ll \phi \ll 1$), then there is an anomalously large shift of the beam's position by a factor of $\text{Im}[A_w] \approx -2/\phi$, referred to as the *weak value* of the system as described previously. The small overlap of the system's states gives rise to an amplification of the small momentum shift imparted by the mirror.

However, in the present case, $\phi \ll k\sigma \ll 1$, so the situation does not have a straightforward interpretation in terms of weak values. Nevertheless, there are certain features in common: the amplification effect can be traced back to the fact that there is a renormalization of the state, owing to a small post-selection probability P_{ps}.

Let us pick up the derivation from chapter two at Eq. (2.2), where we have the post-selected state $\langle \psi_f | \Psi \rangle$. Noting that the system operator has the property $\hat{A}^2 = \hat{1}$, we can expand the exponential in Eq. (2.2) to give $\exp(-ix\hat{A}k) = \cos(xk)\hat{1} - i\sin(xk)\hat{A}$. Thus, after post-selection, we find

$$\langle \psi_f | \Psi \rangle = \langle \psi_f | \hat{A} | \psi_i \rangle \int dx \, \left[A_w^{-1} \cos(xk) - i\sin(xk) \right] \psi(x)|x\rangle, \qquad (3.9)$$

where

$$A_w = \frac{\langle\psi_f|\hat{A}|\psi_i\rangle}{\langle\psi_f|\psi_i\rangle} = -i\cot(\phi/2) \approx -2i/\phi \qquad (3.10)$$

is defined as the *weak value* as before.

We assume that the mirror tilt is small compared to the beam radius, such that $k\sigma < 1$. We can thus expand the trigonometric functions in Eq. (3.9) to obtain

$$\langle\psi_f|\Psi\rangle \approx \langle\psi_f|\hat{A}|\psi_i\rangle k\sigma \int dx \left(\frac{-ix}{\sigma} + (k\sigma A_w)^{-1}\right)\psi(x)|x\rangle \qquad (3.11)$$

where we have factored out $k\sigma$ to preserve normalization. Using the approximation for A_w in Eq. (3.10), the intensity profile can be written as

$$I(x) \approx I_{ps}\left(\frac{x}{\sigma} - \frac{\phi}{2k\sigma}\right)^2 |\psi(x)|^2 \qquad (3.12)$$

where $I_{ps} = P_{ps}I_0$ is the post-selected intensity and $P_{ps} = |\langle\psi_f|\hat{A}|\psi_i\rangle k\sigma|^2 = k^2\sigma^2\cos^2(\phi/2)$ is the post-selection probability. This gives rise to a large attenuation of the number of photons striking the detector, $I_{ps} \ll I_0$, which will prove to be advantageous. It is also important to note that in contrast to the usual weak value amplification method, the post-selected intensity distribution is not a simple shift of the meter wavefunction. Instead, we obtain a two-lobe structure (see Fig. 3.2).

The average position displacement of the two-lobe intensity profile is given by

$$\langle x\rangle_w = -2\,\mathrm{Im}\left[A_w^{-1}\right] = \phi/k, \qquad (3.13)$$

where we note the amplification of a measurement of ϕ by the small number k. We see that the meter shift is now proportional to the *inverse weak value* A_w^{-1}.

Instead of measuring the average position, one can use a split detection method by integrating the intensity over the left side of the origin and subtracting from that the integrated intensity over the right side of the origin. This results in a split detection signal (in photon number) which, if normalized by the total power

striking the detector, is proportional to the average position. This quantity is given by

$$\Delta_w \approx \sqrt{\frac{2}{\pi}}\frac{\phi}{k\sigma} = \sqrt{\frac{2}{\pi\sigma^2}}\langle x \rangle. \tag{3.14}$$

Despite the large amplification of the average position measurement of the post-selected photons, the SNR is essentially the same for a balanced homodyne measurement of phase. The SNR of a phase measurement using balanced homodyne or split-detection can be expressed as $\mathcal{R}_{h,w} = \Delta_{h,w}\sqrt{N_d}$, where N_d is the number of photons striking the detector. These expressions are identical, except for an overall constant factor:

$$\mathcal{R}_h = \phi\sqrt{N}, \tag{3.15}$$
$$\mathcal{R}_w = \sqrt{\frac{2}{\pi}}\phi\sqrt{N}. \tag{3.16}$$

This factor reduces the SNR of the split-detection method by approximately 20%. It is also interesting to note that the SNR is independent of k. Thus, we can in principle reduce k (and P_{ps}) arbitrarily, allowing us to increase the input power and therefore N, ultimately improving the measurement sensitivity arbitrarily while using the same detector.

3.4 Experiment

In the present experiment (see Fig. 3.1), the coherent light beam was created using an external cavity diode laser tuned near the D_1 line of rubidium, approximately 795 nm. The beam was coupled into single mode fiber and then launched to produce a single mode Gaussian profile. The light was collimated with a radius of $\sigma \approx 775\,\mu$m and the continuous wave power ranged from 0.5 mW up to 1 mW. The Sagnac, composed of a 50:50 BS and three mirrors, was rectangular. We used two configurations for the geometry of the interferometer, one with dimensions 39 cm x 8 cm (large) and another with dimensions 11 cm x 8 cm (small). The beam

profile and position of the post-selected photons were measured using a QCD functioning as a split-detector and a CCD camera. During balanced homodyne detection, the signal was measured using a Nirvana balance detector (BD, New Focus model 2007). The quantum efficiency of the BD was about 81%, whereas the quantum efficiency of the QCD was 75%. The QCD was also equipped with a protective neutral density filter with 50% transmissivity. The outputs from the QCD and the BD were fed in series into two low-noise preamplifiers with frequency filters (Stanford Research Systems model SR560).

We used a half-wave plate (HWP) with a piezo-actuated SBC inside the Sagnac interferometer to induce a relative phase shift. The HWP was oriented such that the horizontally polarized input light was rotated to vertically polarized light. The SBC was oriented such that the fast axis was vertical and the slow axis was horizontal. The two light paths in the interferometer encountered these optical elements in opposite order, allowing for a known, tunable phase difference between them. The piezo-actuator in the SBC, which moved approximately 100 pm/mV, imparted a relative phase shift of $22 \pm 0.9 \, \mu$rad/V.

Using the large configuration, with 0.5 mW of input power, the piezo actuator in the SBC was driven with a 20 V peak to peak sine wave at 634 Hz, corresponding to a relative phase shift of 440 μrad. The normalized split-detection signal Δ_s (factoring in an offset from stray light hitting the detector) was measured while the transverse momentum shift k was varied using the piezo-actuated mirror. After scaling Δ_s by the appropriate factor given in Eq. (3.14), the results were plotted in Fig. 3.3. The theory line, which corresponds to a relative phase shift of 440 μrad, is drawn along with the data. We see good agreement of the data with theory, with a clear inverse dependence of $\langle x \rangle$ on k. However, it should be noted that a determination of k for this fit requires calibration, which in practice is quite simple.

We then compared this split-detection method of phase measurement to a bal-
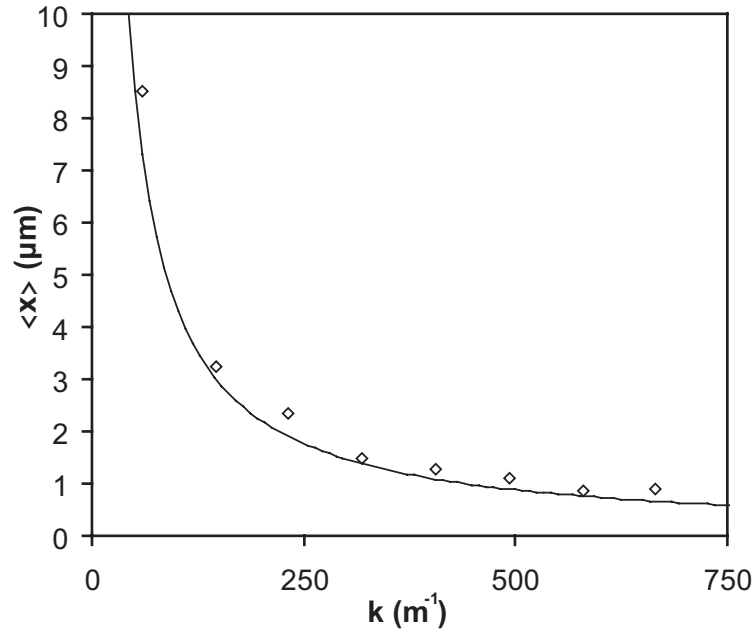
Figure 3.3: Deflection of the beam as a function of transverse momentum. See text for details.

anced homodyne measurement. We used the small configuration with 625 μW of (effective) continuous wave input power—taking into account various attenuators— and varied the driving voltage to the piezo-actuator in the SBC. The low-pass filter limits the laser noise to the 10% to 90% rise-time of a 1 kHz sine wave (300μs). We take this limit as our integration time to determine the number of 795 nm photons used in each measurement. We measured the SNR of a phase measurement using the same method as in chapter two and found that the SNR of our homodyne measurement was on average 3.2 times below an ideal shot noise limited system. The SNR of our split-detection method was on average 2.6 times below an ideal shot noise limited system. We take into account the quantum efficiency of each detector so that the number of photons used with each technique is the same for these two values, yet we ignore any contribution of dark current, thermal or mechanical noise to the expected SNR.

The results are plotted in Fig. 3.4. We vary the driving voltage applied to the
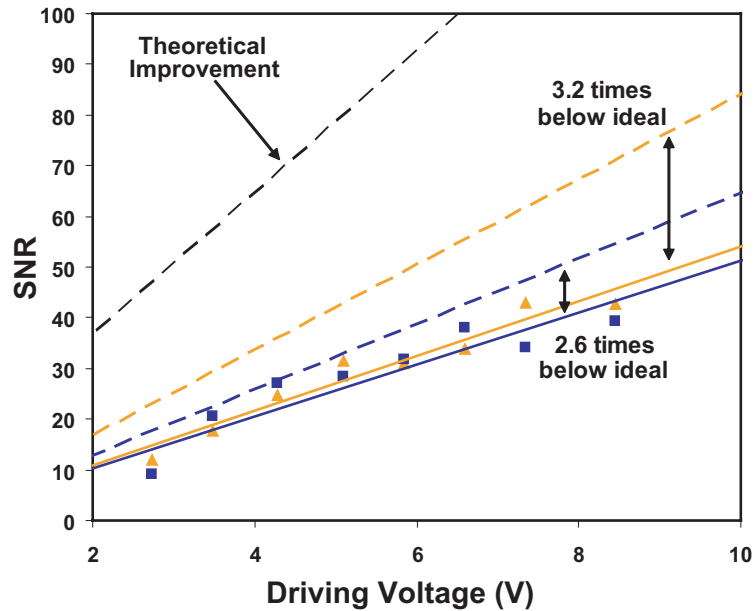
Figure 3.4: Data comparing weak values and the standard technique for phase measurement. See text for details.

piezo-actuator and measure the SNR using balanced homodyne detection (orange triangles) and the split-detection method (blue squares). The effective input power to the interferometer is approximately the same for both methods. Linear fits to the data (solid lines) show that these two methods have essentially the same sensitivity. The ideal shot noise limited SNR (factoring in the quantum efficiency of each detector) is plotted using a dashed blue line (split-detection) or a dashed orange line (balanced homodyne detection). The dashed black line illustrates the theoretical ($\sqrt{N}$) improvement of the split-detection method assuming that an equal number of photons are *incident* on both the split-detector and the balance detector.

Importantly, the SNR resulting from both measurement techniques is approximately the same. However, the split-detection method for this data had only about 15% of the input light incident on the detector. Thus, for diodes with the same saturation intensity, it is possible to use almost seven times more input

power with this configuration, resulting in a SNR about 2.6 times higher (the black, dashed line in Fig. 3.4). The improvement of the SNR by taking advantage of the attenuation before the detector has no theoretical limit and is only limited in practice by phase front distortions and back-reflections off of optical surfaces which degrade the fidelity of the interference. Using commercially available equipment and 24 hours of integration time, sub-picoradian sensitivity is possible even with a low-saturation intensity split-detector.

3.5 Conclusion

In summary, we have shown that the measurement of a relative phase shift between two paths in an interferometer can be measured and amplified using a split-detection method. We note that, although a Sagnac was used in this experiment, the same results apply to other interferometers (e.g. Michelson). Additionally, this method is comparable to the sensitivity achievable using balanced homodyne techniques, yet only the dark port of the interferometer is measured. The split-detector can have a low saturation intensity owing to the large attenuation. In fact, the higher the attenuation, the larger the amplification of the split-detection signal. Furthermore, we have shown that this technique exhibits an inverse weak value at the single photon level and, as discussed in references [16, 30], has the added benefit of reduced technical noise.

We believe that this technique is a robust, low-cost alternative to balanced homodyne phase detection and may have applications in a number of fields, e.g. magnetometry (using nonlinear magneto-optical rotation) or rotation sensing.

4   Frequency Measurements

The following chapter discusses the way in which one can measure the frequency information of a source of light; the chapter is divided into three sections. The first section discusses how weak values can be used in conjunction with a standard glass prism to measure the changes in the frequency of a laser. The second section is a diversion into atomic and optical physics where we locally modify the index of refraction of a material using a coherent optical process in a rubidium cell; the result is the optical guiding of a probe beam over a narrow bandwidth. We then return to frequency measurements, where our dispersing element is a prism filled with atomic rubidium. We conclude with a discussion of how these concepts can be joined for improved sensitivity.

4.1   Weak Value Frequency Measurement

4.1.1   Introduction

Precision frequency measurements [63–65] of a stabilized laser source are of great importance in the field of metrology [66] as well as atomic, molecular [67] and optical physics [68]. In this section, we show that weak values [10, 12, 35] in an optical deflection measurement experiment [15] can produce frequency shift

resolutions down to $129 \pm 7 \text{ kHz}/\sqrt{\text{Hz}}$ with only 2 mW of continuous wave optical power. By performing a weak measurement of the deflection of a near infrared laser source that has passed through a weakly dispersive prism, we are able to measure a change in optical frequency comparable to precision Fabry-Perot interferometers [69–71]. This technique is relatively simple, requiring only a few common optical components and operating at atmospheric pressure. Additionally, we show that this technique has low noise over a large range of response frequencies, making it desirable for many applications such as Doppler anemometry [72], tests of the isotropy of light propagation [68] or laser locking without the use of high finesse Fabry-Perot interferometers [73] or atomic lines.

First developed as a way to understand pre-selected and post-selected quantum measurements and how they relate to time-reversal symmetry in quantum mechanics, the weak value is a result of a so-called weak measurement; *i.e.,* a measurement which gains only partial information about the state of a system. It is therefore interesting that, with such a technique, precision measurement is possible [15, 16, 18, 30]. Indeed, there is a vast array of results, both theoretical [22, 35, 37, 74] and experimental [13, 38], which have gone a long way to further our understanding of the weak measurement process. We take advantage of this technique in order to measure the deflection of a laser beam, a deflection which can be traced back to the frequency of the laser source.

4.1.2 Theory

We describe here the frequency amplification experiment shown in Fig. 4.1 by further developing the ideas of chapter two and reference 15. Although the actual experiment uses a classical beam, we choose to characterize the weak value effect one photon at a time; this is valid, owing to the fact that we consider here a linear system with a coherent laser beam modeled as a linear superposition of Fock states [37].
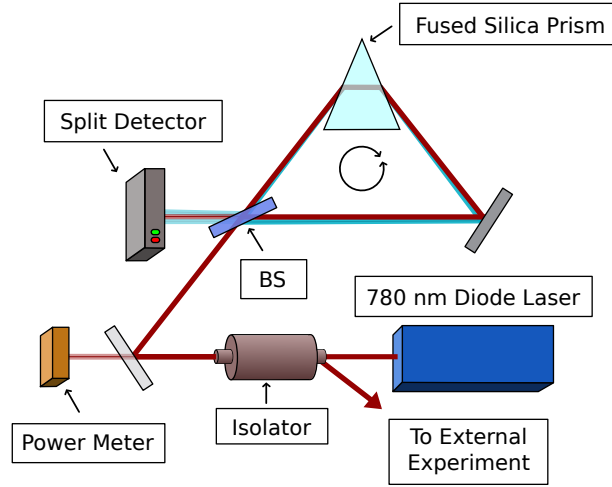
Figure 4.1: Experimental design for measuring frequency using weak values; BS is a 50:50 beam splitter.

In this experiment, a single-mode Gaussian beam of frequency ω and radius σ passes through an optical isolator, resulting in linearly polarized light. We assume that the radius is large enough to ignore divergence due to propagation. Light then enters a Sagnac interferometer containing a 50:50 beam splitter (BS), a mirror and a prism. The beam travels clockwise and counter-clockwise through the interferometer, denoted by the system states given by $\{|\circlearrowright\rangle, |\circlearrowleft\rangle\}$; we write the photon meter states in the position basis as $\{|x\rangle\}$, where x denotes the transverse, *horizontal* direction.

Initially, the interferometer (including the prism) is aligned such that the split photon wave function spatially overlaps (*i.e.,* the photons travel the same path whether by $|\circlearrowright\rangle$ or $|\circlearrowleft\rangle$). After the interferometer is aligned, the photons traversing each path receive a small, constant momentum kick in the *vertical* direction; this vertical kick is controlled by the interferometer mirror and results in a misalignment. Due to its spatial asymmetry about the input BS, this momentum kick creates an overall phase difference ϕ between the two paths. By adjusting the interferometer mirror, we can control the amount of light that exits the inter-

ferometer into the dark port. While the amplified signal ultimately depends on the value of ϕ, and therefore on the magnitude of the misalignment, the *signal to noise ratio* (SNR) is unaffected (discussed previously and below).

We then let $k(\omega)$ represent the small momentum kick given by the prism to the beam (after alignment) in the horizontal x-direction. We have explicitly inserted the frequency dependence of the moment kick to remind the reader that the source of the shift is a prism, and that the dispersion $dk/d\omega$ is material dependent. The *system* and *meter* are entangled via an impulsive interaction Hamiltonian [15] (resulting in a new state $|\psi_i\rangle \to |\Psi\rangle$) such that a measurement of the horizontal position of the photon after it exits the interferometer gives us some information about which path the photon took.

We consider a horizontal deflection that is significantly smaller than the spread of the wave packet we are trying to measure, *i.e.*, $k(\omega)\sigma \ll 1$. In this approximation, we find that the postselected state of the photons exiting the dark port is given by

$$\langle \psi_f | \Psi \rangle = \langle \psi_f | \psi_i \rangle \int dx \psi(x)|x\rangle \exp[-ixA_w k(\omega)], \qquad (4.1)$$

where the weak value is given by $A_w = -i \cot(\phi/2) \approx -2i/\phi$ for small ϕ.

There are two interesting features of Eq. (4.1). First, the probability of detecting a photon has been reduced to $P_{ps} = |\langle \psi_f | \psi_i \rangle|^2 = \sin^2(\phi/2)$, and yet the SNR of an ensemble of measurements is nearly quantum limited [16] despite not measuring the vast majority of the light. Second, the weak value (which can be arbitrarily large in theory) appears to amplify the momentum kick $k(\omega)$ given by the prism; the resulting average position is given by $\langle x \rangle_W = 2k(\omega)\sigma^2|A_w| \approx 4k(\omega)\sigma^2/\phi$, where the angular brackets denote an expectation value. We can compare this to the standard deflection caused by a prism measured at a distance l which is given by $\langle x \rangle \approx lk(\omega)/k_0$, where k_0 is the wavenumber of the light.

In order to predict the deflections $\langle x \rangle$ or $\langle x \rangle_W$, we must know the form of $k(\omega)$. For a prism oriented such that it imparts the minimum deviation on a beam, the
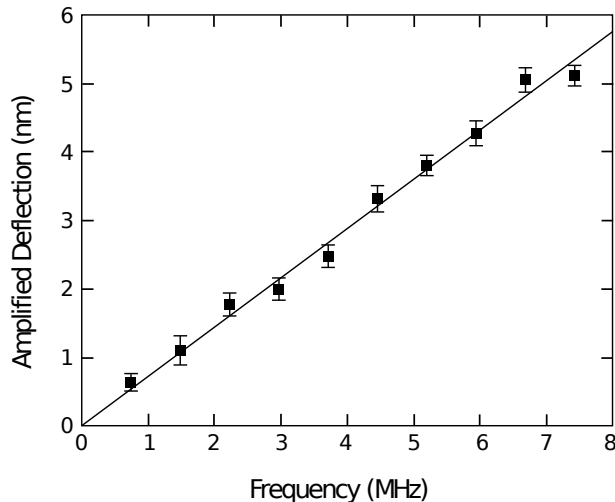
Figure 4.2: The position of the postselected beam profile is measured as we modulate the input laser frequency of the interferometer.

total angular deviation is given by $\theta(\omega) = 2\sin^{-1}[n(\omega)\sin(\gamma/2)] - \gamma$, where $n(\omega)$ is the index of refraction of the material and γ is the angle at the apex of the prism [75]. However, we are only interested in the small, frequency-dependent angular deflection $\delta(\omega) = \Delta\theta = 2\,\Delta n\{[\sin(\gamma/2)]^{-2} - [n(\omega)]^2\}^{-1/2}$, where Δn $(\Delta\theta)$ is the index change in the prism (angular deflection of the beam) for a given frequency change of the laser. The small *momentum kick* is expressed as $k(\omega) = \delta(\omega)k_0$. We can then write the amplified deflection as

$$\langle x \rangle_W \approx \frac{8k_0\sigma^2(\Delta n/\phi)}{\sqrt{[\sin(\gamma/2)]^{-2} - [n(\omega)]^2}}. \tag{4.2}$$

The frequency-dependent index $n(\omega)$ of fused silica, which was used in this experiment, can be modeled using the Sellmeier equation [76]. We can therefore calculate the expected $\langle x \rangle_W$ using Eq. (4.2). However, to compute the ultimate sensitivity of this weak value frequency measurement, we must include possible noise sources. If we consider only shot-noise from the laser, the SNR for small ϕ

is approximated by

$$\mathcal{R} \approx \sqrt{\frac{8N}{\pi}} k_0 \sigma \delta(\omega), \tag{4.3}$$

as shown in reference 16, where N is the number of photons used in the interferometer. Note that N is not the number of photons striking the detector, which is given by NP_{ps}. By setting $\mathcal{R} = 1$ and using modest values for N, σ and ω, we find that frequency sensitivities well below 1 kHz are possible. However, other sources of noise, such as detector dark current, radiation pressure and environmental perturbations will reduce the sensitivity of the device.

4.1.3   Experiment

In our experimental setup (shown in Fig. 4.1), we used a fiber-coupled 780 nm external cavity diode laser with a beam radius of $\sigma = 388\,\mu$m. The frequency of the laser was modulated with a 10 Hz sine wave using piezo controlled grating feedback. The frequency control was calibrated using saturation absorption spectroscopy of the hyperfine excited states of the rubidium D2 line[77]: $F = 3 \rightarrow F' = \{2 - 4$ crossover, $3 - 4$ crossover, $4\}$ transitions of rubidium 85 and the $F = 2 \rightarrow F' = \{1 - 3$ crossover, $2 - 3$ crossover, $3\}$ transitions of rubidium 87. Linearly polarized light was divided before the interferometer using a 50:50 BS (although an imbalanced ratio here would be ideal for practical applications). The light in one port was measured with a photodiode and used to lock the power at 2 mW with an acousto-optic modulator before the fiber. The interferometer was approximately $l = 27$ cm in length; the mirror used to adjust ϕ was approximately 6 cm from the input BS (measured counter clockwise) and the prism, made of fused silica, was approximately 5 cm from the input BS (measured clockwise). Although the prism was not symmetrically placed in the interferometer as described in the theory above, the results are the same aside from a global offset in position which can be subtracted off during processing. The interferometer was first aligned to

minimize light in the dark port and then, using the aforementioned mirror, mis-aligned to allow a small percentage of the light ($\sim$2-5%) into the dark port. The position of this light was measured using a split detector (New Focus model 2921). The signal was passed through two 6 dB/octave bandpass filters centered at 10 Hz and amplified by a factor of about 10^4.

A Gaussian laser beam passes through a Sagnac interferometer consisting of a 50:50 beam splitter (BS), a mirror and a prism. The prism weakly perturbs the direction of the beam as the frequency of the laser source is modulated, denoted by the dark and light gray beam paths. We monitor the position of the light entering the dark port of the interferometer. We lock the input power to the interferometer using a power measurement before the BS. The majority of the light exits the interferometer via the bright port and is collected with an isolator for use in an experiment.

For Fig. 4.2, we measured the peak of the deflection in each 100 ms cycle, repeated 25 times; we computed the average and the standard deviation of this set as we varied the change in the optical frequency. We find that the amplified deflection is a linear function of oscillating optical frequency given by about 720 $\pm$ 11 pm/MHz. Compared to the unamplified deflection of about 9.1 pm/MHz given by the expression for $\langle x \rangle$, this gives an amplification factor of 79 $\pm$ 1.2 and a computed P_{ps} of 1.3%; this agrees with the measured P_{ps} of 2-5% if we include the extra light present in the signal due to phase-front distortions from imperfect optics. The error bars are given by the standard deviation of the mean. The minimum frequency change measured here is around 743 kHz with an effective integration time of 30 ms.

A characteristic noise scan was taken and plotted in Fig. 4.3 with and without frequency modulation. The signal was passed directly from the split detector into the oscilloscope before performing a fast Fourier transform. Data was taken with and without a 7.4 MHz optical frequency modulation to show the noise floor over
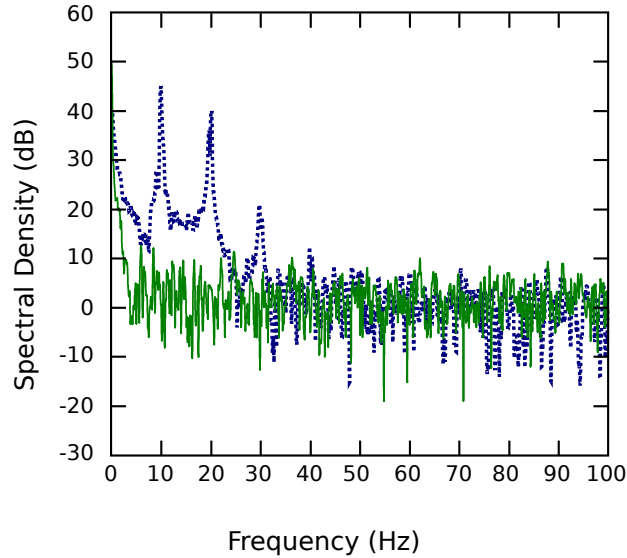
Figure 4.3: We show the noise spectrum for a passive system (green, solid trace) and for a driven system (blue, dashed trace), where the laser frequency modulation is 7.4 MHz at 10 Hz.

a large bandwidth. We see that the first harmonic of the signal is about 5 dB down from the fundamental and the third harmonic is nearly 25 dB down. For a 7.4 MHz change in laser frequency, we see that the noise is approximately 35 dB below the signal, demonstrating the low-noise nature of this measurement. The noise at higher frequencies was similarly flat.

Second, to test the range over which this device could function, we optimized the interferometer at the low-frequency end of the laser's tuning range and obtained a SNR of approximately 19 with the 7.4 MHz optical frequency modulation. We then tuned to the high-frequency end of the laser's tuning range ($\Delta f \approx 141$ GHz), without adjusting or recalibrating the interferometer, and obtained a SNR of 10. In fact, this range can be much larger so long as the weak value condition $k(\omega)\sigma \ll 1$ is satisfied; for our beam radius and optical frequency, we could in principle measure over a range of 5 THz, or about 10 nm.

For our experimental parameters, we can measure below 1 MHz of frequency change with a SNR around 1, as shown in Fig. 4.2. It should be noted that, although the time between measurements is a full 100 ms, our filtering limits the laser noise to time scales of about 30 ms. For analysis, we take this as our integration time in estimating N for each measurement. The resulting sensitivity for our apparatus is 129 ± 7 kHz$/\sqrt{\text{Hz}}$; *e.g.,* if we had integrated for 1 s instead of 30 ms, this device could measure a 129 kHz shift in frequency with a SNR of 1. The error in frequency comes from the calibration described above. Using Eq. (4.3), we find that the ideal ultimate sensitivity is approximately 67 kHz$/\sqrt{\text{Hz}}$. This implies that this apparatus, operating at atmospheric pressure with modest frequency filtering, is less than a factor of two away from the shot-noise limit in sensitivity. This is no longer surprising since we now understand the fact that weak value experiments amplify the signal, but not the technical noise [16, 30].

4.1.4   Summary

With only 2 mW of continuous wave input power, we have measured a frequency shift of 129 ± 7 kHz$/\sqrt{\text{Hz}}$; we have shown that the system is stable over our maximum tuning range of 140 GHz without recalibration and is nearly shot-noise-limited. With more optical power, longer integration and a more dispersive element such as a grating or a prism with $\sin(\gamma/2)n(\omega) \approx 1$, the sensitivity of this device can measure frequency shifts lower than 1 kHz, although a higher sensitivity comes at the cost of maximum tuning range. Compare this to commercially available Fabry-Perot interferometers, which report typical resolutions down to 5 MHz and free spectral ranges of only 1-5 GHz. More sensitive Fabry-Perot interferometers exist, yet they require a host of custom equipment to reduce environment noise, including vacuum systems and vibration damping. Moreover, an important advantage of this technique is that a large percentage ($\sim$90%) of the light used in the interferometer can then be sent off to another experiment (as

indicated in Fig. 4.1), allowing for real-time frequency information during data collection. While this device cannot compare to the absolute frequency sensitivity of frequency combs [65], we believe that this method is a simple solution for high-resolution, relative frequency metrology and will serve as a valuable laser-locking tool.

4.2   All Optical Wave Guiding

4.2.1   Introduction

As discussed in the previous section, we can alter the direction of a beam by modifying the index of refraction of the material in which it propagates. In the case of a prism, the index changes abruptly at the air-glass interface, and is otherwise uniform throughout each medium. However, we need not limit ourselves to a uniform index profile.

We know that, in the case of EIT, we can strongly modify the index of refraction of a probe beam near an atomic resonance in the presence of a strong coupling beam (see chapter one). In fact, off-resonant Raman absorption, which can be seen from Eq. (1.88), offers similar behavior, known as EIA. We can use either of these effects to produce an all optical wave guide, where the index is modified across the transverse direction of the probe beam due to a variation in the coupling power.

In this section, we show that the probe beam propagates with a small spot size over several diffraction lengths. This all optical waveguide is imprinted by a low power Laguerre Gaussian (LG) coupling laser beam. The refractive index at the annulus of the ring control beam is lower than that at the core for probe frequencies tuned to the blue of Raman resonance. We also show that the coupling efficiency of the probe beam into the waveguide varies linearly with the probe power.

4.2.2 Theory

Let us first review some of the properties of a Gaussian beam propagating in a medium where the refractive index decreases quadratically with the radial coordinate as we move away from the optical axis. The electric field distribution of a Gaussian mode propagating in the z direction is given by

$$E(r, z) = E_0 \frac{w_0}{w(z)} \exp[-i(kz + \phi(z)) - ikr^2/2q], \tag{4.4}$$

where $\phi(z)$ is the phase shift due to the geometry of the beam, k is the wave number of the light, $w(z)$ is the radius of the beam at a location z, w_0 is the beam radius at the beam waist, and q is the complex parameter describing the Gaussian beam. q is defined as

$$\frac{1}{q} = \frac{1}{R} - i\frac{\lambda}{\pi w(z)^2}, \tag{4.5}$$

where R is the radius of curvature of the phase front. As the beam propagates in free space from the beam waist, the spot size and the radius of curvature vary according to the following equations:

$$w^2(z) = w_0^2 \left[1 + \left(\frac{\lambda z}{\pi w_0^2}\right)^2\right], \tag{4.6}$$

$$R = z \left[1 + \left(\frac{\pi w_0^2}{\lambda z}\right)^2\right]. \tag{4.7}$$

We have a much simpler transformation relation for the beam parameter q and it is given by,

$$q_2 = q_1 + z, \tag{4.8}$$

where q_1 and q_2 are the beam parameters at two spatial locations separated by the distance z along the propagation direction. The transformation relation when the beam passes a converging thin lens of focal length f is given by,

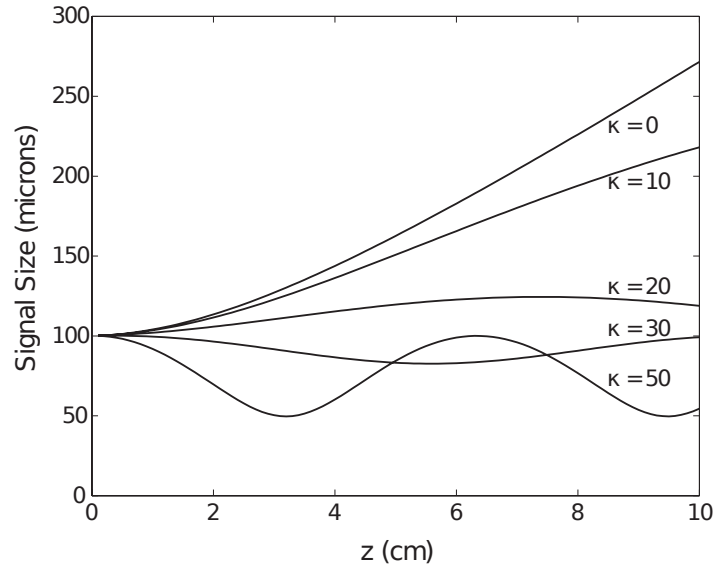$$\frac{1}{q_2} = \frac{1}{q_1} - \frac{1}{f} \tag{4.9}$$

Figure 4.4: Beam propagation as a function of κ.

It is known that in a medium where the refractive index varies quadratically with the transverse position, the transformation for the beam parameter can be written in terms of an ABCD matrix as

$$q_2 = \frac{Aq_1 + B}{Cq_1 + D}.$$ (4.10)

It has been shown by Yariv and Yeh [78] that for the lossless quadratic index medium, whose refractive index is given by $n = n_0[1 - (\kappa^2/2)r^2]$, the transformation relation is given by

$$q(z) = \frac{\cos(\kappa z)q_0 + \sin(\kappa z)/\kappa}{-\sin(\kappa z)\kappa q_0 + \cos(\kappa z)}.$$ (4.11)

Fig. 4.4 shows the change in probe beam size during propagation for various values of κ. We show the change for a propagation distance of 10 cm. The initial width of the beam is assumed to be 100 μm. $\kappa = 0$ corresponds to the case of the free space propagation, and higher values of κ indicate a medium with a sharper index contrast. We can see that the beam expands to more than 2.5 times its initial size

in free space, yet has a reduced divergence for larger values of κ. For very large values of κ, the probe size exhibits oscillatory behavior over a short distance.

We see that a medium with a quadratic transverse index profile can confine the mode of a probe beam; the medium is therefore called a waveguide. If we can control the properties of κ, we therefore have control over the properties of the waveguide. We shall see that this task is straightforward in the context of EIT and EIA, where κ is controlled all optically by the power, size and frequency of the control beam.

Consider the coupling beam in the Laguerre-Gaussian LG_{01} mode (ring mode) whose intensity can be written as,

$$I_c(r) = \frac{2P}{\pi w_c^2} \frac{r^2}{w_c^2} \exp\left(-\frac{2r^2}{w_c^2}\right), \tag{4.12}$$

where P is the coupling beam power and w_c is its width. When $r \ll w_c$, we can approximate the above expression as

$$I_c(r) = \frac{2P}{\pi} \frac{r^2}{w_c^4}, \tag{4.13}$$

i.e., we have a quadratic intensity profile. We therefore have

$$|\Omega_c|^2 = \frac{4\mu^2}{c\hbar^2\epsilon_0} \frac{P}{\pi w_c^4} r^2. \tag{4.14}$$

The real part of the off-resonant refractive index can be written as,

$$n = 1 + \frac{\beta}{2} \frac{|\Omega_c|^2}{4\Delta^2} \frac{\delta}{\delta^2 + \gamma^2} = 1 + \frac{\beta}{2} \frac{\mu^2}{c\hbar^2\epsilon_0} \frac{P}{\pi w_c^4} \frac{\delta}{\Delta^2(\delta^2 + \gamma^2)} r^2 \tag{4.15}$$

Note that we ignored power broadening and the AC stark effect in the above equation because the region of interest is the center of the ring beam where the coupling beam intensity is very small. We can see from the above equation that we have a medium with a refractive index that changes quadratically with the radial coordinate.

From Eqn. 4.15, we can write κ^2 as,

$$\kappa^2 = -\beta \frac{\mu^2}{c\hbar^2\epsilon_0} \frac{P}{\pi w_c^4} \frac{\delta}{\Delta^2(\delta^2 + \gamma^2)} r^2 \tag{4.16}$$
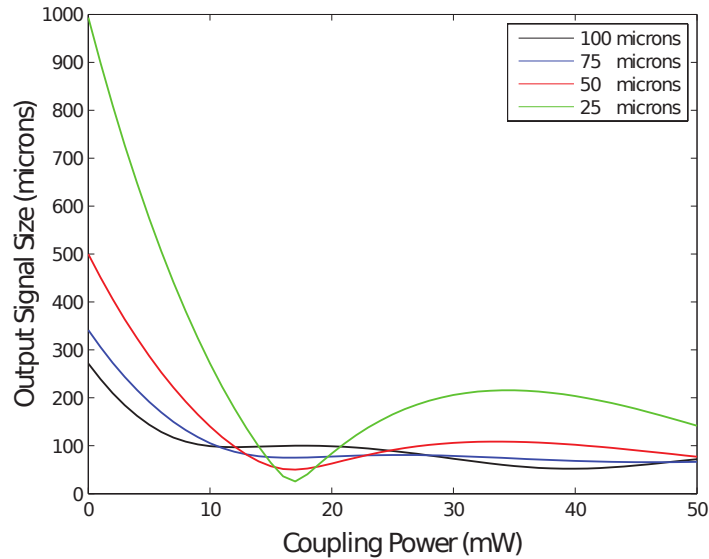
Figure 4.5: Beam propagation as a function of coupling Rabi frequency.

For negative values of δ, κ is real and hence we have an oscillatory solution. For positive values of δ, the refractive index at the core of the LG-01 beam is lower than at the annulus and hence we have a diverging probe. We also note that the value of κ^2 is proportional to P and hence higher values of coupling beam power results in better mode confinement, as seen in Fig. 4.5. Also note that the value of κ^2 is inversely proportional to w_c and hence the waveguiding is strongly dependent on the size of the coupling beam.

Each curve in Fig. 4.5 is plotted for different input probe beam widths. Eqns. (4.11) and (4.16) are used to simulate the beam size after propagating a distance of 10 cm, with $w_c = 800\ \mu$m, $\beta = 105$ and a single photon detuning of 1.5 GHz. We also assumed that $\delta = -\gamma = 100$ KHz. We can observe that the behavior of the probe output size is also dependent on its initial size. Smaller initial size results in faster oscillations. We can also see from Eqn. (4.16) that κ^2 has a dispersive relation with the Raman detuning. Fig. 4.6 depicts this behavior. The output probe size is plotted against the Raman detuning for various input probe sizes.
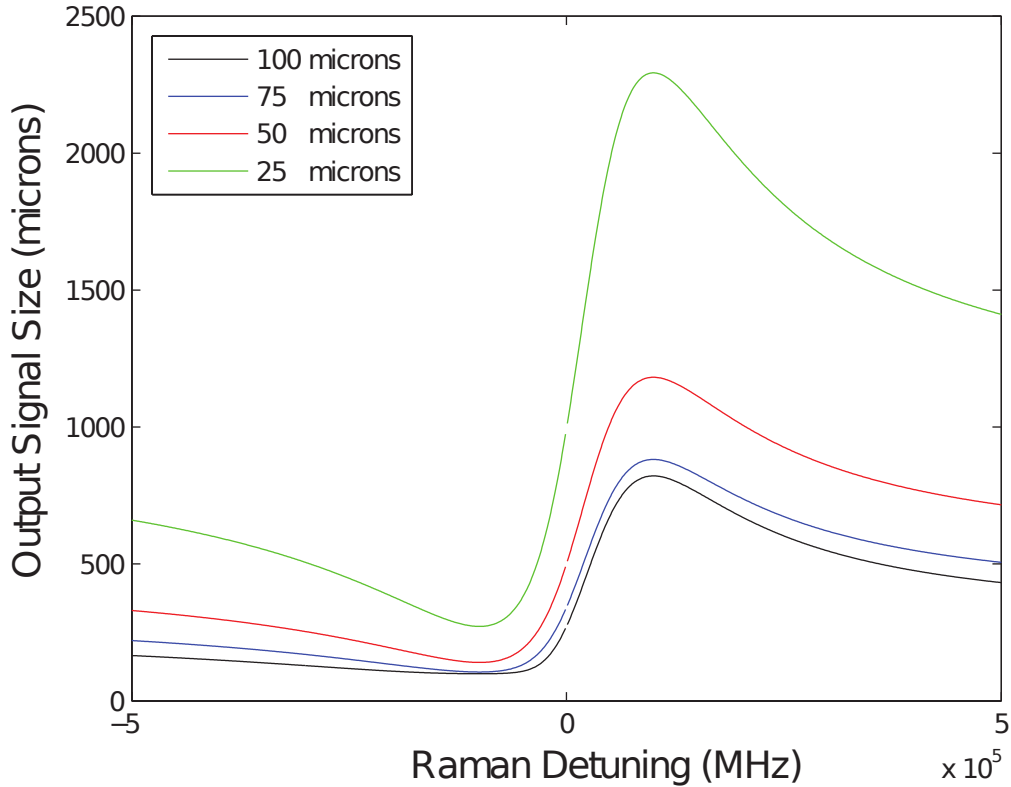
Figure 4.6: Beam propagation as a function of detuning.

The coupling beam power is assumed to be 10 mW. We see that probe size is smaller for negative δ and larger for positive δ. The size approaches the free space value for large δ on either side of zero Raman detuning.

4.2.3 Experiment

The experimental setup shown in Fig. 4.7 consists of a 795 nm external cavity tunable diode laser followed by a tapered amplifier. The beam is split in two at a 50:50 beam splitter. One beam acts as the probe after frequency shifting it by about 3.035 GHz to the red by double passing it through a 1.5 GHz acousto-optic modulator. The other beam acts as the coupling beam which is sent through a spatial filter in order to clean up its mode and is followed by a charge one spiral
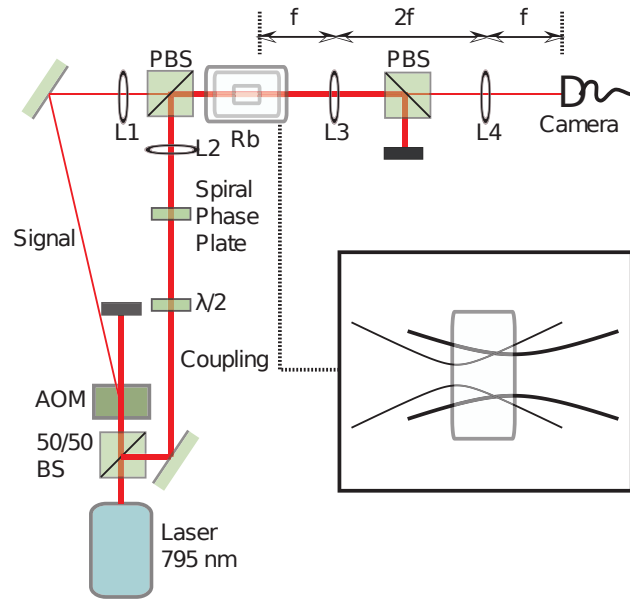
Figure 4.7: The experimental schematic for all optical waveguiding using atomic rubidium vapor. The focusing scheme for control beam (black) and probe (gray) is shown in the inset.

phase plate, resulting in a first order Laguerre Gaussian beam. The orthogonally polarized coupling and probe are then combined at a polarizing beam splitter.

We use a configuration where the coupling focuses at the back face and the probe focuses into the core of the ring coupling beam at the front face of the vapor cell. We use the configuration of focusing coupling beam rather than a collimated beam because we want to show that the probe beam follows the size of the coupling beam. The transmission properties of the beams and two photon characteristics are observed by taking off the spiral phase plate and the lenses L1 and L2. The coupling is filtered at another polarizing beam splitter after the cell. We image the back face of the cell with a 4f imaging system to determine the size of the probe. The anti-reflection coated vapor cell is 5 cm long and contains a natural abundance of rubidium isotopes with a 20 torr neon buffer gas. The vapor cell is placed inside a magnetically shielded oven and is maintained at a
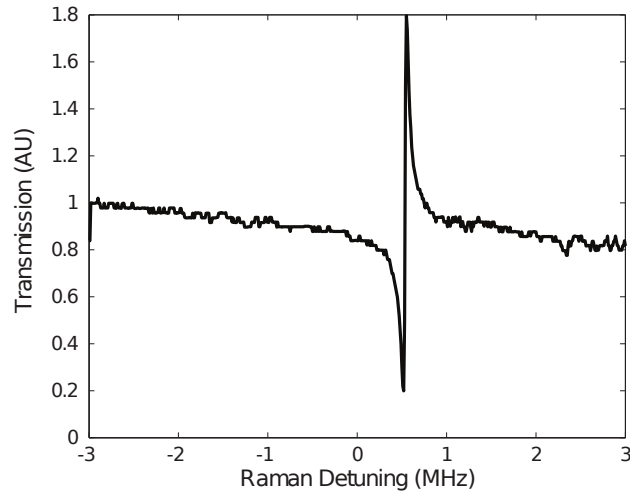
Figure 4.8: The experimental plot of the variation in the transmission of probe versus Raman detuning.

temperature of about 80°C which results in number densities of approximately 10^{12} cm^{-3}. We use a positive single photon detuning, Δ, of about 500 MHz.

The plot showing the transmission of the probe beam as a function of Raman detuning is shown in Fig. 4.8. The coupling and the probe are tuned to be about 500 MHz to the blue of the ^{85}Rb $F = 2$ to $F = (2,3)$ and $F = 3$ to $F = (2,3)$ D1 transitions respectively. Both coupling and probe are collimated and are co-propagating. The dispersion of the medium is obtained by applying Kramers Kronig relations on the observed transmission profile. We obtain a dispersion profile in this manner for various coupling beam powers. Fig. 4.9 shows the plot of the variation of the refractive index versus coupling beam power at a fixed probe frequency with $\delta = -1.5$ MHz. We can see that the refractive index decreases with increasing coupling beam intensity. We choose the probe frequency to be close to Raman resonance such that there is good contrast in refractive index for higher and lower coupling beam powers and away from the absorption dip shown in Fig 4.8. We found that we have optimum guiding at a $\delta = -2$ MHz.

Fig. 4.10(a) shows the refractive index profile along the transverse plane.
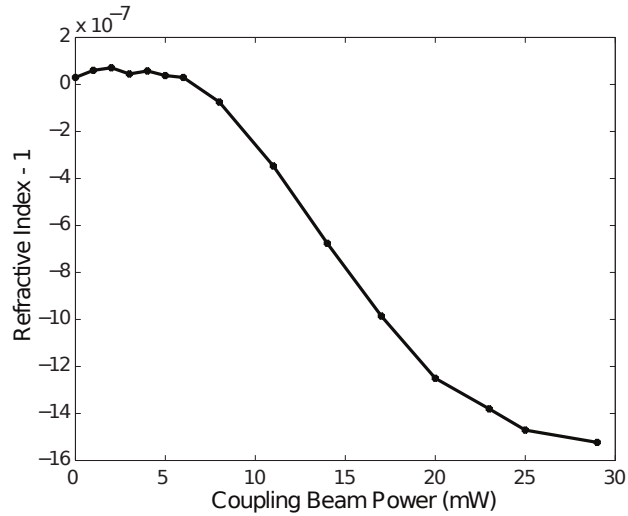
Figure 4.9: The plot of refractive index of the probe, tuned -1.5 MHz away from Raman resonance, as a function of coupling beam power.

White indicates higher refractive index and black, along the ring, is lower refractive index. The intensity profile at the front of the vapor cell is captured with a camera and Eq. (4.15) is used to obtain the refractive index. Fig. 4.10(b) shows the index profile along one of the axes of the beam. We see that we have a refractive index contrast of about 10^{-5} between maximum and minimum refractive indices. We use a single photon detuning of 500 MHz, a Raman detuning of -1 MHz and 30 mW coupling beam power in Eq. (4.15) to obtain the refractive index profiles from a camera snapshot of intensity profile.

Fig. 4.11 shows the main result of the experiment. The coupling beam is converging along the cell and has a focus at the back face of the cell. The snapshots of the probe beam with and without the coupling beam at the back face of the vapor cell are shown in Fig. 4.11(a) and (b). Recall that the probe is focused into the "core" of the coupling beam at the front face as shown in Fig. 4.7(c). The black dashed line is the measured coupling beam intensity profile, the black dotted line is the measured probe intensity and the solid black line is the Gaussian fit to the measured probe intensity. The Gaussian width of the probe is 56 μm. In the
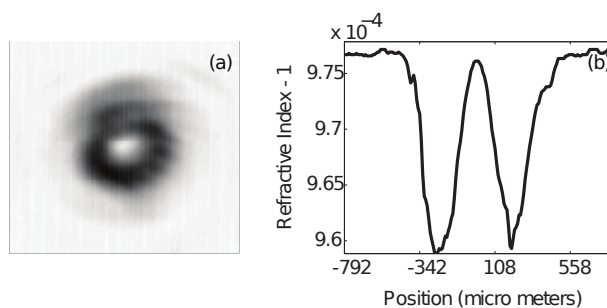
Figure 4.10: (a) shows the spatial variation of refractive index. (b) shows the plot of refractive index versus position along one of the axes.

absence of the coupling beam, the probe beam diverges along the length of the cell as shown by the gray curve in Fig. 4.11(d). In Fig. 4.11(d), the black dashed line is the measured coupling beam profile, gray and black dotted lines are the measured probe beam profiles when the coupling is off and on, respectively, and the solid gray and black lines are Gaussian fits to the dotted lines. The Gaussian widths of the gray and black curves are 102 μm and 35 μm respectively. When the coupling is on, the probe is guided along its core and so the probe beam diameter is smaller at the back face of the cell. For example, the Gaussian width of the probe at the back face is 35 μm with an 18 mW input coupling (black curve of Fig. 4.11(d)). The integrated intensity of the black curve is approximately 43% of the gray curve implying that there is a good coupling of the probe power into the waveguide. Note that the peak intensity of the black curve is more than that of the gray curve. The coupling beam intensity in Fig. 4.11(c) and (d) is normalized to fit in the figure while the probe intensities in Fig. 4.11(d) are relative. The laser beams are slightly elliptical and so the axis mentioned above is along the longer axis.

We saw in Figs. 4.5 and 4.6 the variation of the output probe beam size with the coupling beam power and the two photon Raman detuning. Figs. 4.12 and 4.13 shows the experimental observation of this dependence. We see from Fig. 4.12
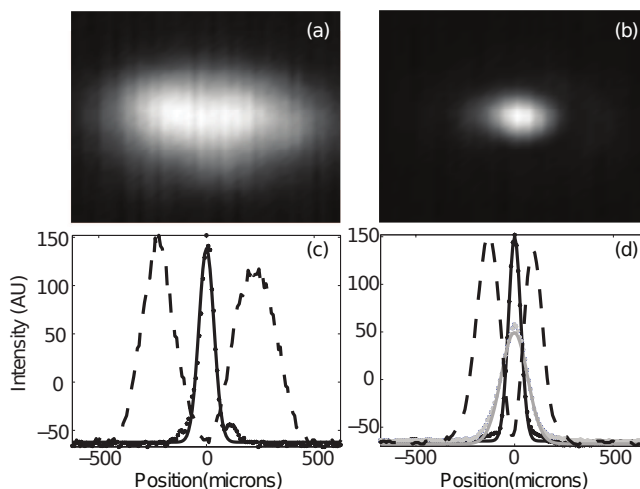
Figure 4.11: The snap shots of the probe beam profile at the back of the vapor cell with the coupling beam off (a) and on (b). Beam profiles along the longer axis of the beams at the front face of the cell (c) and at the back face of the cell (d).

the expected oscillatory behavior, and Fig. 4.13 shows the expected dispersive behavior. The gray (black) curves show the beam size along the horizontal (vertical) axis. We have waveguiding when the Raman detuning is negative and divergence for positive detuning. We also see that we can have waveguiding for a range of frequencies over a bandwidth of few MHz. This means that we can potentially guide optical pulses with bandwidths of a few MHz. Fig. 4.14 shows the output powers for different frequencies. We see that in the frequency range where we have good waveguiding, we also have relatively good transmission of the probe power.

In order to verify that the waveguide is the result of the Raman absorption and not due to other nonlinear effects like four-wave mixing (FWM), we measure the output probe power for various input probe powers as shown in Fig. 4.15. We see that the plot is linear and hence the waveguiding effect is linear in probe power. This also means that the waveguiding effect is not due to self focusing
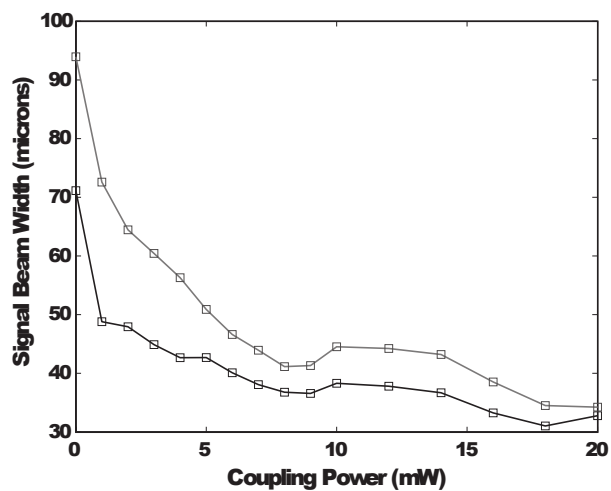
Figure 4.12: Plots of the probe beam size at the back face of the vapor cell versus the control beam power.
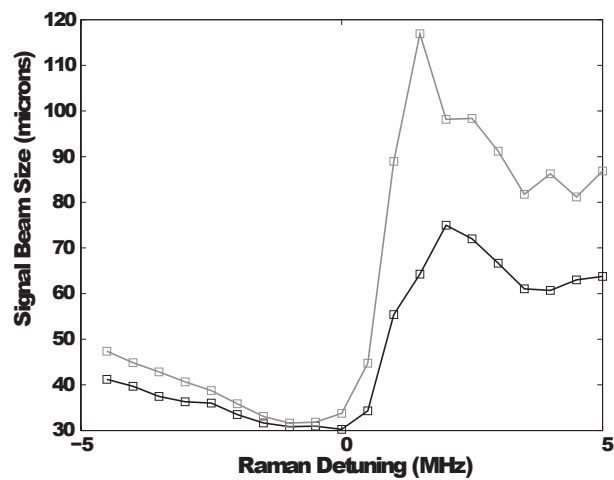

Figure 4.13: Plots of the probe beam size at the back face of the vapor cell versus the Raman detuning
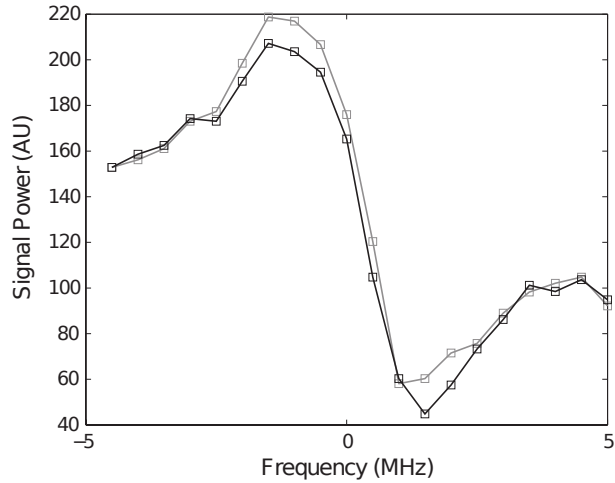
Figure 4.14: The plot of output probe power versus Raman detuning.

effect. Instead it is due to coupling beam dependent focusing. The slope of the linear fit is about 0.43, which means that we couple about 43% of input probe power into the waveguide. This implies that we can expect to guide light of very low power probe without significant loss.

4.2.4 Summary

In summary, we use the intensity dependent refractive index resulting from a Raman transition in a Λ system to create an all optical waveguide. We are able to transmit about 43% of the power along the waveguide, for lengths much greater than the diffraction length, using a low power control beam.

This all optical waveguide can be used to achieve efficient nonlinear processes at very low light levels. For example, in the case of naturally abundant rubidium, we can use one isotope to guide the probe and the other isotope as a medium for the nonlinear processes such as two photon absorption, Stark shift, Kerr effect, etc. Lukin and Imamoğlu [79] suggested the use of rubidium isotopes for two simultaneous, independent nonlinear processes to achieve large Kerr nonlinearities.
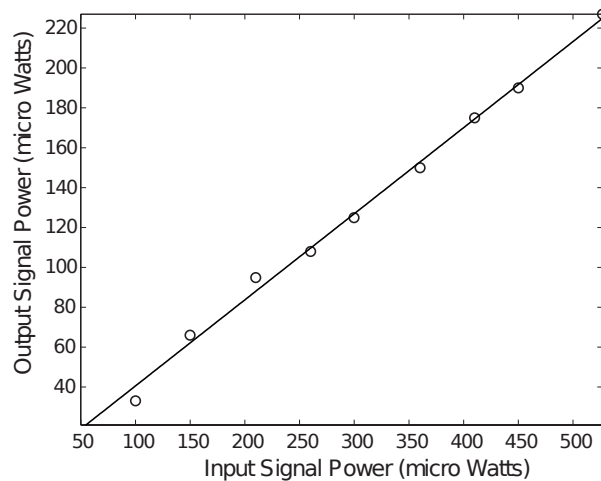
Figure 4.15: The plot of output probe power versus input probe power. The plot is nearly linear, the slope of the linear fit to data is 0.43.

One can also optimize the waveguide to increase the bandwidth and allow for multiple frequency waveguiding. Finally, one can use this waveguide as a building block for an all optical beam-coupler and beam-splitter, similar to solid-state waveguide devices.

4.3 Atomic Prism

4.3.1 Introduction

In the previous section, we saw how modifying the index of refraction using an atomic medium can result in interesting and useful behavior. We will now return to the use of a prism, where the material is no longer glass, but a cloud of hot rubidium; this results in large spectral resolution. Such devices are invaluable in the field of photonics. Common techniques for high resolution spectroscopy use Fourier transform interferometers [80], Fabry-Perot cavities [81–83], optical frequency combs [83–85] and Faraday rotation with polarization optics [86–88].

Here, we present an atomic prism spectrometer which utilizes the steep linear dispersion between two strongly absorbing rubidium (Rb) resonances to achieve high spectral resolution. We demonstrate the sensitivity of the prism by discriminating spectral lines 50 MHz apart with 36% transmission, and 300 MHz apart with 80% transmission. We also spatially separate collinear pump, signal and idler beams resulting from a FWM process [89] with 35 dB suppression over a 1.4 GHz bandwidth. These results highlight the potential for use in interaction free measurements [88], the filtering of entangled photons [90] or frequency modes from atomic interactions, the separation of multiple teeth of an optical frequency comb [91–93], and even the filtering of (frequency) multimode images [94].

The large dispersion near an atomic resonance is well known [95, 96], and its use in spectroscopy has been studied extensively in metal vapors [97–103]. Early experiments have focused on a single absorption [98, 99, 104] or transmission [97] resonance. For example, Finkelstein *et al.* showed that, using the resonance enhancement of dispersion of a single absorption line, a mercury vapor prism could resolve the Raman lines of CO_2 [99]. Related work in the area of interaction-free measurement has shown an impressive filtering of an 80 MHz line with 35 dB suppression near an atomic resonance [88]. However, the transmission of this system is only 10%. It is therefore advantageous to consider using the transparent region between two resonances where, e.g., there is increased bandwidth, decreased frequency-dependent absorption, high transparency and the ability to resolve many spectral lines.

In this section, we present a Rb vapor prism spectrometer that operates in the transparent region between two strongly absorbing resonances with five orders of magnitude greater dispersing power, albeit over much smaller bandwidth, than a standard glass prism. Such a transparent region also gives rise to slow light and has been studied in various systems recently [105]. We show that the number of resolvable spectral frequencies—which is an important feature of this design—is

proportional to the slow light delay-bandwidth product. The delay-bandwidth product for double absorption slow light has been shown to be nearly 50 in Rb [106] and 100 in cesium [107]; therefore, there exists an advantage over electromagnetically induced transparency (EIT) [89] based slow light prisms [97], where the delay-bandwidth products are typically less than one. In addition, the separation of frequency modes is independent of polarization, in contrast to EIT and Faraday anomalous dispersion optical filters.

4.3.2 Theory

Consider a double absorption slow light medium [106] of Rb vapor in an evacuated chamber. The chamber is placed in air as shown in Fig. 4.16a and the shape of the chamber is a prism with an apex angle of θ_0. Assuming that the index of refraction of air is unity, the change in the direction of the beam at the exit interface is small. We can obtain the exit angle of the ray after propagating through the prism as $n(\nu)\sin(\theta_0) = \sin[\theta(\nu)]$, where n is the real part of the index of refraction and $\theta(\nu)$ is the angle made by the ray with the normal of the second surface of the prism as shown in Fig. 4.16b. For $n(\nu) \approx 1$, the angular dispersion of frequencies can be written as

$$\frac{d\theta}{d\nu} \approx A\frac{dn}{d\nu}, \tag{4.17}$$

where we assumed small deflections and A is a geometric factor (of order one) determined by θ_0 and also corrects for misalignment from normal incidence.

The quantity $dn/d\nu$ depends on the system of interest. However, we know that the group index $n_g = n + \nu dn/d\nu \approx \nu dn/d\nu$, for large dispersion. Therefore, we can replace $dn/d\nu$ with n_g/ν. For a medium of length L and a group delay of τ, $n_g/\nu \approx \lambda\tau/L$ where λ is the wavelength and we assumed that $n_g \gg 1$. The group delay in a double absorption system is approximately given by $\tau = \alpha L/\Gamma$ where α is the absorption coefficient at the center of the transparency and Γ is
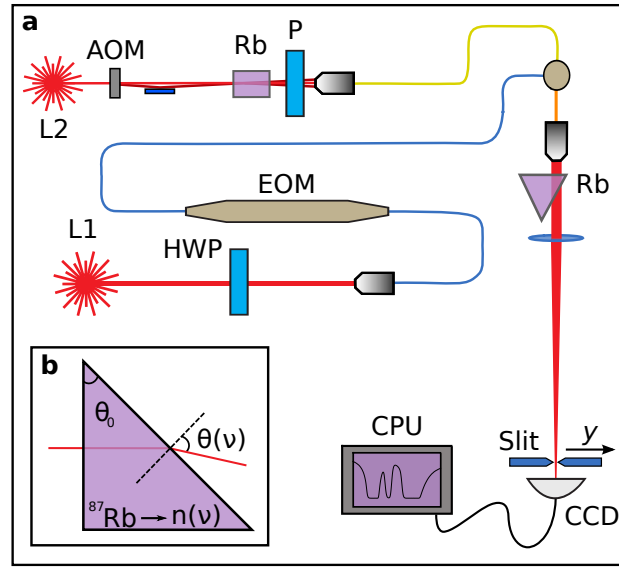
Figure 4.16: (a) The experimental setup for an atomic prism spectrometer. (b) A detailed diagram of the geometry of the prism.

the full width at half maximum of each absorption [106]. The resulting angular dispersion is therefore given by

$$\frac{d\theta}{d\nu} = A\frac{\lambda\alpha}{\Gamma}. \tag{4.18}$$

We are particularly interested in the number of spatially resolvable frequency modes. However, for small frequency changes $\Delta\nu$, $\Delta\theta$ is typically not sufficient to spatially separate each mode. We therefore place a lens of focal length f near the exit face of the prism (or right before the prism), giving a displacement of the beam in the focal plane as $\Delta y = \Delta\theta(\nu)f$. For a beam with a $(1/e^2)$ Gaussian diameter of D before the lens, the Fourier-transform-limited diameter of the beam at the detector is given by $d = \frac{4\lambda}{\pi}\frac{f}{D}$. We then calculate the amount of frequency shift needed for one beam waist displacement of the beam at the detector. Setting $\Delta y = d$, we find

$$\Delta\nu_{\text{min}} = \frac{d}{fA}\frac{L}{\lambda\tau} = \frac{4\Gamma}{A\pi\alpha D}. \tag{4.19}$$

This quantity gives us the minimum frequency resolution of the prism. Similarly, to spatially separate *multiple* frequency components, we require $\Delta y_{\mathrm{max}}/d \gg 1$, where Δy_{max} is the maximum deflection for the system. That is, we want

$$\frac{\Delta y_{\mathrm{max}}}{d} = \frac{f\lambda A}{d}\frac{\tau \Delta \nu_{\mathrm{max}}}{L} \gg 1, \tag{4.20}$$

where $\Delta \nu_{\mathrm{max}}$ is the bandwidth of the prism. We see that this ratio is proportional to the delay-bandwidth product over unit length and note that f/d is linearly related to D, the Gaussian beam diameter before the lens.

In order to maximize $\Delta y_{\mathrm{max}}/d$ we need a slow light system with a large delay-bandwidth product, such as a double Lorentzian absorption system. The bandwidth of the system is governed by the separation between the two absorptions and the delay is dependent on the optical depth. The hyperfine absorption lines in alkali metals (e.g., Rb or Cs) provide ideal double absorption resonances for this purpose.

The simplified model discussed above can predict our experimental results. However for more accuracy, we need to consider the effect of a centroid shift due to differential absorption across the transverse cross-section of the beam in the prism. Since there is a uniform extinction coefficient in the prism, the part of the beam with the longest path length within the prism will have the largest amount of loss. The intensity of the beam after propagating through the prism is given by $I = I_0 \exp[-2(x - x_0)^2/w^2]\exp(-\alpha L_0 x/x_0)$ where I_0 is the intensity at the center of the beam before the prism, α is the absorption coefficient, L_0 is the propagation distance for the centroid when there is no absorption, w is the Gaussian beam radius $(D/2)$ and x_0 is the distance of the beam from the vertex of the prism. The intensity I can be rewritten as $I = I'\exp\{-2\left[x - (x_0 - \alpha L_0 w^2/4x_0)\right]^2/w^2\}$ where $I' = I_0 \exp(-\alpha L_0)\exp(\alpha^2 w^2 L_0^2/8x_0^2)$. The centroid of the Gaussian beam is thus shifted by $\alpha L_0 w^2/4x_0$. For the experimental results below, this shift is approximately 2-4% of the width of the beam. We note that L and τ in all the
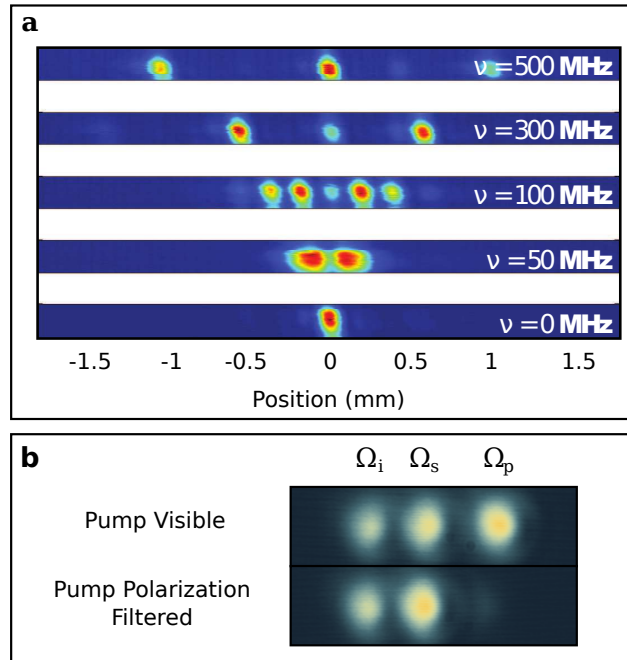
Figure 4.17: Experimental data of the separation of multiple frequency modes with an atomic prism spectrometer. (a) The transverse profile of the beam at the detector for different modulation frequencies. (b) The separation of the different modes generated from FWM.

equations correspond to the length of propagation and delay for the *centroid* of the exit beam.

4.3.3 Experiment

The schematic of the experimental setup is shown in Fig. 4.16. We analyze two sources: the frequency sidebands generated by laser L1 passing through an EOM, or the FWM signal generated by the nonlinear interaction of laser L2 with atomic Rb. As we change the frequency of the source between the atomic resonances, we see a shift in the position of the beam at the camera. We note that the displacement of the beam as well as its focal spot size increase for longer focal distance. We also consider two atomic prisms to emphasize different aspects of

this design. The first prism contains naturally abundant Rb, resulting in steep dispersion at the cost of bandwidth. The second prism contains isotopically pure ^{87}Rb, offering a larger transparent region. For clarity, we detail each source, and each prism:

Frequency source 1. A narrow line width external cavity diode laser at 780 nm is tuned near the hyperfine resonances of the D$_2$ line of Rb and coupled into a fiber EOM which is driven by an oscillator. A $\lambda/2$ wave plate is used to control the efficiency of the sideband creation in the EOM.

Frequency source 2. A narrow line width external cavity diode laser is frequency shifted with a 1.5 GHz acousto-optic modulator, double passed, to produce two linearly but orthogonally polarized coherent beams separated by 3.035 GHz. These beams are combined at a polarizing beam splitter and passed through a magnetically shielded, heated vapor cell with naturally abundant Rb and 20 Torr neon buffer gas. The frequencies and powers of each beam are adjusted to produce collinear FWM within the vapor cell. In particular, the signal beam is tuned to the blue of the $F = 3 \rightarrow F' = \{2, 3\}$ ^{85}Rb transition and the pump beam, separated by 3.035 GHz in frequency from the signal beam, is therefore to the blue of the $F = 2 \rightarrow F' = \{2, 3\}$ ^{85}Rb transition. The output is polarization filtered to remove the pump and coupled into a single mode fiber.

1) The naturally abundant prism. This prism has a 79° apex angle and the beam is 20° from perpendicular incidence, giving a geometric factor $A \approx 2$. The beam was focused gently through the prism and on to a camera; the cell was 3 cm from the lens, which was 38 cm from the camera. The Gaussian diameter of the beam before the cell was $D = 1.6$ mm and the centroid propagates about 6 mm through the prism. The focused, Gaussian diameter d at the camera is approximately 90 μm.

2) The isotopically pure ^{87}Rb prism. The prism contains approximately 2% ^{85}Rb, heated to approximately 114°C, and has a 45° apex angle. The light

enters the vapor cell perpendicular to the face of the Rb prism and exits through the other side as shown in Fig. 4.16b, resulting in a geometric factor of $A \approx 1$. The beam has a Gaussian diameter of $D = 3.8$ mm and the centroid propagates about 3.1 mm through the prism. The beam is focused on the camera 1 m away. The focused, Gaussian diameter d at the camera is approximately 260 μm.

The light from each source is separately passed through a hot Rb vapor prism and either focused onto an 8-bit CCD camera or a slit in the focal plane with a power meter. The intensity profile is observed for each source. We consider two different prisms to emphasize 1) high dispersion or 2) large bandwidth. Even though the dispersion increases for higher temperatures of the vapor cell, the effective bandwidth of the system decreases due to increased absorption. At our working temperature, the bandwidth of our system is about 1.1 GHz with 36% transmission for the naturally abundant prism, and 1.8 GHz with 80% transmission for the isotopically pure ^{87}Rb prism. Note that, for each prism, we report data only in the largest transparency window; however, there are other, narrower regions for each prism which result in larger dispersion.

Let us first consider the source from laser L1 using the naturally abundant prism. The frequency dependent deflection is quantified by first turning off the EOM and tuning the frequency of L1 to the center of the transparency between the two ^{85}Rb resonances. Turning on the EOM results in frequency sidebands. Different frequency bands in the signal are spatially separated after the prism and the resultant spatial distribution of intensities is recorded at the camera. Fig. 4.17a shows the data for different modulation frequencies. The central spot is the zeroth order (unmodulated) frequency followed by the first order and second order sidebands to either side. The first order sidebands are visible up to the modulation frequency of 550 MHz. Frequency dependent absorption causes the change in relative intensities of each mode; one can obtain the exact spectral

information of the input signal by correcting for the frequency dependent losses at the vapor cell. The transmission of the zeroth order beam through the prism is approximately 36%. With a bandwidth of 1.1 GHz, we find that the displacement at the camera is 1.95 μm/MHz. With a 0.38 m focal length lens, this corresponds to an angular dispersion of 5.1 μrad/MHz, and so $dn/d\nu \approx 2.6 \times 10^{-12}$ Hz^{-1}. Compare to a glass prism, with $dn/d\nu \approx 4 \times 10^{-17}$ Hz^{-1}. We also find $\Delta y_{\mathrm{max}} = 2.15$ mm and $\Delta \nu_{\mathrm{min}} = 50$ MHz, which are in fair agreement with the predictions of 2.6 ± 0.4 mm and 37 ± 6 MHz.

Let us next consider the source from laser L2 using the isotopically pure ^{87}Rb prism. By using the transparent region between the ^{87}Rb resonances as well as the much larger nonlinear dispersive region outside the resonances, we spatially separate different frequencies resulting from a collinear FWM process in ^{85}Rb. The setup is similar to the FWM discussed in reference 108. Signal, idler and pump beams at the output of a Rb vapor cell are coupled into a fiber (yellow in Fig. 4.16a). Signal and pump beams fall in the highly dispersive region between the resonances. The magnitude of the deflection is different for each mode due to the different refractive indicies of Rb at their respective frequencies. The idler beam, which is about 6 GHz to the blue of signal beam, is farther from resonance and hence experiences less deflection. Fig. 4.17b shows the image at the detector. The central spot is the signal beam and the left and right spots are of idler and pump, respectively. The transmission of the signal photons is 80%, falling in the transparent region of the prism. We see that each mode is well separated with low loss

In fact, using this highly transparent prism, we find that beams separated by 600 MHz have greater than 30 dB relative suppression, with a max of about 35 dB across the transparent region of 1.4 GHz. The results are shown in Fig. 4.18, where P_0 is the power, measured through the slit, of frequency mode ν and $P(\Delta)$ is the power, measured through the slit, of frequency mode $\nu + \Delta$ if the EOM were
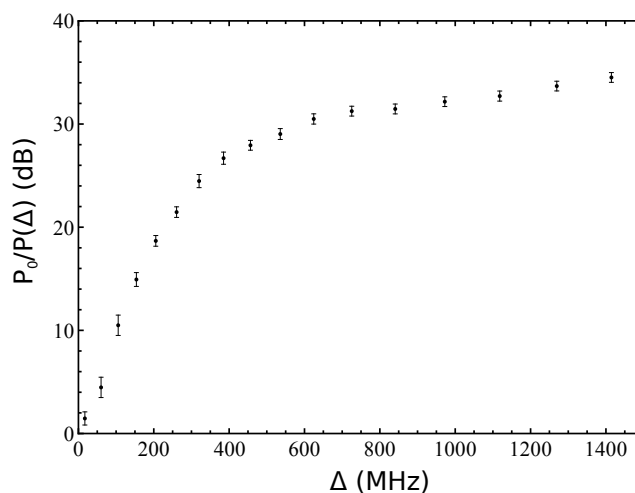
Figure 4.18: The suppression of one beam relative to another beam, separated by a frequency Δ.

active. The reference frequency ν is set to the blue edge of the large transparency region of the isotopically pure ^{87}Rb prism. We find that modes approximately 300 MHz apart are well separated.

The sensitivity of the spectrometer using the naturally abundant Rb prism is quantified using a similar configuration to Fig. 4.16. Instead of a CCD camera we use a position sensitive quadrant detector. We use the EOM at a modulation frequency of 1 GHz and then adjust the frequency of the laser such that one of the first order sidebands is in the transparent region between the two Rb^{85} hyperfine resonances. The central peak and the other sidebands are in a highly absorbent region. The sideband frequency is then modulated using an external arbitrary waveform generator. For this measurement we modulated the frequency of the sideband by 10 kHz at a rate of 60 kHz. The signal from the quadrant detector is filtered at 30-100 kHz. The power of the beam after passing through the cell was roughly 300 μW. Using the same methods as in reference 109 and chapters two and three, the sensitivity of the spectrometer is found to be approximately 20 Hz/$\sqrt{\text{Hz}}$, which corresponds to a SNR of one. This is almost four orders

of magnitude improvement over the standard glass prism technique [109]. The theoretical limit for a shot noise limited system is less than 1 Hz/$\sqrt{\text{Hz}}$, but we were limited by technical noise.

4.3.4 Summary

We have demonstrated a highly dispersive atomic prism. We showed that the number of resolvable spectral frequencies is proportional to the delay-bandwidth product, which makes a slow light double absorption system ideal for an atomic prism. These ideas can be generalized to larger bandwidth systems; for example, one can utilize linear dispersion between the D_1 and D_2 absorption frequencies of Rb [110]. Furthermore, we demonstrated a spatial separation of the pump, signal and idler beams from a FWM process in Rb and find a suppression of 35 dB between frequencies separated by 1.4 GHz with 80% transmission. Applications for this technique exist in, for example, efficiently and cleanly separating number squeezed signal and idler beams for quantum metrology and information purposes.

4.4 Conclusion

In this chapter, we have shown that weak values provide a powerful way to measure the change of an optical frequency, that coherent Raman processes can alter the propagation characteristics of light, and that even natural atomic resonances can be used for spectroscopy. By combining weak values with the dispersion possible in Rb or Cs, one might be able to achieve quantum limited frequency metrology and spectroscopy.

Additionally, the signal and idler beams resulting from the FWM process in rubidium have been shown to be number squeezed and are expected to be entangled. Thus, FWM in rubidium is a potential source for narrow-band entangled

photons. However, the residual pump noise in the signal and idler beams and the spontaneous emission noise in hot atomic vapor make such experiments challenging. We can use the rubidium prism to separate different frequency components spatially and reduce the amount of crosstalk between the beams.

5   Quantum Undemolition: Restoring Entanglement

5.1   Introduction

In chapter one, we laid the foundations for quantum measurement as a means to understand the weak value, its advantages and its limitations. Fundamental to this discussion is the concept of a weak measurement applied to a quantum state: an act which perturbs the state weakly, and from which we can gain a limited amount of information. In the following chapter, instead of focusing on how weak measurements can result in precision measurement, we will explore how they can be used to modify a two-party state in a desirable way. In particular, we will see how one can restore the entanglement between a pair of particles, even in the presence of statistical noise.

The notions of "state" and "measurement" were parts of the early framework of quantum mechanics and are still active and vibrant concepts for study. Current fundamental and applied topics of interest related to the state and measurement of a quantum system include the quantum Zeno effect [111–113], weak values [10, 15, 30, 114, 115], quantum state discrimination [116–118] and precision measurements [119, 120]. Recently, attention has turned to the use of exotic states of light to perform important tasks, e.g., entangled [79, 113, 121, 122] or squeezed

[47, 120, 123, 124] states. In fact, many current applications of protocols in quantum computing and quantum communication require the control of entanglement in a quantum system. However, this control is often hampered by decoherence effects in the storage and/or transfer of these quantum building blocks.

One idea which has been used to overcome the effects of decoherence is entanglement distillation, where one sifts through a large ensemble of non-maximally entangled systems to distill a much smaller ensemble of highly entangled systems. This idea has been demonstrated by Kwiat *et al.* [125] for an optical system based on polarization entanglement.

While entanglement distillation is powerful, there is another way to restore entanglement in a quantum system. Ueda and Kitagawa [126] introduced the idea of reversing a measurement, thereby undoing the decoherence of a quantum system. This original work quickly spurned a number of interesting results [127–133]; they show that when an unknown initial state is disturbed by a *known* measurement, this measurement can be probabilistically reversed. The result is a final state equivalent to the initial state, or at least having a fidelity closer to the initial state than would be found without the reversal procedure [127, 128, 132].

Entanglement distillation and measurement reversal have been connected in a paper by Sun *et al.* [133] where they examine how the entanglement decreases when the entangled qubits are locally disturbed by either amplitude damping or a null result weak measurement. Then, knowing the strength of the disturbance, they put each qubit through a local reversal process, which in many cases will regain some of the lost entanglement.

In this chapter, we propose a procedure which extends this idea to a system with statistical noise. We derive analytic results for a maximally entangled Bell state and include simulations demonstrating how correcting the random disturbance (in amplitude and phase) via a local weak measurement on one particle results in an average increase in the entanglement, fidelity, or both. We conclude

by proposing a simple experimental implementation using polarization entangled photons.

5.2 Theory

Let us begin by considering the polarization state of two photons in the $\{|H\rangle, |V\rangle\}$ basis. We can create photon pairs using a variety of different processes; for entangled photons, a common choice is spontaneous parametric down conversion (SPDC) in a nonlinear crystal, where one high energy photon generates two lower energy photons, conserving energy and momentum. The state of our system can be represented by the density matrix ρ in the joint Hilbert space $\mathcal{H}_A \otimes \mathcal{H}_B$ of both photons A and B. For a pure state, this looks like $\rho = |\Psi\rangle\langle\Psi|$, where

$$|\Psi\rangle = a|HH\rangle + b|HV\rangle + c|VH\rangle + d|VV\rangle, \tag{5.1}$$

$\{a, b, c, d\}$ are complex coefficients, and where e.g., $|HV\rangle = |H\rangle_A \otimes |V\rangle_B$.

We can now characterize the disturbance that represents how this state will be altered. In the case of photons, the alteration could be caused by propagation through a fiber or a polarization-dependent reflection off of an interface. Let us define an operator which acts upon a single photon, given by

$$\hat{D} = e^{i\phi_H}\hat{\Pi}_H + e^{i\phi_V}\hat{\Pi}_V, \tag{5.2}$$

where $\hat{\Pi}_{\{H,V\}}$ are the projectors onto $\{|H\rangle, |V\rangle\}$ and $\phi_{\{H,V\}}$ are the complex phases describing the disturbance of each polarization component. The real part of $\phi_{\{H,V\}}$ describes a phase shift of that polarization, whereas the imaginary part describes an attenuation (when $\text{Im}[\phi_{\{H,V\}}] > 0$) or an amplification (where $\text{Im}[\phi_{\{H,V\}}] < 0$). We restrict our analysis to the former.

Using this disturbance operator, we can calculate the normalized state of our photons after the disturbance in a straightforward manner:

$$\rho' = \frac{(\hat{D} \otimes \hat{\mathbb{1}})\rho(\hat{D} \otimes \hat{\mathbb{1}})^\dagger}{\text{Tr}[(\hat{D} \otimes \hat{\mathbb{1}})\rho(\hat{D} \otimes \hat{\mathbb{1}})^\dagger]}, \tag{5.3}$$

where only photon A has been disturbed. One might ask, how disturbed is the state of our biphoton? There are two immediate ways one might answer this.

First, we could look at the fidelity of the states, i.e., how similar are the states ρ and ρ'? The standard measure of fidelity is defined to be

$$\mathcal{F}(\rho, \rho') = \text{Tr}\left[\sqrt{\sqrt{\rho}\rho'\sqrt{\rho}}\right], \tag{5.4}$$

where $0 \leq \mathcal{F} \leq 1$, with $\mathcal{F} = 1$ implying $\rho = \rho'$.

However, we may only be interested in a certain aspect of the state in question, e.g., its entanglement. We could then look at how the entanglement changes after the disturbance. For bipartite, two-state particles, the standard entanglement measure is known as concurrence [134], and is defined as $C(\rho) = \max[0, \lambda_1 - \lambda_2 - \lambda_3 - \lambda_4]$, where $\{\lambda_i\}$ are the ordered eigenvalues of the matrix R:

$$R = \sqrt{\sqrt{\rho}\tilde{\rho}\sqrt{\rho}}, \tag{5.5}$$

with the spin-flipped matrix $\tilde{\rho} = (\sigma_y \otimes \sigma_y)\rho^*(\sigma_y \otimes \sigma_y)$. The concurrence has the property $0 \leq C(\rho) \leq 1$, where separable states have $C = 0$, and $C = 1$ corresponds to a maximally entangled state.

We will restrict the calculation of these two measures to particular cases. Let us consider the popular, maximally entangled singlet state, written in the $\{H, V\}$ basis as

$$|\Psi^-\rangle = \frac{|HV\rangle - |VH\rangle}{\sqrt{2}}. \tag{5.6}$$

Depending on the type of disturbance we choose to consider, we can obtain a variety of results. Let us first consider the case of amplitude damping of the
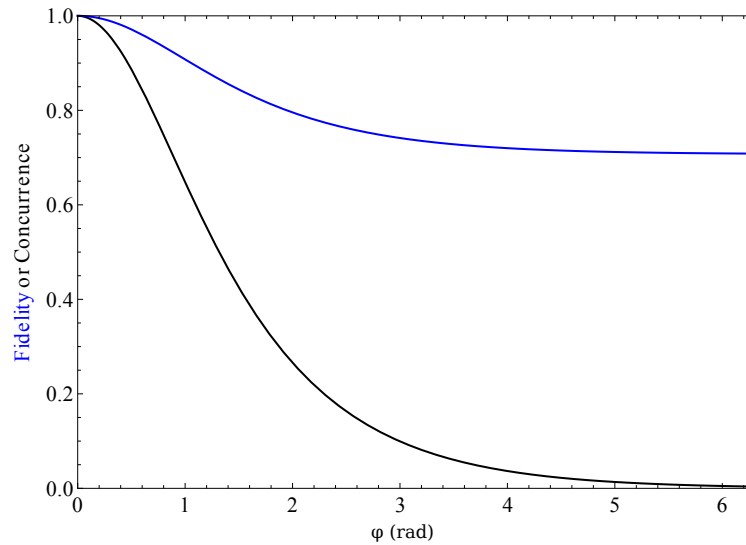
Figure 5.1: The fidelity and concurrence of a singlet state after an amplitude damping disturbance of strength ϕ of the horizontal polarization of one photon.

horizontal polarization, where $\phi_H = i\phi$ and $\phi_V = 0$ with $\phi > 0$. In this case,

$$C(\rho') = \text{sech}(\phi) \tag{5.7}$$

$$\mathcal{F}(\rho, \rho') = \sqrt{\frac{1 + \text{sech}(\phi)}{2}}. \tag{5.8}$$

These quantities are shown in Fig. 5.1.

We can instead consider a disturbance of the *phase* of the horizontal polarization of photon A, where $\phi_H = \phi$ is real. In this case, the concurrence is unaffected, but the fidelity is reduced as

$$\mathcal{F}(\rho, \rho') = \sqrt{\frac{1 + \cos(\phi)}{2}}, \tag{5.9}$$

and is shown in Fig. 5.2.

We know that these effects can be undone by performing a second weak measurement. Let us consider altering the state of the unaffected photon B by performing a weak measurement of the same form as $\hat{D}$. We shall represent the
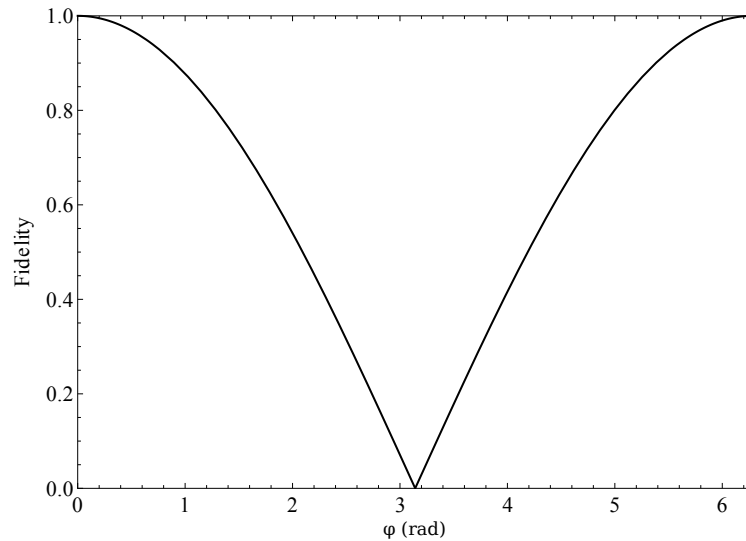
Figure 5.2: The fidelity of a singlet state after phase shifting the horizontal polarization of one photon by an amount ϕ.

measurement on B by the operator $\hat{D}'$, and the new state is given by

$$\rho'' = \frac{(\hat{\mathbb{1}} \otimes \hat{D}')\rho'(\hat{\mathbb{1}} \otimes \hat{D}')^\dagger}{\text{Tr}[(\hat{\mathbb{1}} \otimes \hat{D}')\rho'(\hat{\mathbb{1}} \otimes \hat{D}')^\dagger]}, \tag{5.10}$$

where $\hat{D}'$ is characterized by the parameter $\phi'_{\{H,V\}}$.

Let us again consider the singlet state with an amplitude damping of the horizontal polarization of photon A by an amount $\phi_H = i\phi$, where the fidelity and concurrence are given by Eqs. (5.7) and (5.8). We may guess that the the appropriate measurement strength on photon B is given by $\phi'_H = \phi_H$, i.e., the two "disturbances" are equal. This is indeed the case for both $\mathcal{F}$ and C:

$$C(\rho'') = \text{sech}(\phi - \phi') \tag{5.11}$$

$$\mathcal{F}(\rho, \rho'') = \sqrt{\frac{1 + \text{sech}(\phi - \phi')}{2}}. \tag{5.12}$$

Similarly, for a phase shift ($\{\phi_H, \phi'_H\} \in \mathfrak{R}$), we obtain

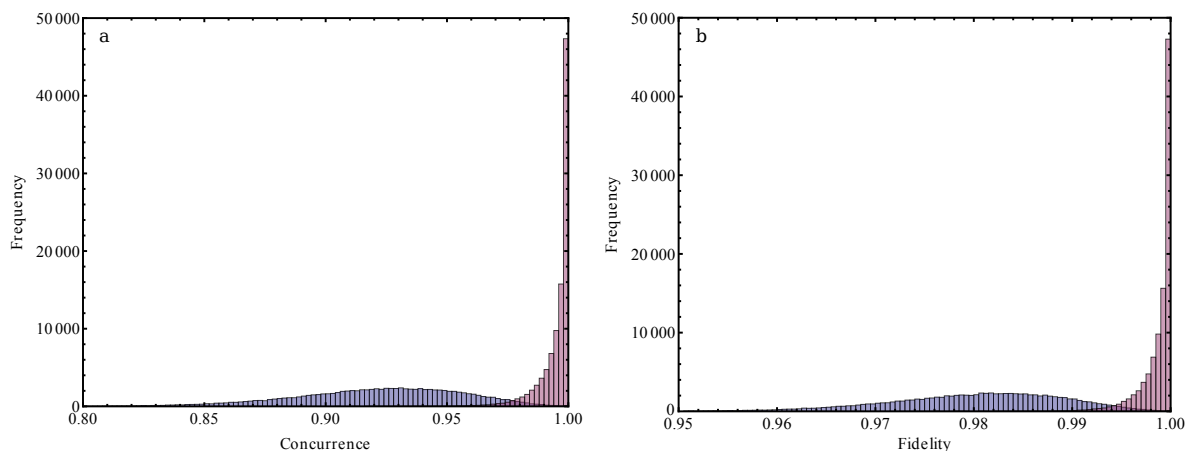$$\mathcal{F}(\rho, \rho'') = \sqrt{\frac{1 + \cos(\phi - \phi')}{2}}. \tag{5.13}$$

Figure 5.3: The (a) concurrence and (b) fidelity probability distributions with a Gaussian random amplitude damping disturbance ($\phi_a = 0.4$ and $\sigma = 0.1$) along with the correction.

Therefore, if we know the nature and strength of the disturbance on photon A, we can undo the effect by applying an analogous disturbance to photon B. This feature of measurement is well known [133], and offers a robust way of restoring the entanglement in your system at the cost of reducing transmission rate.

In the following section, we will discuss how these results are altered when the disturbance is statistical in nature.

5.3 Results

We have seen how the disturbance caused by environmental coupling can reduce entanglement between a pair of photons. We have also seen how we can restore the state to its original form, given information about the disturbance. We now ask the question: what if the disturbance is statistical in nature?

To consider this possibility, we replace ϕ in the equations above with a Gaussian random variable $\widetilde{\phi}$, with average $\langle \widetilde{\phi} \rangle = \phi_a$ and variance $\sigma^2 = \langle \widetilde{\phi^2} \rangle - \langle \widetilde{\phi} \rangle^2$. We have chosen a Gaussian distribution as the most general, based on the central limit
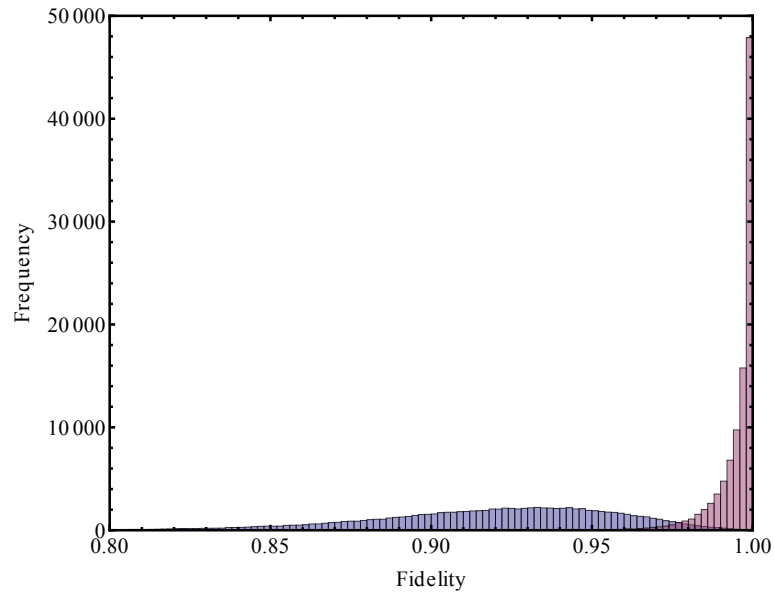
Figure 5.4: The fidelity probability distribution with a random phase shifting disturbance ($\phi_a = \pi/4$ and $\sigma = \pi/16$) along with the correction.

theorem. We again consider a singlet state, and the correcting weak measurement will be set to the average strength of the disturbance, namely, ϕ_a.

If we first consider amplitude damping, we find that not only does the correction improve the concurrence and fidelity on average, but there is a significant reduction in the standard deviation of both quantities. We plot a simulation of the concurrence and fidelity in Fig. 5.3 for $N = 10^5$ random samplings, with $\phi_a = 0.4$ and $\sigma = 0.1$. The concurrence improved from $\langle C \rangle = 0.92 \rightarrow 0.995$ with $\sigma_C = 0.035 \rightarrow 0.0069$. Similarly, the fidelity improved from $\langle \mathcal{F} \rangle = 0.980 \rightarrow 0.999$ with $\sigma_{\mathcal{F}} = 0.0089 \rightarrow 0.0017$. That is a factor of 5 reduction in the spread of the concurrence and fidelity.

We also consider the fidelity when there is a random phase shift on one photon. The results are plotted in Fig. 5.4 for $N = 10^5$ random samplings with $\phi_a = \pi/4$ and $\sigma = \pi/16$. We find that the fidelity improved from $\langle \mathcal{F} \rangle = 0.980 \rightarrow 0.999$ with $\sigma_{\mathcal{F}} = 0.0089 \rightarrow 0.0017$.
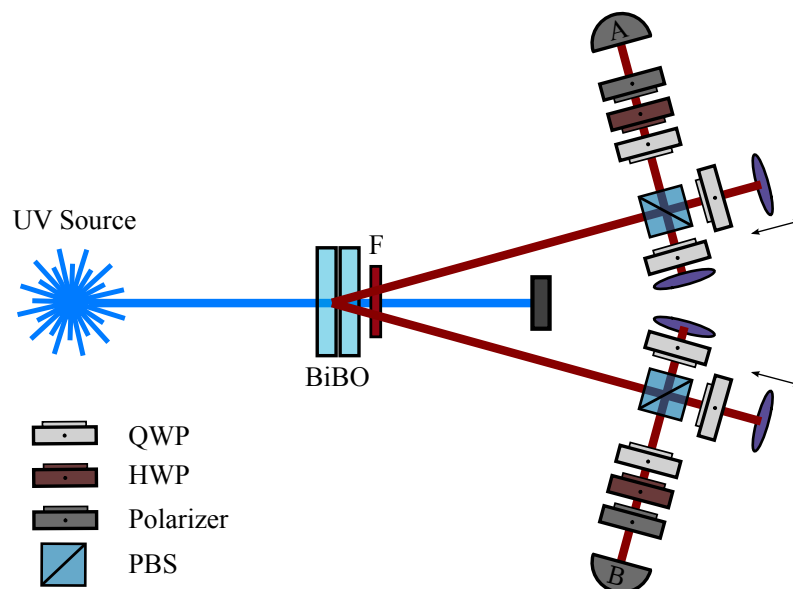
Figure 5.5: The experimental setup to test the quantum undemolition of polarization entangled photon pairs.

There is a straightforward optical implementation to test these results, as shown in Fig. 5.5. Entangled photons from SPDC are input into two independent Michelson interferometers made up a PBS, two QWPs and a mirror on a translation stage. The QWPs control the amplitude of the respective polarization component of the photons in the output port. The translation stage controls the phase shift of the horizontal polarization component of the photons in the output port. One photon obtains a random (known) disturbance and the other photon obtains a static correction. Tomography is done on the output photons with polarization analyzers.

5.4 Conclusion

We have seen that for an ensemble of randomly disturbed photons, a static weak measurement can improve the concurrence and fidelity of the biphotons and signif-

icantly reduce their variance. The correction is made nonlocally; i.e., we measure the unperturbed photon in order to correct the disturbance on its pair. This feature is desirable from a quantum information perspective where highly entangled resources must be transmitted with good fidelity over long distances. We have provided simulations and proposed a simple experimental design to test these results.

6   Conclusion

The focus of this thesis has been to explore the usefulness of quantum measurement in the context of quantum optics. A large portion of this work focused on pre- and post-selected weak measurements to amplify small quantities, e.g. the motion of a mirror or the change in the frequency of a laser. We also found that the properties of alkali metals can be used to guide light for use in precision measurement and spectroscopy. We concluded with a demonstration of how weak measurements can even be used to distill entanglement, despite a random noisy process. Let us quickly review these results.

In chapter two, we presented our first work in weak values, where the small deflection of an optical beam was amplified. This amplification was independent of the source of the deflection and reached amplification factors of over 100. The weak value experimental setup, in conjunction with a lock-in amplifier, allowed the measurement of 560 frad of mirror deflection which was caused by 20 fm of piezo actuator travel. This technique does not beat the ultimate limit for a beam deflection measurement, yet it does have a number of improvements over other schemes: (1) the reduction in technical noise; (2) the ability to use high power lasers with low power detectors while maintaining the optimal SNR; and (3) the ability to obtain the ultimate limit in deflection measurement with a large beam radius.

We continued our study of weak values in chapter three by considering a different regime, where the deflection k was large, and the phase ϕ was small. In this limit, we can perform a measurement of the phase ϕ and obtain an amplification proportional to the inverse weak value A_w^{-1}. This method is comparable to the sensitivity achievable using balanced homodyne techniques, yet only the dark port of the interferometer is measured; therefore, the split-detector can have a low saturation intensity owing to the large attenuation. This design, like other weak value techniques, has the added benefit of reduced technical noise.

In chapter four, we presented three experiments which demonstrate the use of dispersion to (1) make precision measurements with weak values, (2) guide light beyond the Rayleigh range and (3) spatially separate multiple frequency modes. In section one, with only 2 mW of continuous wave input power, we measured a frequency shift of 129 ± 7 kHz/$\sqrt{\text{Hz}}$ over a range of 140 GHz. A large percentage ($\sim 90\%$) of the light used in the interferometer can then be sent off to another experiment, allowing for real-time frequency information during data collection. In section two, we used the intensity-dependent refractive index resulting from a Raman transition in a Λ system to create an all optical waveguide with 43% transmission for lengths much greater than the diffraction length. In section three, we demonstrated a highly dispersive atomic prism that can separate the modes generated from FWM with high transparency and good suppression. While each experiment was quite different, we are interested in how the dispersion alters the properties of the beam. By incorporating weak values with this dispersion, very high frequency resolution should be possible.

Chapter five extended an idea first demonstrated by Ueda and Kitagawa [126], where the entanglement and fidelity of a quantum state, having been disturbed, can be restored. We showed that even if the disturbance is statistical in nature, a static correction is capable of not only improving the average concurrence and fidelity of the state, but also greatly reducing the spread of each of these quantities.

Such a technique is valuable for quantum information and communication, where the degradation of entangled states is unavoidable.

As demonstrated in this thesis, quantum measurement can be a subtle yet exciting area of study, and the field of quantum optics provides a perfect test bed. Research on weak values and weak measurements is still in its infancy with new results and applications being released daily. The results presented here give evidence for the power of these techniques, and provide many avenues for future work.

Bibliography

[1] I. Newton, *Opticks* (Royal Society, London, 1704).

[2] J. C. Maxwell, "On physical lines of force," Philosophical Magazine and Journal of Science **4**, 161 (1861).

[3] A. Einstein, "ber einen die erzeugung und verwandlung des lichtes betreffenden heuristischen gesichtspunkt," Annalen der Physik **322**, 132 (1905), ISSN 1521-3889.

[4] P. A. M. Dirac, "The quantum theory of the emission and absorption of radiation," Proceedings of the Royal Society of London. Series A **114**, 243 (1927).

[5] M. A. Nielsen and I. L. Chuang, *Quantum Computation and Quantum Information* (Cambridge University Press, New York, 2000).

[6] T. D. Newton and E. P. Wigner, "Localized states for elementary systems," Rev. Mod. Phys. **21**, 400 (1949).

[7] W. O. Amrein, "Localizability for particles of mass zero," Helv. Phys. Acta **30**, 149 (1969).

[8] M. O. Scully and M. S. Zubairy, *Quantum Optics* (Cambridge University Press, 1997).

[9] R. Loudon, *The Quantum Theory of Light* (Oxford University Press, 1973).

[10] Y. Aharonov, D. Z. Albert, and L. Vaidman, "How the result of a measurement of a component of the spin of a spin-1/2 particle can turn out to be 100," Phys. Rev. Lett. **60**, 1351 (1988).

[11] Y. Aharonov and L. Vaidman, "The two-state vector formalism of qauntum mechanics: an updated review," arXiv:quant-ph/0105101v2 (2007).

[12] I. M. Duck, P. M. Stevenson, and E. C. G. Sudarshan, "The sense in which a "weak measurement" of a spin-1/2 particle's spin component yields a value 100," Phys. Rev. D **40**, 2112 (1989).

[13] G. J. Pryde, J. L. O'Brien, A. G. White, T. C. Ralph, and H. M. Wiseman, "Measurement of quantum weak values of photon polarization," Phys. Rev. Lett. **94**, 220405 (2005).

[14] N. W. M. Ritchie, J. G. Story, and R. G. Hulet, "Realization of a measurement of a ''weak value''," Phys. Rev. Lett. **66**, 1107 (1991).

[15] P. B. Dixon, D. J. Starling, A. N. Jordan, and J. C. Howell, "Ultrasensitive beam deflection measurement via interferometric weak value amplification," Phys. Rev. Lett. **102**, 173601 (2009).

[16] D. J. Starling, P. B. Dixon, A. N. Jordan, and J. C. Howell, "Optimizing the signal-to-noise ratio of a beam-deflection measurement with interferometric weak values," Phys. Rev. A **80**, 041803 (R) (2009).

[17] D. Starling et al., "Phase amplification using weak value formalism," arXiv:quant-ph/0000.0000 (2009).

[18] D. J. Starling, P. B. Dixon, N. S. Williams, A. N. Jordan, and J. C. Howell, "Continuous phase amplification with a sagnac interferometer," Phys. Rev. A **82**, 011802 (2010).

[19] D. J. Starling, P. B. Dixon, A. N. Jordan, and J. C. Howell, "Precision frequency measurements with interferometric weak values," Phys. Rev. A **82**, 063822 (2010).

[20] J. M. Hogan, J. Hammer, S.-W. Chiow, S. Dickerson, D. M. S. Johnson, T. Kovachy, A. Sugarbaker, and M. A. Kasevich, "Precision angle sensor using an optical lever inside a sagnac interferometer," Opt. Lett. **36**, 1698 (2011).

[21] M. D. Turner, C. A. Hagedorn, S. Schlamminger, and J. H. Gundlach, "Pico-radian deflection measurement with an interferometric quasi-autocollimator using weak value amplification," Opt. Lett. **36**, 1479 (2011).

[22] N. S. Williams and A. N. Jordan, "Weak values and the leggett-garg inequality in solid-state qubits," Phys. Rev. Lett. **100**, 026804 (2008).

[23] A. Romito, Y. Gefen, and Y. M. Blanter, "Weak values of electron spin in a double quantum dot," Phys. Rev. Lett. **100**, 056801 (2008).

[24] J. Dressel, Y. Choi, and A. N. Jordan, "Measuring which-path information with coupled electronic mach-zehnder interferometers," Phys. Rev. B **85**, 045320 (2012).

[25] L. Hardy, "Quantum mechanics, local realistic theories, and lorentz-invariant realistic theories," Phys. Rev. Lett. **68**, 2981 (1992).

[26] J. S. Lundeen and A. M. Steinberg, "Experimental joint weak measurement on a photon pair as a probe of hardy's paradox," Phys. Rev. Lett. **102**, 020404 (2009).

[27] D. Rohrlich and Y. Aharonov, "Cherenkov radiation of superluminal particles," Phys. Rev. A **66**, 042102 (2002).

[28] S. P. Yakir Aharonov and P. Skrzypczyk, "Measuring which-path information with coupled electronic mach-zehnder interferometers," arXiv:quant-ph/1202.0631v1 (2012).

[29] G. Mitchison, R. Jozsa, and S. Popescu, "Sequential weak measurement," Phys. Rev. A **76**, 062105 (2007).

[30] O. Hosten and P. Kwiat, "Observation of the Spin Hall Effect of Light via Weak Measurements," Science **319**, 787 (2008).

[31] D. R. Solli, C. F. McCormick, R. Y. Chiao, S. Popescu, and J. M. Hickmann, "Fast light, slow light, and phase singularities: A connection to generalized weak values," Phys. Rev. Lett. **92**, 043601 (2004).

[32] N. Brunner, A. Acín, D. Collins, N. Gisin, and V. Scarani, "Optical telecom networks as weak quantum measurements with postselection," Phys. Rev. Lett. **91**, 180402 (2003).

[33] N. Brunner, V. Scarani, M. Wegmüller, M. Legré, and N. Gisin, "Direct measurement of superluminal group velocity and signal velocity in an optical fiber," Phys. Rev. Lett. **93**, 203902 (2004).

[34] R. M. Camacho, P. B. Dixon, R. T. Glasser, A. N. Jordan, and J. C. Howell, "Realization of an all-optical zero to π cross-phase modulation jump," Phys. Rev. Lett. **102**, 013902 (2009).

[35] J. Dressel, S. Agarwal, and A. N. Jordan, "Contextual values of observables in quantum measurements," Phys. Rev. Lett. **104**, 240401 (2010).

[36] A. Aiello and J. P. Woerdman, "Role of beam propagation in goos–hänchen and imbert–fedorov shifts," Opt. Lett. **33**, 1437 (2008).

[37] J. C. Howell, D. J. Starling, P. B. Dixon, P. K. Vudyasetu, and A. N. Jordan, "Interferometric weak value deflections: Quantum and classical treatments," Phys. Rev. A **81**, 033813 (2010).

[38] N. W. M. Ritchie, J. G. Story, and R. G. Hulet, "Realization of a measurement of a ''weak value''," Phys. Rev. Lett. **66**, 1107 (1991).

[39] J. Dressel and A. N. Jordan, "Significance of the imaginary part of the weak value," Phys. Rev. A **85**, 012107 (2012).

[40] P. K. Vudyasetu, *Slow Light, Stopped Light and Guided Light in Hot Rubidium Vapor Using Off-resonant Interactions* (University of Rochester, 2011).

[41] P. W. Milonni, *Fast light, slow light and left-handed light* (CRC Press, 2005).

[42] V. B. Braginskii and Y. I. Vorontsov, "Quantum-mechanical limitations in macroscopic experiments and modern experimental technique," Sov. Phys. Uspekhi **17**, 644 (1975).

[43] C. A. J. Putman et al., "A detailed analysis of the optical beam deflection technique for use in atomic force microscopy," J. Appl. Phys. **72**, 6 (1992).

[44] J. Goodman, *Introduction to Fourier Optics* (Roberts & Co Publishers, 2005), 3rd ed.

[45] J. J. Bollinger et al., "Optimal frequency measurements with maximally correlated states," Phys. Rev. A **54**, R4649 (1996).

[46] S. F. Huelga et al., "Improvement of frequency standards with quantum entanglement," Phys. Rev. Lett. **79**, 3865 (1997).

[47] Y.-q. Li et al., "Sub-shot-noise laser doppler anemometry with amplitude-squeezed light," Phys. Rev. Lett. **78**, 3105 (1997).

[48] V. Giovannetti, S. Lloyd, and L. Maccone, "Quantum-enhanced positioning and clock synchronization," Nature **412**, 417 (2001).

[49] D. Kleckner and D. Bouwmeester, "Sub-kelvin optical cooling of a micromechanical resonator," Nature **444**, 75 (2006).

[50] G. Meyer and N. M. Amer, "Erratum: Novel optical approach to atomic force microscopy," Appl. Phy. Lett. **53**, 2400 (1988).

[51] D. Rugar, H. J. Mamin, and P. Guethner, "Improved fiber-optic interferometer for atomic force microscopy," Appl. Phys. Lett. **55**, 2588 (1989).

[52] S. Barnett et al., "Ultimate quantum limits for resolution of beam displacements," Eur. Phys. J. D **22**, 513 (2003).

[53] K.-X. Sun et al., "Polarization-based balanced heterodyne detection method in a sagnac interferometer for precision phase measurement," Opt. Lett. **22**, 1359 (1997).

[54] R. Erlandsson et al., "Atomic force microscopy using optical interferometry," J. Vac. Sci. Technol. A **6**, 266 (1988).

[55] E. J. Post, "Sagnac effect," Rev. Mod. Phys. **39**, 475 (1967).

[56] J. Schmitt, "Optical coherence tomography (oct): a review," Selected Topics in Quantum Electronics, IEEE Journal of **5**, 1205 (1999), ISSN 1077-260X.

[57] A. Wehr and U. Lohr, "Airborne laser scanning–an introduction and overview," ISPRS Journal of Photogrammetry and Remote Sensing **54**, 68 (1999), ISSN 0924-2716.

[58] C. M. Caves, "Quantum-mechanical noise in an interferometer," Phys. Rev. D **23**, 1693 (1981).

[59] M. J. Holland and K. Burnett, "Interferometric detection of optical phase shifts at the heisenberg limit," Phys. Rev. Lett. **71**, 1355 (1993).

[60] B. L. Higgins et al., "Demonstrating heisenberg-limited unambiguous phase estimation without adaptive measurements," New Journal of Physics **11**, 073023 (2009).

[61] Z. Y. Ou, "Fundamental quantum limit in precision phase measurement," Phys. Rev. A **55**, 2598 (1997).

[62] A. Abramovici et al., "LIGO: The Laser Interferometer Gravitational-Wave Observatory," Science **256**, 325 (1992).

[63] M.-L. Junttila and B. Stahlberg, "Laser wavelength measurement with a fourier transform wavemeter," Appl. Opt. **29**, 3510 (1990).

[64] J. Ishikawa and H. Watanabe, "A fringe-counting wavemeter for infrared laser diodes," IEEE Trans. Instrum. Meas. **42**, 423 (1993).

[65] D. Jones, S. Diddams, J. Ranka, A. Stentz, R. Windeler, J. Hall, and S. Cundiff, "Carrier-envelope phase control of femtosecond mode-locked lasers and direct optical frequency synthesis," Science **288**, 635 (2000).

[66] T. Udem, R. Holzwarth, and T. W. Hansch, "Optical frequency metrology," Nature **416**, 233 (2002).

[67] S. Falke, H. Knöckel, J. Friebe, M. Riedmann, E. Tiemann, and C. Lisdat, "Potassium ground-state scattering parameters and born-oppenheimer potentials from molecular spectroscopy," Phys. Rev. A **78**, 012503 (2008).

[68] C. Eisele, A. Y. Nevsky, and S. Schiller, "Laboratory test of the isotropy of light propagation at the $10-17$ level," Phys. Rev. Lett. **103**, 090401 (2009).

[69] T. Hori, T. Matsui, K. Araki, and H. Inomata, "Variable-finesse wideband fabry-perot wavemeter for far-infrared and millimeter waves," Opt. Lett. **14**, 302 (1989).

[70] N. Nishimiya, Y. Yamaguchi, Y. Ohrui, and M. Suzuki, "Frequency measuring system using mirror gap stabilized fabry-perot interferometer," Spectrochim. Acta, Part A **60**, 493 (2004).

[71] M. Notcutt, L.-S. Ma, J. Ye, and J. L. Hall, "Simple and compact 1-hz laser system via an improved mounting configuration of a reference cavity," Opt. Lett. **30**, 1815 (2005).

[72] C. Tropea, "Laser doppler anemometry: recent developments and future challenges," Meas. Sci. Technol. **6**, 605 (1995).

[73] R. Pohl et al., "The size of the proton," Nature **466**, 213 (2010).

[74] N. Brunner and C. Simon, "Measuring small longitudinal phase shifts: Weak measurements or standard interferometry?," Phys. Rev. Lett. **105**, 010405 (2010).

[75] F. L. Pedrotti and L. S. Pedrotti, *Introduction to Optics* (Prentice-Hall, Inc., 1993), 2nd ed.

[76] I. H. Malitson, "Interspecimen comparison of the refractive index of fused silica," J. Opt. Soc. Am. **55**, 1205 (1965).

[77] D. A. Steck, "Alkali d line data," (2010), URL http://steck.us/alkalidata/.

[78] Amnon and Yariv, "Four wave nonlinear optical mixing as real time holography," Optics Communications **25**, 23 (1978), ISSN 0030-4018.

[79] M. D. Lukin and A. Imamoğlu, "Nonlinear optics and quantum entanglement of ultraslow single photons," Phys. Rev. Lett. **84**, 1419 (2000).

[80] Z. Shi, R. W. Boyd, R. M. Camacho, P. K. Vudyasetu, and J. C. Howell, "Slow-light fourier transform interferometer," Phys. Rev. Lett. **99**, 240801 (2007).

[81] P. Hariharan, *Optical interferometry* (Elsevier Science, Amsterdam, 2003).

[82] S. Saraf, R. L. Byer, and P. J. King, "High-extinction-ratio resonant cavity polarizer for quantum-optics measurements," Appl. Opt. **46**, 3850 (2007).

[83] M. J. Thorpe, D. Balslev-Clausen, M. S. Kirchner, and J. Ye, "Cavity-enhanced optical frequency combspectroscopy: application to human breathanalysis," Opt. Express **16**, 2387 (2008).

[84] R. H. T. Udem and T. W. Hänsch, "Optical frequency metrology," Nature **416**, 233 (2002).

[85] A. Foltynowicz, P. Maslowski, T. Ban, F. Adler, K. C. Cossel, T. C. Briles, and J. Ye, "Optical frequency comb spectroscopy," Faraday Discuss. **150**, (2011).

[86] R. P. Abel, U. Krohn, P. Siddons, I. G. Hughes, and C. S. Adams, "Faraday dichroic beam splitter for raman light using an isotopically pure alkali-metal-vapor cell," Opt. Lett. **34**, 3071 (2009).

[87] J. A. Zielińska, F. A. Beduini, N. Godbout, and M. W. Mitchell, "Ultranarrow faraday rotation filter at the rb d1 line," Opt. Lett. **37**, 524 (2012).

[88] F. Wolfgramm, Y. A. de Icaza Astiz, F. A. Beduini, A. Cerè, and M. W. Mitchell, "Atom-resonant heralded single photons by interaction-free measurement," Phys. Rev. Lett. **106**, 053602 (2011).

[89] M. Fleischhauer, A. Imamoglu, and J. P. Marangos, "Electromagnetically induced transparency: Optics in coherent media," Rev. Mod. Phys. **77**, 633 (2005).

[90] R. Okamoto, J. L. O'Brien, H. F. Hofmann, T. Nagata, K. Sasaki, and S. Takeuchi, "An entanglement filter," Science **323**, 483 (2009).

[91] M. C. Stowe, M. J. Thorpe, A. Pe'er, J. Ye, J. E. Stalnaker, V. Gerginov, and S. A. Diddams (Academic Press, 2008), vol. 55 of *Advances In Atomic, Molecular, and Optical Physics*, pp. 1 – 60.

[92] S. A. Diddams, L. Hollberg, and V. Mbele, "Molecular fingerprinting with the resolved modes of a femtosecond laser frequency comb," Nature **445**, 627 (2007).

[93] A. Bartels, D. Heinecke, and S. A. Diddams, "10-ghz self-referenced optical frequency comb," Science **326**, 681 (2009).

[94] P. K. Vudyasetu, R. M. Camacho, and J. C. Howell, "Storage and retrieval of multimode transverse images in hot atomic rubidium vapor," Phys. Rev. Lett. **100**, 123903 (2008).

[95] R. W. Wood, *Physical Optics* (Optical Society of America, 1988).

[96] W. C. Marlow, "Hakenmethode," Appl. Opt. **6**, 1715 (1967).

[97] V. A. Sautenkov, H. Li, Y. V. Rostovtsev, and M. O. Scully, "Ultradispersive adaptive prism based on a coherently prepared atomic medium," Phys. Rev. A **81**, 063824 (2010).

[98] A. Zheltikov, A. Naumov, P. Barker, and R. Miles, "Controlling dispersion and transmission spectra of hybrid resonant-gas-filled photonic-crystal optical components," Optics and Spectroscopy **89**, 282 (2000).

[99] N. D. Finkelstein, A. P. Yalin, W. R. Lempert, and R. B. Miles, "Dispersion filter for spectral and spatial resolution of pure rotational raman scattering," Opt. Lett. **23**, 1615 (1998).

[100] N. D. Finkelstein, W. R. Lempert, and R. B. Miles, "Narrow-linewidth passband filter for ultraviolet rotational raman imaging," Opt. Lett. **22**, 537 (1997).

[101] A. P. Yalin, P. F. Barker, and R. B. Miles, "Characterization of laser seeding by use of group-velocity dispersion in an atomic-vapor filter," Opt. Lett. **25**, 502 (2000).

[102] D. Hoffman, K.-U. Münch, and A. Leipertz, "Two-dimensional temperature determination in sooting flames by filtered rayleigh scattering," Opt. Lett. **21**, 525 (1996).

[103] J. Menders, K. Benson, S. H. Bloom, C. S. Liu, and E. Korevaar, "Ultra-narrow line filtering using a cs faraday filter at 852 nm," Opt. Lett. **16**, 846 (1991).

[104] S.-Y. Lin, V. M. Hietala, L. Wang, and E. D. Jones, "Highly dispersive photonic band-gap prism," Opt. Lett. **21**, 1771 (1996).

[105] J. B. Khurgin, "Slow light in various media: a tutorial," Adv. Opt. Photon. **2**, 287 (2010).

[106] R. M. Camacho, M. V. Pack, and J. C. Howell, "Low-distortion slow light using two absorption resonances," Phys. Rev. A **73**, 063812 (2006).

[107] R. M. Camacho, M. V. Pack, J. C. Howell, A. Schweinsberg, and R. W. Boyd, "Wide-bandwidth, tunable, multiple-pulse-width optical delays using slow light in cesium vapor," Phys. Rev. Lett. **98**, 153601 (2007).

[108] P. K. V. Ryan M. Camacho and J. C. Howell, "Four-wave-mixing stopped light in hot atomic rubidium vapour," Nature Photonics **3**, 103 (2009).

[109] A. N. J. D. J. Starling, P. B. Dixon and J. C. Howell, "Precision frequency measurements with interferometric weak values," Phys. Rev. A **82**, 063822 (2010).

[110] C. J. Broadbent, R. M. Camacho, R. Xin, and J. C. Howell, "Preservation of energy-time entanglement in a slow light medium," Phys. Rev. Lett. **100**, 133602 (2008).

[111] B. Misra and E. C. G. Sudarshan, "The Zeno's paradox in quantum theory," Journal of Mathematical Physics **18**, 756 (1977).

[112] W. M. Itano, D. J. Heinzen, J. J. Bollinger, and D. J. Wineland, "Quantum Zeno effect," Phys. Rev. A **41**, 2295 (1990).

[113] S. Maniscalco, F. Francica, R. L. Zaffino, N. Lo Gullo, and F. Plastina, "Protecting entanglement via the quantum zeno effect," Phys. Rev. Lett. **100**, 090503 (2008).

[114] O. Zilberberg, A. Romito, and Y. Gefen Phys. Rev. Lett. **106**, 080405 (2011).

[115] J. S. Lundeen, B. Sutherland, A. Patel, C. Stewart, and C. Bamber Nature **474**, 188 (2011).

[116] A. Peres, "How to differentiate between non-orthogonal states," Physics Letters A **128**, 19 (1988).

[117] B. Huttner, A. Muller, J. D. Gautier, H. Zbinden, and N. Gisin, "Unambiguous quantum measurement of nonorthogonal states," Phys. Rev. A **54**, 3783 (1996).

[118] A. Chefles and S. M. Barnett, "Optimum unambiguous discrimination between linearly independent symmetric states," Physics Letters A **250**, 223 (1998).

[119] F. W. Sun, B. H. Liu, Y. X. Gong, Y. F. Huang, Z. Y. Ou, and G. C. Guo, "Experimental demonstration of phase measurement precision beating standard quantum limit by projection measurement," EPL (Europhysics Letters) **82**, 24001 (2008).

[120] P. M. Anisimov, G. M. Raterman, A. Chiruvelli, W. N. Plick, S. D. Huver, H. Lee, and J. P. Dowling, "Quantum metrology with two-mode squeezed vacuum: Parity detection beats the heisenberg limit," Phys. Rev. Lett. **104**, 103602 (2010).

[121] C. J. Broadbent, R. M. Camacho, R. Xin, and J. C. Howell, "Preservation of energy-time entanglement in a slow light medium," Phys. Rev. Lett. **100**, 133602 (2008).

[122] V. Boyer, A. M. Marino, R. C. Pooser, and P. D. Lett, "Entangled images from four-wave mixing," Science **321**, 544 (2008).

[123] C. M. Caves and B. L. Schumaker, "New formalism for two-photon quantum optics. i. quadrature phases and squeezed states," Phys. Rev. A **31**, 3068 (1985).

[124] J. E. Sharping, M. Fiorentino, and P. Kumar, "Observation of twin-beam-type quantum correlation in optical fiber," Opt. Lett. **26**, 367 (2001).

[125] P. G. Kwiat, S. Barraza-Lopez, A. Stefanov, and N. Gisin, "Experimental entanglement distillation and 'hidden' non-locality," Nature **409**, 1014 (2008).

[126] M. Ueda and M. Kitagawa, "Reversibility in quantum measurement processes," Phys. Rev. Lett. **68**, 3424 (1992).

[127] N. Katz, M. Neeley, M. Ansmann, R. C. Bialczak, M. Hofheinz, E. Lucero, A. O'Connell, H. Wang, A. N. Cleland, J. M. Martinis, et al., "Reversal of the weak measurement of a quantum state in a superconducting phase qubit," Phys. Rev. Lett. **101**, 200401 (2008).

[128] A. N. Korotkov and A. N. Jordan, "Undoing a weak quantum measurement of a solid-state qubit," Phys. Rev. Lett. **97**, 166805 (2006).

[129] A. Imamoḡlu, "Logical reversibility in quantum-nondemolition measurements," Phys. Rev. A **47**, R4577 (1993).

[130] A. Royer, "Reversible quantum measurements on a spin 1/2 and measuring the state of a single system," Phys. Rev. Lett. **73**, 913 (1994).

[131] M. Koashi and M. Ueda, "Reversing measurement and probabilistic quantum error correction," Phys. Rev. Lett. **82**, 2598 (1999).

[132] Y.-S. Kim, Y.-W. Cho, Y.-S. Ra, and Y.-H. Kim, "Reversing the weak quantum measurement for a photonic qubit," Optics Express **17**, 11978 (2009).

[133] Q. Sun, M. Al-Amri, L. Davidovich, and M. S. Zubairy, "Reversing entanglement change by a weak measurement," Phys. Rev. A **82**, 052323 (2010).

[134] W. K. Wootters, "Entanglement of formation of an arbitrary state of two qubits," Phys. Rev. Lett. **80**, 2245 (1998).